Spectroscopic studies of coronal structures using ground and space based data

A Thesis

Submitted for the Award of the Degree of

Doctor of Philosophy in Physics

To

Mangalore University

by

S. Krishna Prasad

Under the Supervision of

Prof. Jagdev Singh (Guide)

Prof. Dipankar Banerjee (Co-Guide)

Indian Institute of Astrophysics

Bangalore - 560 034

India

September 2013

Declaration of Authorship

I hereby declare that the matter contained in this thesis is the result of the investigations carried out by me at Indian Institute of Astrophysics, Bangalore, under the supervision of Profs. Jagdev Singh and Dipankar Banerjee. This work has not been submitted for the award of any other degree, diploma, associateship, fellowship, etc. of any other university or institute.

Signed:

Date:

Certificate

This is to certify that the thesis entitled **'Spectroscopic studies of coronal structures using ground and space based data'** submitted to the Mangalore University by Mr. S. Krishna Prasad for the award of the degree of Doctor of Philosophy in the faculty of Science, is based on the results of the investigations carried out by him under my supervision and guidance, at Indian Institute of Astrophysics. This thesis has not been submitted for the award of any other degree, diploma, associateship, fellowship, etc. of any other university or institute.

Signed: _____

Date: _____

Signed: _____

Date: _____

Dedicated to

my

family and friends...

Acknowledgements

I feel immense pleasure in expressing my sincere gratitude to my supervisors, Prof. Jagdev Singh and Prof. Dipankar Banerjee, for their invaluable guidance throughout the tenure. I am indebted to Prof. Jagdev Singh, for all the wonderful discussions we had and for his patience in explaining me simpler things. My special thanks are due to Prof. Dipankar Banerjee, for his constant encouragement and support, without which much of the work in this thesis would not have reached the stage of completion. It was all my pleasure to work with them.

I am thankful to the Director, Dean and BGS of our institute for providing me with all the necessary facilities for my research work. I thank Dr. Christina Birdie, Mr. B. S. Mohan, Mr. Prabhahar and the other staff of library for assisting me in accessing books and journals. I thank Dr. Baba Varghese, Mr. Fayaz and Mr. Ashok for their help in computer related issues.

I thank our administrative officer Dr. P. Kumaresan, personnel officer Mr. Narasimha Raju, Accounts officer, Mr. S. B. Ramesh and all other administrative staff for their timely help in completing the admin related work.

I would like to thank Nagaraj, Nataraj, Blesson, Bharat, Ramya, Tapan, Veeru bhai, Vigeesh, Uday, Anant, Girju, Amit, Chandu and all my seniors, for making my initial life at IIA, more fun and enjoyable. I specially thank Nagaraj for all the wonderful trips we had; girju for teaching me the academic basics; amit, girju and veeru bhai for teaching me Hindi; Nataraj for his guidance; amit, anant, girju, and chandu for standing with me at times when needed.

It is my pleasure to thank Arya, Rathna, Prashanth, Dinesh, Avijeet, Sudha, Sajal, Sam, Arun, Sasi, Suresh, Pradeep, Manpreet, Shruti, Paru, Sindhuja, Indu, Ramya P., Hema, Anantha, Jayashree, Drisya, Susmitha, Honey, Tanmoy, and all those who made my stay at IIA memorable.

I must acknowledge my childhood friends, Anil, Siva, Uma, Balaji and my M.Sc friends, Hari, Sivaram, Prabhakar, Srinu, and Naresh, for their enormous help and support. My special thanks are due to Hari for being with me throughout the ups and downs in this path.

My sincere thanks are due to Prof. Balakrishna and Prof. Dharmaprakash of department of physics at Mangalore University, for their help in registration, arranging the colloquium and assisting me in other University related formalities. I also thank Mrs. Anita for providing the required information on official procedures with her prompt responses.

Last but not the least, I would like to thank my parents, brother, and all those who extended their support for the successful completion of this project.

List of Publications

1. Thermal Structure of Coronal Loops as Seen with Norikura Coronagraph
   Krishna Prasad, S.; Singh, Jagdev; Ichimoto, K., 2013, *ApJL*, **765**, 46 – 50.

2. Dynamics of Coronal Bright Points as seen by SWAP, AIA and HMI
   Chandrashekhar, K.; **Krishna Prasad, S.**; Banerjee, D.; Ravindra, B.; Seaton, Daniel B., 2013, *Solar Physics*, **286**, 125 – 142

3. Variation of Emission Line Width in Mid- and High-Latitude Corona
   Krishna Prasad, S.; Singh, Jagdev; Banerjee, D., 2013, *Solar Physics*, **282**, 427 – 442.

4. Omnipresent long-period intensity oscillations in open coronal structures
   Krishna Prasad, S.; Banerjee, D.; Van Doorsselaere, T.; Singh, J., 2012, *A & A*, **546**, 50 – 54

5. Oscillations in active region fan loops: Observations from EIS/Hinode & AIA/SDO
   Krishna Prasad, S.; Banerjee, D.; Singh, Jagdev., 2012, *Solar Physics*, **281**, 67 – 85

6. Propagating intensity disturbances in polar corona as seen from AIA/SDO
   Krishna Prasad, S.; Banerjee, D.; Gupta, G. R., 2011, *A & A*, **528**, L4 – L8

Presentations

1. Oral presentation in 39^{th} *COSPAR Scientific Assembly*, held at Mysore, India during 14-22 July 2012.

2. Oral presentation in *BUKS 2012 workshop*, held at Crete, Greece, during 4-7 July, 2012.

3. Oral presentation in *workshop on physics of the transition region and corona*, held at IUCAA, Bangalore, during 5-7 September 2011.

4. Oral presentation in *Fifth Coronal loops workshop*, held at Palma de Mallorca, Spain, during 29 June - 2 July 2011.

5. Oral presentation in *In house meeting*, held at Bangalore, India on 18^{th} April, 2011.

6. Poster presentation in 3^{rd} *Indo-China workshop and* 1^{st} *Asia-Pacific solar physics meeting*, held at Bangalore, India, during 21-24 March, 2011.

7. Oral presentation in the *Astronomical Society of India meeting 2011*, held at Raipur, India, during 23-25 February 2011.

8. Poster presentation in *Space climate 4*, held at Goa, India, during 16-21 January 2011.

9. Oral presentation in 13^{th} *Young Astronomers Meet*, held at Physical Research Laboratory, Ahmedabad, during 3-5 September 2010.

10. Oral presentation in 38^{th} *COSPAR Scientific Assembly*, held at Bremen, Germany during 18-25 July 2010.

11. Oral presentation in *Asia Oceania Geosciences Society meeting 2010*, held at Hyderabad, during 5-9 July 2010.

Abstract

Solar corona, the tenuous outer atmosphere of the Sun, is very hot with temperatures of the order of a few million kelvin. The main energy source for heating the corona and the physical mechanism behind the acceleration of fast solar wind are not clearly understood yet. These are major long-standing problems in solar physics and serve as a common motivation for most of the coronal studies. Our knowledge on these issues is advancing with the recent advent of instruments with high spatial, temporal, and spectral resolutions, which at the same time brought many new problems into light. A few such problems motivated the studies presented in this thesis. Broadly, two different issues are addressed, one connected with the variation of spectral line parameters and the other related to the ambiguity on the nature of propagating intensity disturbances. Data from a ground-based coronagraph, a space-based Extreme Ultraviolet (EUV) imager and a space-based EUV spectrometer were used for this purpose.

The thermal structure of a coronal loop is crucial for determining the plasma heating mechanism. Temperature variation along 18 different loop structures was studied using high resolution spectroscopic data from Norikura coronagraph. Observations were made simultaneously in multiple iron emission lines. Using the temperature sensitive emission line ratios [Fe XIV] 5303 Å/[Fe XIII] 10747 Å, and [Fe XI] 7892 Å/[Fe X] 6374 Å the temperature and its gradients were computed for all the structures. It was found that the temperature gradients are negative for most of the structures observed in hotter lines and positive for those observed in colder lines. This indicates that the loop tops in general appear cooler or hotter depending on the line pair chosen. To explain this complex behaviour, a gradual interaction between different temperature plasma was proposed. Interestingly, extensive analysis in the past, on line width variation with altitude, also indicated a similar behaviour, in agreement with this mixing scenario. This behaviour is now verified for polar regions. It was found that the FWHM of red emission line ([Fe X] 6374 Å) increase with height whereas that of green emission line ([Fe XIV] 5303 Å) decrease with height consistent with the results from equatorial regions. An interesting behaviour of green line was observed when latitudinal comparison was made. Line widths are higher in polar regions for all the

emission lines studied except for the green line. The higher line widths in polar regions are often associated with the existence of a non-thermal source powering the fast solar wind. But, the observed behaviour of green line seem to disagree with this.

Some of the recent observations question the uniqueness of the interpretation of propagating disturbances (PDs) as slow magneto-acoustic waves. It is argued that the high-speed quasi-periodic upflows produce similar signatures and it is difficult to distinguish them. In an attempt to resolve this ambiguity, these PDs were studied in different open structures. In polar regions, space-time maps were constructed for several plume and interplume structures using artificial slits that are wider than usual. This is to suppress the effect of fainter jets, if any present, causing the upflows. Stronger jets were identified from movies. Despite these measures, PDs were seen in all the structures studied. Moreover, they were found to be insensitive to changes in slit width. This implies the coherent nature of these disturbances. The average propagation speeds were found to be dependent on the temperature. These properties favour the interpretation of PDs as due to slow waves rather than high speed upflows. Same technique cannot be applied for AR fan loops since they are relatively thin. To compensate for this, simultaneous spectroscopic and imaging data were used to study PDs in active region fan loops. Two different periodicities short ($<$3 min) and long ($\approx$9 min) were observed with different nature. The shorter periodicities showed oscillations in intensity, Doppler shift and line width whereas the longer ones did not show any line width oscillations. The line profiles are symmetric with no visible blue-shifted component. The apparent propagation speeds were computed for the longer periods from the co-temporal imaging data which show the temperature dependence. The observed properties suggest the longer periods are due to slow MHD waves and the shorter ones could be due to the simultaneous presence of more than one MHD modes.

To further supplement the previous study, spatial damping was studied in different open structures both on-disk and off-limb. Powermaps constructed at three different period ranges indicate that the PDs with long periods travel farther distances before getting damped. Similar behaviour is observed in all the structures. Spatial damping was also studied in different temperature channels. Results indicate lower amplitudes and faster damping in hotter channels. All these observed properties were explained using a simple slow wave model considering thermal conduction as the damping mechanism.

Contents

List of Figures

List of Tables

Abbreviations

NASA	**N**ational **A**eronautics and **S**pace **A**dministration
NAOJ	**N**ational **A**stronomical **O**bservatory of **J**apan
NOAA	**N**ational **O**ceanic and **A**tmospheric **A**dministration
SOHO	**S**olar and **H**eliospheric **O**bservatory
SUMER	**S**olar **U**ltraviolet **M**easurements of **E**mitted **R**adiation
UVCS	**U**ltra**V**iolet **C**oronagraph **S**pectrometer
EIT	**E**xtreme ultraviolet **I**maging **T**elescope
TRACE	**T**ransition **R**egion and **C**oronal **E**xplorer
CCD	**C**harge **C**oupled **D**evice
UT	**U**niversal **T**ime
JST	**J**apanese **S**tandard **T**ime
MHD	**M**agneto**H**ydro**D**ynamic
CCSDS	**C**onsultative **C**ommittee for **S**pace **D**ata **S**ystems

Chapter 1

Introduction

The Sun is a second-generation star, formed from the material left by the first-generation stars in our Galaxy, that underwent supernova explosions. It is the major source of heat and light that sustain life on Earth. It also emanates highly energetic charged particles continuously into the interplanetary space. These particles are often channelled down through polar field lines, interact with Earth's atmosphere and produce beautiful auroral patterns. However, occasional energetic explosions on Sun, can make the solar wind intense enough to produce geomagnetically induced currents that can damage power grids and cause electricity blackout. It can also destroy the satellites and pose a threat to astronauts. All these potential impacts indicate the importance of studying the Sun and its atmosphere. Besides, the extreme conditions in the outer atmosphere of the Sun that are difficult to reproduce on Earth, makes it a unique physical laboratory to improve our understanding in various branches of physics.

Energy is generated in the core of the Sun by nuclear reactions. Four protons fuse together to form Helium nuclei and release energy. This energy is mainly transported by radiation up to 0.67 $R_\odot$ and by convection from there to solar surface. Based on the energy transportation processes these regions are termed as radiative and convective zones respectively. Different layers of the Sun are shown in Figure 1.1.

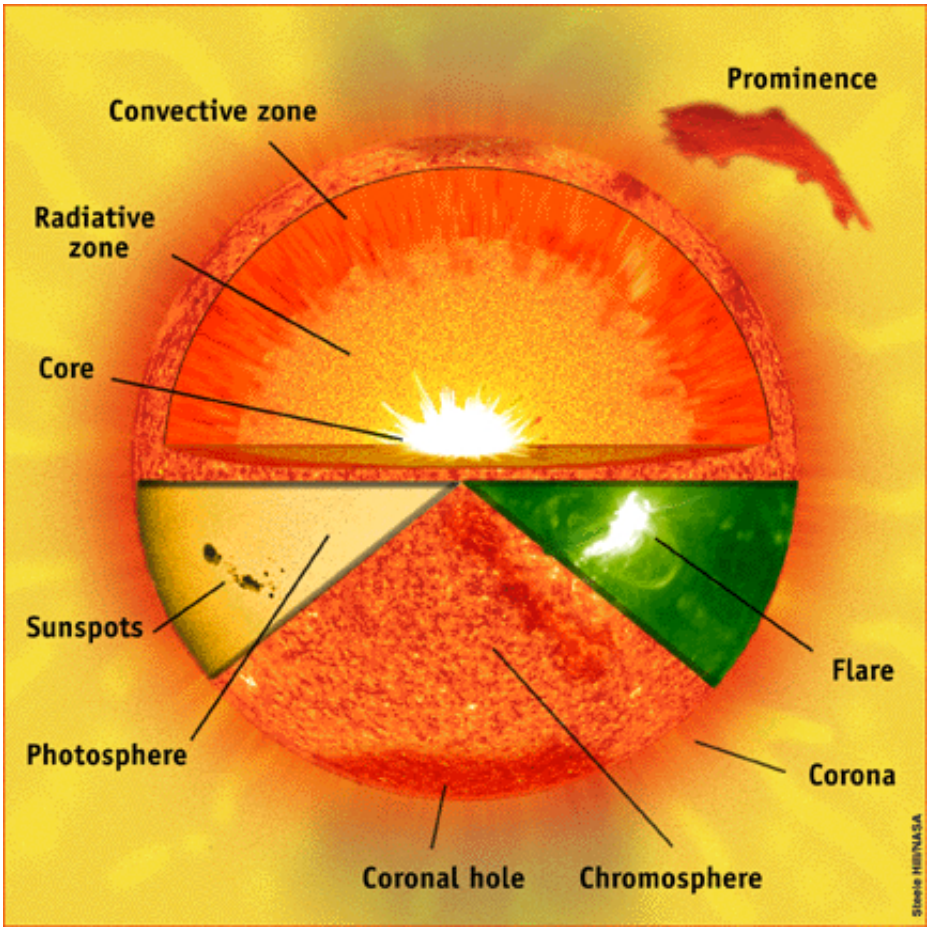

FIGURE 1.1: A cartoon image showing the different layers of Sun from the central core to outer corona. *Image credit:* http://sohowww.nascom.nasa.gov

1.1 The Solar Atmosphere

The region outside the visible surface of the Sun is known as solar atmosphere. It comprises of three layers namely, photosphere, chromosphere, and corona. Different layers of the solar atmosphere are shown in Figure 1.1. The temperature variation across these layers is shown in Figure 1.2 for a model solar atmosphere. Starting from the surface of the Sun, the temperature first decreases over a few hundred kilometres and reaches a minimum value. This region is known as photosphere. It gradually rises from there up to about 2,000 km height from the photosphere and then sharply increases to the order of a million kelvin within the short distance of a few hundred kilometres. The layer between the temperature

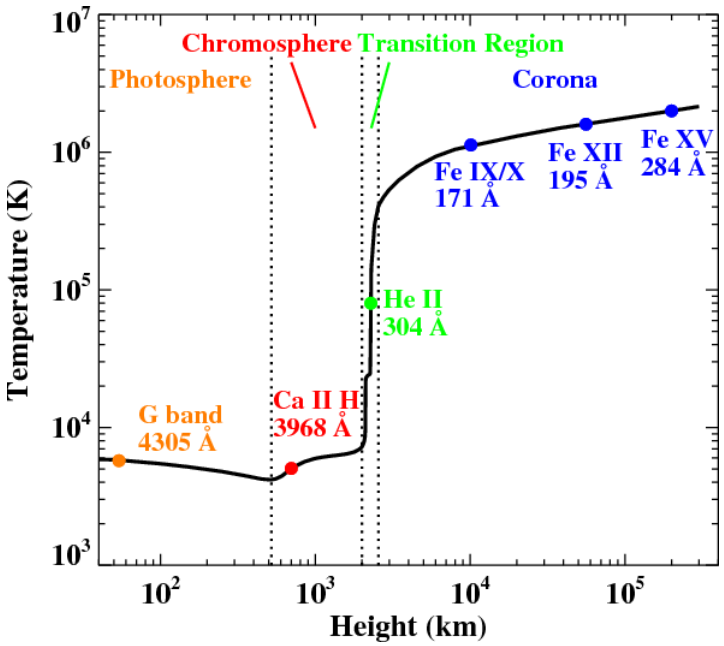

FIGURE 1.2: Temperature variation from photosphere to corona. Spectral lines that can be used to observe different regions of the atmosphere are marked at respective locations. Reproduced from Yang *et al.* (2009)

minimum up to where the temperature becomes approximately 20,000 K is generally defined as chromosphere. The region where the temperature reaches $\sim 10^6$ K and the densities are very low compared to the chromosphere is called solar corona. The thin layer separating the dense, cool chromosphere and tenuous, hot corona with temperatures of the order of 10^5 K, is called transition region. The rise in temperature from chromosphere reaching such a high values in corona is not generally expected and is known as coronal heating problem. Because of this huge temperature variation, lines from molecular G-band to those from heavily ionized iron can be observed in the solar atmosphere. Different lines formed at different heights of the atmosphere are marked in Figure 1.2. Note the temperature variation presented here is just a representative variation and the actual heights of these layers may vary from one region of the solar atmosphere to the other.

Another important parameter that determines the dynamics of solar atmosphere is plasma-β, the ratio of gas pressure to magnetic pressure, given as

$$\beta = \frac{p_{gas}}{p_{mag}} \approx \frac{nkT}{(B^2/8\pi)} \tag{1.1}$$

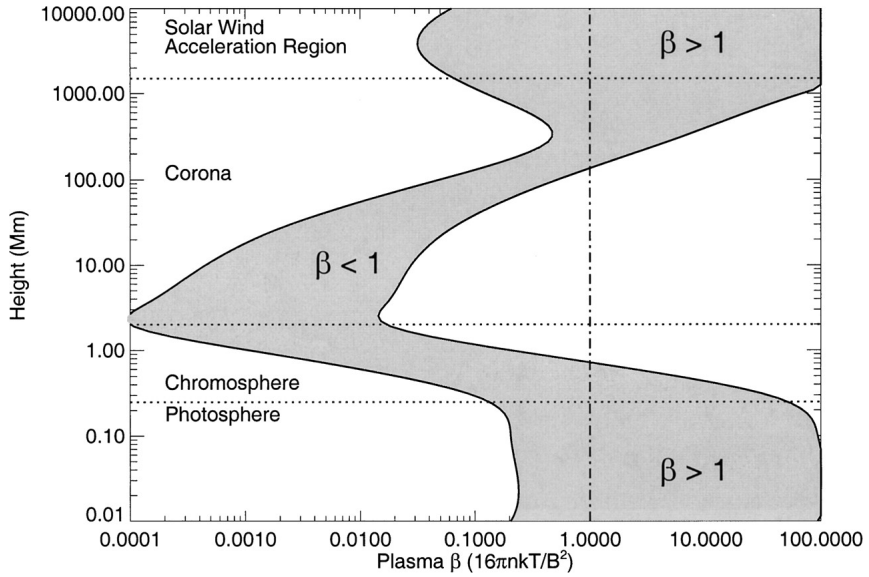

FIGURE 1.3: Variation of plasma-β in the solar atmosphere for a range of magnetic field strengths between 100 G and 2500 G. Extracted from Aschwanden (2005)

The variation of this parameter in the solar atmosphere is illustrated in Figure 1.3. At the photospheric level, the plasma-β is greater than 1 implying the domination of plasma motions over the magnetic fields whereas in the chromosphere and corona this value decreases below 1, leading to a confinement of plasma to the magnetic structures (this makes the corona highly structured). In the extended upper atmosphere this value rises again causing the magnetic field to advect out with the solar wind plasma.

1.1.1 Photosphere

The photosphere is defined as the surface of the Sun from where photons start escaping into space. No photon escapes from below this layer and hence cannot be seen directly. The layer is a few hundred kilometres thick and the actual surface is usually defined using optical depth. Since this quantity is dependent on wavelength, the exact definition of photosphere is given as the region where optical depth τ, becomes unity for the radiation of wavelength 5000 Å. The temperature of this layer is about 6400 K. A variety of features such as granules, supergranules, and sunspots are observed in this layer. Granules are small cell-like structures,

bright at the centre, formed due to surface convection. These structures have typical sizes of $\approx\ 100 - 1100$ km and lifetimes of the order of several minutes. A much larger version of these features are the supergranules. They are about 30,000 km across, and a few thousand kilometres thick with lifetimes of the order of one to several days. Material from the interior is convected upwards at the cell centre, spreads out towards the cell boundaries nearly horizontally with velocities of 0.4 km s^{-1} and then convected downwards with velocities of 0.1 km s^{-1}. While doing so, the convective flow transports concentrations of magnetic fields towards the boundaries forming a magnetic network region around it. The region within the cells are called internetwork. As one can see, most of the pattern observed here is convection dominated since the plasma-β is high in this region. Sunspots are an exception to this, where the magnetic field concentration is high enough to inhibit the convective flow and hence appear dark. The darkest part of the sunspot is called umbra where the temperature drops well below the ambient temperature. The less dark outer region of a sunspot is termed as penumbra. The number of sunspots visible in the photosphere varies periodically with a period of 11 years. This is called solar cycle. Often some bright patches are visible close to sunspots. These are called faculae. These are again concentrated magnetic field regions but over a smaller area which makes them look bright. Although, the sunspots are dark, the total brightness of the Sun increases by about 0.1% during solar maximum because of the faculae.

1.1.2 Chromosphere

Chromosphere starts from the temperature minimum region and extends up to the transition region. The thickness of the layer is about 2,000 km to 3,000 km and the temperature increases from about 4,400 K to 20,000 K. At these temperatures hydrogen is partially ionized with most of it in excited state leading to Hα emission at 6563 Å. This emission gives this layer a reddish pink colour because of which it is named chromo(colour)sphere. Many interesting phenomena like spicules and prominences can be observed in this layer. Spicules are jet like eruptions of gas that shoot upwards, ejecting material off the surface and outwards into the Corona at speeds of about $20-30$ km s^{-1}. Their lifetimes are of the order of minutes.

They are usually found on boundaries between supergranules and form as a result of shocks due to p-mode leakage at inclined magnetic fields (De Pontieu *et al.* 2004). When viewed in Hα line they appear dark on the disk covering about 10% of the solar surface. They appear dark against the photosphere as they are cooler. Solar prominences are dense clouds of gas suspended above the Sun's surface by its magnetic field. There are two types of prominences: Quiescent and Active. Quiescent Prominences are the more stable and long-lived prominences. They can retain their structure for periods up to a year before they evolve by breaking up, suddenly disappearing or occasionally violently erupting into space with a tremendous burst of energy, then dispersing. Active Prominences are the opposite of quiescent prominences. They tend to be much short-lived and smaller. Prominences, when viewed against the disk, appear dark and are called filaments.

The transition region is a very thin layer separating the chromosphere from corona. Temperature changes rapidly from 20,000 K to 1 MK over a short distance. The plasma-β becomes very low and the magnetic fields gain a complete dominance (see Figure 1.3). Hydrogen is ionized at these temperatures and therefore the dominant emission is from ions of carbon, oxygen and silicon (Mariska 1992).

1.1.3 Corona

The solar corona is the tenuous outer atmosphere of the Sun where temperatures are of the order of a million kelvin. At these high temperatures hydrogen and helium are stripped of their electrons and can not be detected. Hence, the spectral lines are observed from highly ionized calcium and iron. When observed in visible light during a solar eclipse or with a coronagraph, the emission is due to three main components to the coronal light. They are labelled, K-corona, F-corona, and E-corona. K-corona displays a continuous spectrum arising out of the photospheric light that is scattered by the electrons of the coronal plasma. F-corona arises due to the scattering of the photospheric light by dust particle in the ecliptic plane. It is characterized by the absorption lines similar to that observed in the on-disk spectrum. These lines are not visible in the K-corona because of the higher thermal velocities of the scattering electrons that wash away the absorption lines due to

Doppler shifts. E-corona represents the emission directly coming from the coronal gas and consists of isolated spectral lines formed by the coronal ions. In some cases T-corona may also be visible. This comes from the thermal emission of the interplanetary dust and is largely in infrared part of the spectrum.

The plasma-β is very low in this region due to which plasma is mostly confined to thread like magnetic structures called coronal loops. These loops either extend into the interplanetary space or curve back to photosphere which are often referred to open and closed loops respectively. This confinement of plasma makes the corona highly structured. Corona can be divided into three regions: Active regions, coronal holes and quiet Sun regions. Active regions are dominated by closed field structures, and the coronal holes are dominated by open field structures. Quiet Sun regions comprise a mixture of both. Since the corona is magnetically dominated, the overall shape of outer corona varies greatly over the solar activity cycle. It appears more uniform during solar maximum when the streamers are distributed at all latitudes and more inhomogeneous during solar minimum when the streamers are restricted to equatorial latitudes.

1.1.3.1 Coronal Heating

Eclipse observations of the solar corona in the later half of the nineteenth century, revealed several unidentified lines which were thought to be coming from an unknown element called *coronium* until the work by Bengt Edlén and Walter Grotrian in 1942, who identified that these lines are emitted by elements such as iron and calcium at very high ionization states (Edlén 1943). They inferred a coronal temperature of $T \approx 1$ MK from the formation temperature of these ions. This also explained the larger extent of corona above the solar surface (higher temperatures mean larger scale heights). But, why the corona is so hot and how is it maintained at such high temperatures, especially when the photospheric temperature is of the order of 6000 K, remained a puzzle. Although considerable progress has been made, this problem is not yet solved and is widely known as coronal heating problem in astrophysics. The temperature is expected to steadily drop down from the photosphere according to second law of thermodynamics. The energy

TABLE 1.1: Coronal energy losses due to different processes, in units of erg cm^{-2} s^{-1}. Reproduced from Withbroe and Noyes (1977).

Parameter	Coronal hole	Quiet Sun	Active region
Coronal temperature [K], at $r \approx 1.1$ $R_\odot$	10^6	1.5×10^6	2.5×10^6
Coronal energy losses [erg cm^{-2} s^{-1}]			
– Conductive flux F_C	6×10^4	2×10^5	$10^5 - 10^7$
– Radiative flux F_R	10^4	10^5	5×10^6
– Solar wind flux F_W	7×10^5	$\lesssim 5 \times 10^4$	$(< 10^5)$
– Total corona loss $F_C + F_R + F_W$	8×10^5	3×10^5	10^7
Solar wind mass loss [g cm^{-2} s^{-1}]	2×10^{-10}	$\lesssim 2 \times 10^{-11}$	$(< 4 \times 10^{-11})$

losses due to thermal conduction and the EUV radiation would cool off the corona within a matter of hours to days, if there is no other energy source. The estimated energy losses in different parts of the solar corona are listed in Table 1.1 as given by Withbroe and Noyes (1977).

Several different mechanisms had been proposed over the years to power the corona, but the models that still prevailed are based on heating due to waves and heating due to reconnection. These are often categorized as AC (Alternate Current) mechanisms and DC (Direct Current) mechanisms depending on the time scale at which the photospheric driver changes compared to the Alfvén transit time along a structure. If the photospheric driver displaces the foot point of a loop at a time scale much longer than the Alfvén transit time then it allows magnetic stresses to build up over time which when dissipated due to reconnection produces heating. This is the case for DC models. On the other hand, if the driver displaces the coronal loop foot points at a rapid rate, waves are generated which propagate up into the corona and get dissipated to heat the plasma locally. This process defines AC models. For more information, see reviews on coronal heating by Klimchuk (2006) and Erdélyi and Ballai (2007). Although, it is more or less agreed at present that the energy source is derived from the convective motions of the photosphere and magnetic fields play a fundamental role in heating, the main problem now is to find the exact mechanism through which the energy is transferred and dissipated in corona. It is also possible that different processes are in play at different regions (Jess *et al.* 2009; Wedemeyer-Böhm *et al.* 2012; Morton *et al.* 2012).

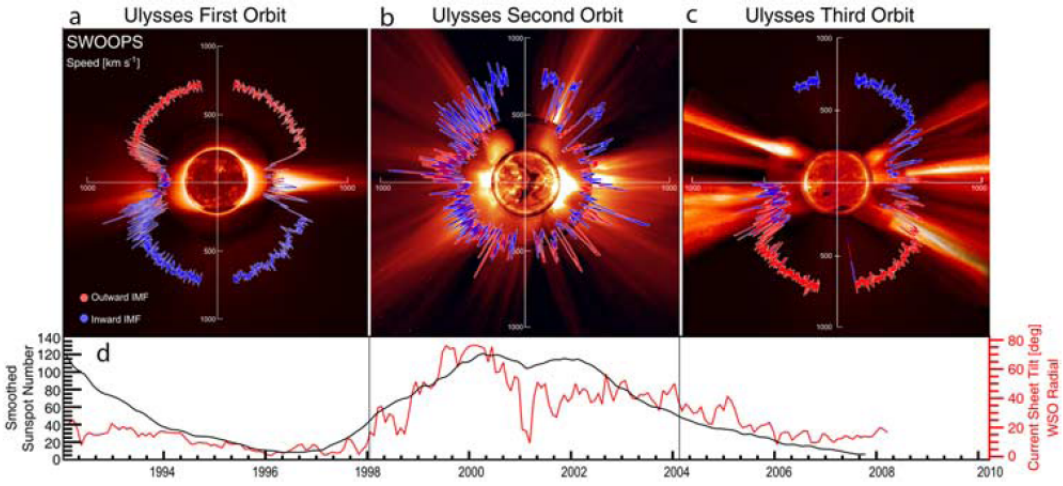

FIGURE 1.4: Latitudinal variation of solar wind speed as observed by Ulysses during its three orbits. Blue and Red colours are used to represent different magnetic polarities. Smoothed sunspot number is plotted in the bottom panel to show the solar cycle variation. Extracted from McComas *et al.* (2008)

1.1.3.2 Solar Wind

Plasma in the outer solar atmosphere is continuously flowing out into the interplanetary space. This stream of particles emanating from the Sun, constituting mainly protons and electrons, is called solar wind. Parker (1958) theoretically predicted the solar wind by showing that the hotter open corona cannot be in hydrostatic equilibrium up to very large distances. His model further demonstrates an acceleration in the solar wind speed from subsonic to supersonic flows due to decreasing gravity with distance. Observational evidence of the solar wind came in 1959 from the Soviet satellite Luna 1. Two types of solar wind are often observed, the slow solar wind and the fast solar wind. The slow solar wind travels at speeds of ≈400 km s^{-1} and is mostly observed near equatorial regions whereas the fast solar wind travels at speeds of ≈800 km s^{-1} and originates from open magnetic field regions such as polar coronal holes. The slow solar wind is found to be more dense and highly variable whereas the fast solar wind is relatively homogeneous and less dense. Figure 1.4 displays the latitudinal variation of solar wind speed as seen by Ulysses during its three orbits until the mission ended. The average sunspot number is plotted in a panel below to demonstrate the solar cycle variation. The magnetic field orientation is represented by red and blue colours.

Clearly, during solar minima, the slow wind is restricted to the equatorial regions and the fast wind is coming from polar regions. But at solar maximum, the distribution is more complex with slow and fast winds emanating from all latitudes. This arises from the fact that during solar maximum, the sources of slow and fast winds such as the streamers and coronal holes get distributed at all latitudes. Note the change in magnetic polarity from one minima to the other. Both fast and slow winds were known to accelerate with distance from the Sun. The acceleration of slow wind can be explained using the Parker's thermodynamic expansion model, but the fast wind was found to accelerate much faster and could not be accounted with this model alone. This suggests the requirement of an additional mechanism to accelerate the fast solar wind.

The solar wind continues to propagate in the interplanetary space, until it reaches the edge of heliosphere where it slows down from supersonic to subsonic speeds. This region is called termination shock region. Beyond this it comes to a pressure balance with the Inter Stellar Medium (ISM) forming a region called heliosheath which ends at heliopause, the outer boundary of the solar system.

1.2 Motivation for the Current Studies

The main energy source for heating the corona and the physical mechanism behind the acceleration of fast solar wind are not clearly understood yet. These are major long-standing problems in solar physics and serve as a common motivation for most of the coronal studies. Our knowledge on these issues is advancing with the recent advent of instruments with high spatial, temporal, and spectral resolutions, which at the same time brought many new problems into light. A few such problems motivated the studies presented in this thesis. Broadly, two different issues are addressed, one connected with the variation of spectral line parameters and the other related to the ambiguity on the nature of propagating intensity disturbances. Detailed discussion on these two issues, is given in following sections.

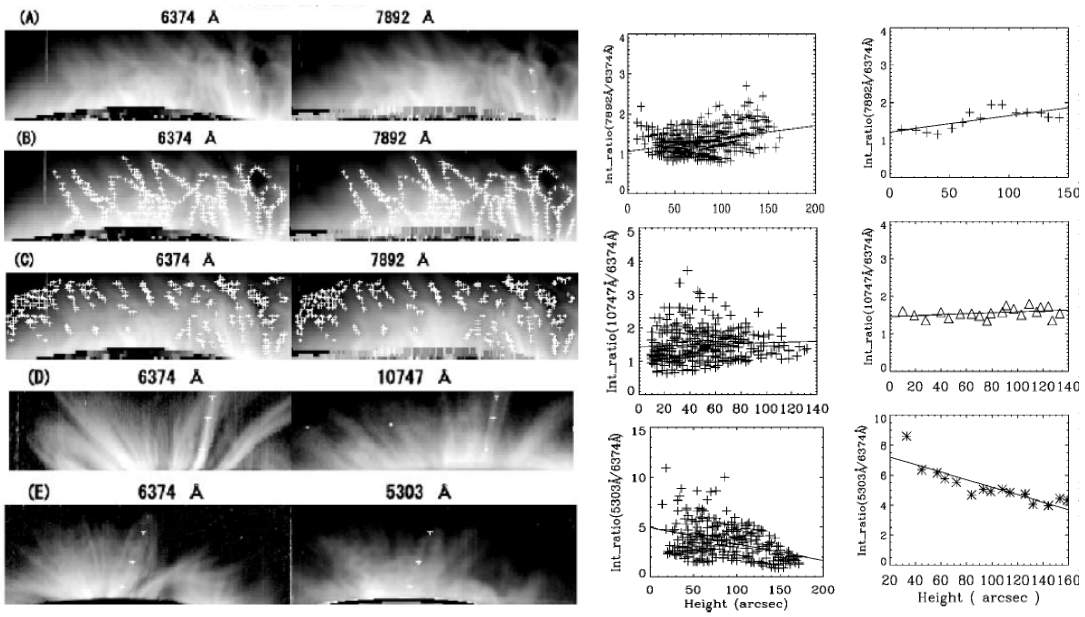

FIGURE 1.5: *Left:* Intensity distribution for the coronal regions observed in pairs of emission lines as marked in each panel. Panels B and C show the region same as that in A, with the locations of loops and the diffuse plasma overplotted. *Middle:* Ratio of intensities plotted against height for the respective line pairs, at all the loop locations selected. *Right:* Plots similar to that in middle for an individual loop structure. In all the plots, solid lines represent the linear fits to the data. Extracted from Singh *et al.* (2004)

1.2.1 Variation of Spectral Line Parameters

Spectral line profiles carry important information from the source. The intensity ratio of a suitably chosen line pair can be used to extract thermal information of the source. Using high resolution spectroscopic data from Norikura coronagraph[1] Singh *et al.* (2004) studied the variation of different line ratios as a function of height above the limb. Observations include raster scans taken simultaneously in pairs of emission lines; one line being [Fe X] 6374 Å and the other line being [Fe XI] 7892 Å, or [Fe XIII] 10747 Å, or [Fe XIV] 5303 Å. Panels A to E of Figure 1.5 display the intensity maps of coronal regions observed in these lines. Several locations along the observed loop structures were manually selected and the same pixel locations were chosen automatically from the other line of a simultaneously observed pair. The intensity ratio was then computed at all these locations and plotted as a function of height. Similar plots were made for the diffuse region

[1]Details on instrument are given in Chapter 2

between the loops. Selected locations corresponding to the loops and the diffuse plasma are overplotted on the observed region in panel A and shown in panels B and C respectively, to demonstrate the selection. The plots in the middle column depict the variation for the loop locations for different line pairs. Similar plots were also made by choosing an individual loop structure and shown in the right column. Overplotted solid lines represent the linear fits to the data. Plots corresponding to the diffuse region are not shown here. All the plots indicate an increase in the Fe XI/Fe X ratio, a moderate change in Fe XIII/Fe X ratio, and a decrease in Fe XIV/Fe X ratio with height. Similar behaviour was found in many other structures observed over a large number of days. These ratios, particularly the Fe XIV/Fe X and Fe XI/Fe X are known to be sensitive to temperature and do not vary much with density (Guhathakurta *et al.* 1993). So, the observations imply a decrease (increase) in temperature along a loop when seen in hotter (colder) lines. To explain this, a gradual interaction between different temperature plasma was proposed. But, it was argued the the Fe XIV and Fe X lines may represent different plasma since their maximum abundance temperatures are widely separated. So it may not be correct to use their ratio to infer the plasma temperature. The temperature variation along a loop is crucial for determining the plasma heating mechanism. Hence, it is important to verify if this behaviour is true. With this motivation, observations were planned and made simultaneously in four emission lines that include Fe XIV and Fe XIII lines. The results obtained using this data are presented in Chapter 3.

Line width of spectral line contains both thermal and non-thermal information of the emitting region. The increase/decrease in line width with altitude, is often associated with the variations in non-thermal component due to undamped/damped waves. Singh *et al.* did an extensive analysis on variation of line width with height using raster scans obtained with the same coronagraph (Singh *et al.* 1999, 2002b, 2003a, 2006a,b). They found that the FWHM of the [Fe XIV] 5303 Å line decreases with height up to $300''\pm50''$ and then remains more or less same up to $500''$, while that of the [Fe X] 6374 Å line increases up to about $250''$ and remains unchanged thereafter. Figure 1.6 shows the observed variation in FWHM with height up to $500''$ for Fe XIV and Fe X lines demonstrating the same. Combining this with their results on variation in intensity ratios, they explain that both temperature and non-thermal velocity vary in the lower corona until they reach a uniform value

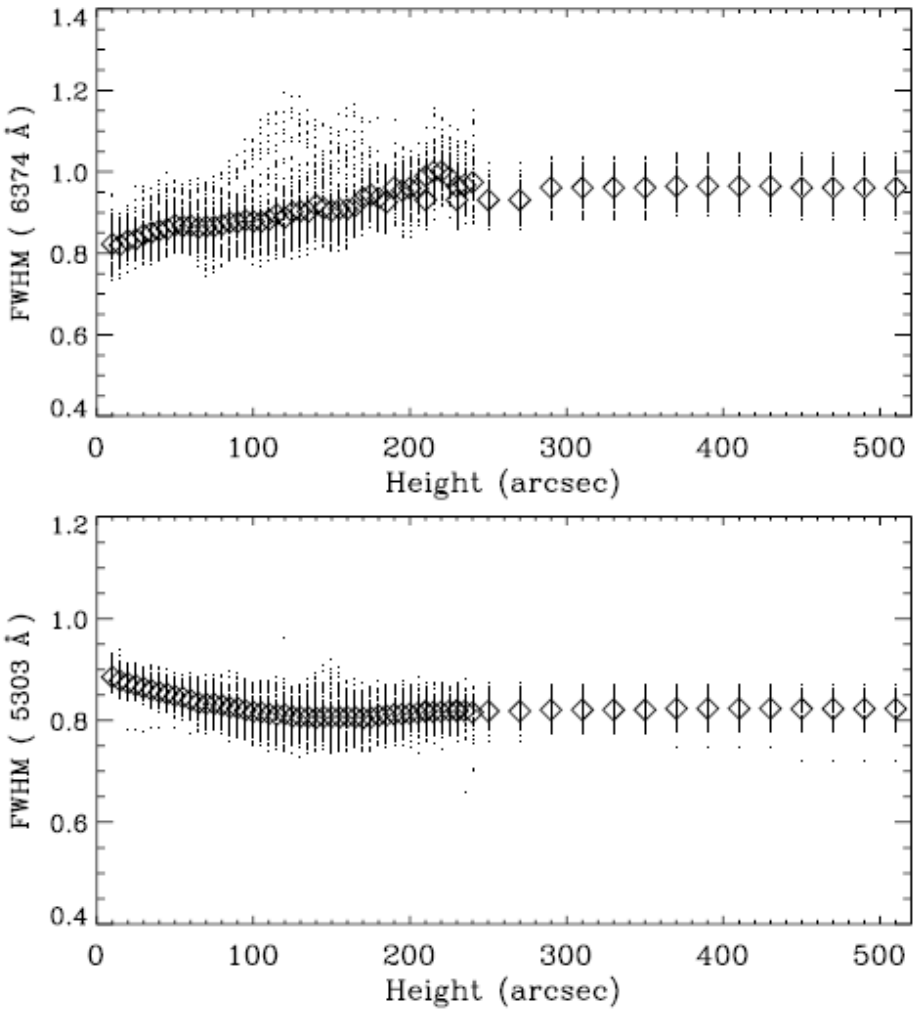

FIGURE 1.6: Variation of FWHM with height for [Fe X] 6374 Å and [Fe XIV] 5303 Å lines. Diamonds represent the mean values at each height with its size chosen according to the standard deviation. Extracted from Singh *et al.* (2006a)

at a certain height that depends on the local conditions. Although the given interpretation fits the observations very well, these studies are mostly restricted to equatorial regions and it has not been explored whether or not these lines behave in the same way in polar regions. Observations that cover mid- and high-latitude regions was used to study this and some interesting results were obtained. These results are presented in Chapter 4.

TABLE 1.2: Statistical properties of propagating intensity oscillations observed in coronal loops with TRACE. Adapted from McEwan and De Moortel (2006)

Parameter	Average	Range
Oscillation period, P	284.0±10.4 s	145–550 s
Propagation speed, v	99.7±3.9 km s^{-1}	O(45)–O(205) km s^{-1}
Relative amplitude, A	3.7±0.2%	0.7–14.6%
Detection length, L_d	8.3±0.6 Mm	2.9–23.2 Mm
Energy flux, F	313±26 erg cm^{-2} s^{-1}	68–1560 erg cm^{-2} s^{-1}

1.2.2 Nature of propagating disturbances

Propagating intensity disturbances were first observed in polar plumes using the white light channel of UVCS/SOHO (Ofman *et al.* 1997). Using observations from EIT/SOHO, Deforest and Gurman (1998) studied several plume structures by constructing evolution charts (a precursor to the space-time maps used now) and found that propagating disturbances are ubiquitously present in the polar corona. These disturbances were found to recur with periodicities of 10–15 min and propagate outward at 75–150 km s^{-1} speeds. The observed properties such as the constant speed throughout the field of view, their repeated nature, their ubiquitous nature and the absence of Doppler blue shifts in the earlier observations of similar structures, prompted them to interpret these disturbances as compressive waves. They also suggested that these disturbances could be slow magnetosonic modes, since the propagation speeds are at or below the local sound speed. Later, Berghmans and Clette (1999) discovered similar disturbances in active region fan loops. Many such observations followed, particularly using imaging data from TRACE (Nightingale *et al.* 1999; De Moortel *et al.* 2000; Robbrecht *et al.* 2001). De Moortel *et al.* (2002a) observed that loops that are situated above sunspot regions show periods of 3 min whereas the non-sunspot loops situated above plage regions show 5 min oscillations. King *et al.* (2003) studied the propagating disturbances in two different temperature channels and observed a decreasing correlation with distance along the structure which implies their different propagation speeds. De Pontieu *et al.* (2005) gave a model suggesting these oscillations as due to leakage of photospheric p-modes into corona. The statistical properties of propagating intensity oscillations observed from TRACE, are listed in Table 1.2 as given by McEwan and De Moortel (2006). The average periodicity

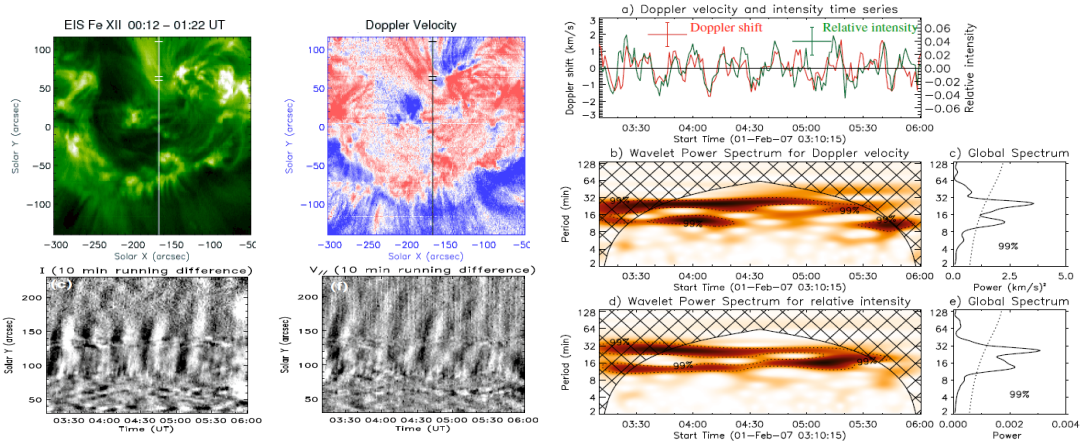

FIGURE 1.7: *Top left:* Intensity and Doppler shift maps of the active region covered by the EIS raster. Vertical line denotes the slit position in sit-and-stare mode. Horizontal cuts mark the analysis locations. *Bottom left:* Time-distance diagrams in intensity and Doppler shift enhanced using a 10 min running difference. *Right:* Wavelet results for the top-cut location shown in the left panel. Extracted from Wang *et al.* (2009b)

is close to 5 min with propagation speeds of the order of 100 km s^{-1}. All these studies suggest that the propagating intensity disturbances observed in both polar plumes and active region fan loops are due to slow magneto-acoustic waves. More recently, Wang *et al.* (2009b) studied these oscillations using spectroscopic data from EIS simultaneously in intensity and Doppler shift for the first time. Figure 1.7 displays the intensity and Doppler shift maps of the active region covered by the EIS raster (top-left panels) from their observations. The vertical line represents the EIS slit location in sit-and-stare mode. A part of the slit is over the fan loop system and is nearly parallel to it. This was the main advantage of this observation that made this study possible. The horizontal cuts marked on the slit are analysis locations. The two panels in the bottom left show the time distance diagrams in intensity and Doppler shift for a part of the slit that covers the fan loops. These are enhanced using a 10 min running difference. These images clearly show propagating disturbances in intensity and Doppler shift. Wavelet analysis plots for the top-cut location are shown in right panel. Two periods 12 min and 25 min are observed. Corresponding light curve in Doppler shift overplotted on intensity (top-right panel) indicates a very good correlation between them. The observed in-phase behaviour of these two parameters further confirmed the slow magneto-acoustic wave nature of these disturbances. But later, De Pontieu and McIntosh (2010) found that these oscillations in intensity and velocity are actually

accompanied by a significant oscillation in line width which is not expected for a slow wave. They demonstrated that this is due to a quasi-periodically varying emission component in the blue wing of the line which is caused by high speed quasi-periodic upflows. This makes it difficult to distinguish these events from slow waves using imaging data alone. According to them, a significant fraction of the previous observations that were interpreted as slow waves, can be actually due to these upflows. Followed by this, Verwichte *et al.* (2010) showed that under certain conditions slow waves may also produce similar variation in line width which created further ambiguity in identifying the nature of propagating disturbances.

Wang *et al.* (2009b) utilized the observed properties of propagating disturbances to obtain the inclination angle of the supporting structure, local sound speed and temperature of the emitting region assuming them to be slow waves. Marsh *et al.* (2009) used the stereoscopic observations of a fan loop structure to measure the true phase speed of a propagating disturbance and obtained temperature from it. They further demonstrated that slow waves can also be used to determine some of the important coronal parameters like magnetic field strength and adiabatic index. These applications coupled with the abundant observations of propagating oscillations, make them useful to advance our knowledge on solar corona. However, it is required to establish the nature of these disturbances, before proceeding to such seismological applications. In this context, several studies were performed and new tools/techniques were developed to understand the true nature of the propagating quasi-periodic intensity disturbances. These results are presented in Chapters 5 & 6.

1.3 Outline of Thesis

This thesis aims to address the problems discussed in the previous section using imaging and spectroscopic data obtained from observational facilities based on both ground and space. Different studies were performed on basic structures like coronal loops and polar plumes and any advancement of our knowledge brought

by these studies will therefore help us in improving our general understanding on solar corona.

Data from a ground based coronagraph, a space-based EUV imager, and another space-based EUV spectrometer, were used in the studies presented in this thesis. It is important to have some basic knowledge on the instrument setup and other details to understand and eliminate many problems in the data that could arise from the instruments. Some of this information along with the reduction steps to prepare the raw data for scientific analysis, is provided for each instrument in Chapter 2.

The general temperature variation along a coronal loop had been studied using a previously unexplored emission line pair. Observed emission line ratios were translated to temperature with the help of an atomic data base available online. The density dependence of these ratios was found to be significant unlike that reported in the literature. Simultaneous observations in four emission lines were availed to take this into account. Results of this investigation are presented in Chapter 3. Variation of emission line width was studied with height in different spectral lines at mid- and high-latitude regions. Comparison with the previous results from equatorial regions revealed an interesting behaviour of green line. The details on this study are given in Chapter 4.

Chapters 5 & 6 deal with the propagating disturbances observed in polar regions and active region fan loops. Different properties of these disturbances were studied using improvised tools/techniques to understand their exact nature. Basic properties like relative amplitudes and propagations speeds were explored in different temperature channels and the results for both polar and active regions are presented in Chapter 5. The possible coherence nature of waves was exploited by taking wider slits in polar regions, to separate them from periodic upflows. Same technique cannot be applied for the active region loops, since they appear to be only a few pixels wide. Simultaneous imaging and spectroscopic data was used to study the AR loops to compensate for this. A technique was developed to improve the measurement of propagation speed, an important parameter for identifying the acoustic nature of these oscillations. Spatial damping in propagating

disturbances was discussed for different open structures in Chapter 6. Powermaps constructed using wavelet analysis revealed an interesting feature which can be explored further to identify the damping mechanism(s) for these disturbances.

The major results of all these investigations are summarised in Chapter 7. Some of the possible future prospects of these studies are also outlined here.

Chapter 2

Instruments and Data Reduction

2.1 Instruments

Data collected from three different instruments were used to address some of the problems explained in Chapter 1. Important information on these three instruments, a space-based EUV imager, a space-based EUV spectrometer, and a ground-based coronagraph, is given in this section.

2.1.1 Solar Dynamics Observatory (SDO)

Solar Dynamics Observatory (SDO; Pesnell *et al.* 2012) is the first mission launched under NASA's Living With a Star (LWS) program, a program designed to understand the causes of solar variability and its impacts on Earth. It was launched from Kennedy Space Centre in Florida on February 11, 2010. The main goal of SDO is to understand the Sun's influence on Earth and Near-Earth space by monitoring the solar interior and different layers of its atmosphere with high spatial and temporal coverage and in many wavelengths simultaneously. The requirement of high spatial and temporal coverage, which implies a large volume of data, led to

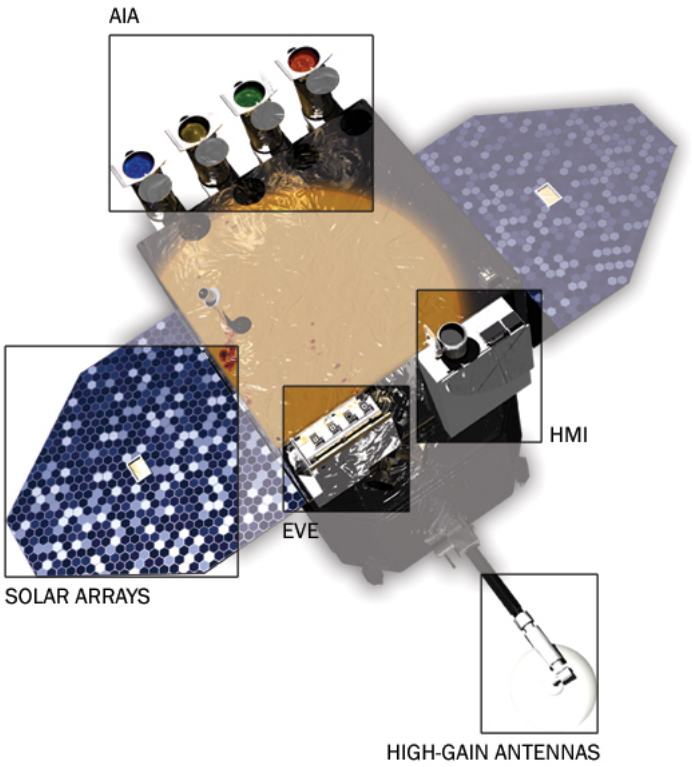

FIGURE 2.1: The SDO spacecraft with all the three instruments onboard highlighted. The high-gain antennas and the solar arrays can also be seen in this figure. *Image credit:* Pesnell *et al.* (2012)

place the satellite in an inclined geosynchronous orbit that allows the contact with a single, dedicated ground station for a continuous downlink. The orbit is inclined at 28.5°, with nearly continuous view of the Sun, apart from two eclipse seasons (due to shadow of Earth) per year during which there will be daily interruptions in the observations. There will also be three more brief interruptions every year due to Lunar transit.

There are three instruments onboard SDO; the Atmospheric Imaging Assembly (AIA) built in partnership with the Lockheed Martin Solar & Astrophysics Laboratory (LMSAL), the Helioseismic and Magnetic Imager (HMI) built in partnership with Stanford University, and the Extreme ultraviolet Variability Explorer (EVE) built in partnership with the University of Colorado at Boulder's Laboratory for Atmospheric and Space Physics (LASP). Figure 2.1 shows the SDO spacecraft

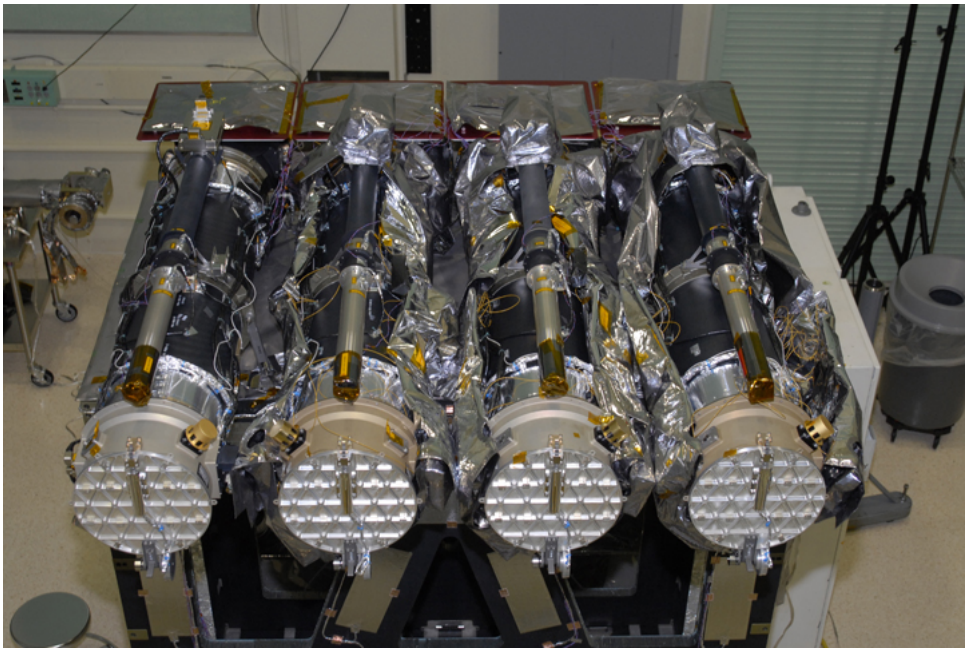

FIGURE 2.2: The four AIA telescopes mounted on the SDO spacecraft during integration at NASA's Goddard Space Flight Centre. *Image credit:* Lemen *et al.* (2012)

with different instruments onboard highlighted. This observatory started its science operations on May 1, 2010 with a planned lifetime of 5 years. The individual instruments are discussed in the following section. Only AIA is described in detail, since the data from other two instruments, were not used in this thesis work.

2.1.1.1 Atmospheric Imaging Assembly

Atmospheric Imaging Assembly (AIA; Lemen *et al.* 2012) is an array of four telescopes that image the solar atmosphere in 10 different wavelength bands nearly simultaneously. Figure 2.2 displays these four telescopes with their individual guide telescopes mounted on the SDO spacecraft during integration at NASA's Goddard Space Flight Centre (GSFC). With a primary aperture of 20 cm, each telescope captures the full disk over a 4k × 4k CCD at a spatial resolution of ≈ 0.6″ per pixel. The circular field of view of diameter 41 arcmin allows the observations up to 0.28 $R_{\odot}$above the limb. A set of seven EUV and three UV-visible channels are being employed out of which four EUV channels have never been

TABLE 2.1: The list of seven EUV and three UV-visible channels used in AIA. The primary ion(s), the region of atmosphere that can observed and their characteristic temperatures are given. Adapted from Lemen *et al.* (2012)

Channel	Primary ion(s)	Region of atmosphere	Char. log(T)
4500 Å	continuum	photosphere	3.7
1700 Å	continuum	temperature minimum, photosphere	3.7
304 Å	He II	chromosphere, transition region	4.7
1600 Å	C IV+cont.	transition region , upper photosphere	5.0
171 Å	Fe IX	quiet corona, upper transition region	5.8
193 Å	Fe XII, XXIV	corona and hot flare plasma	6.2, 7.3
211 Å	Fe XIV	active-region corona	6.3
335 Å	Fe XVI	active-region corona	6.4
94 Å	Fe XVIII	flaring corona	6.8
131 Å	Fe VIII, XXI	transition region, flaring corona	5.6, 7.0

used or used only during brief rocket flights and are expected to open new perspectives of the solar corona. Six of the seven EUV channels observe ionized iron and allow temperature diagnostics of the solar atmosphere from less than 1 MK to 20 MK. For all the ten channels, the primary ion(s) responsible for the emissivity in each channel, the region of atmosphere that can be observed using them and their characteristic temperatures are listed in Table 2.1. Three out of the four telescopes observes the Sun in six channels, two by each, one after the other while the fourth telescope observes C IV (near 1600 Å) and the nearby continuum (1700 Å) along with the 171 Å channel and has a filter that observes in the visible (around 4500 Å) to enable co-alignment with images from other telescopes. The temperature response functions of the seven EUV channels, the arrangement of telescopes, and their observing wavelengths as viewed from the Sun are shown in Figure 2.3. The instrument calibration, wavelength responses and other related information can be found in Boerner *et al.* (2012). The cadence at which images are captured in the standard observing mode is 12 s. However, AIA has the capability to readout small regions of interest, which reduces the cadence up to 2 s for selected wavelength channels to meet specific science objectives such as flare studies.

HMI and EVE are the other two instruments onboard SDO. HMI uses the Zeeman effect of the Fe I 6173 Å line, to measure the Stokes parameters required to make the longitudinal and vector magnetograms of the entire visible disk of the Sun at a

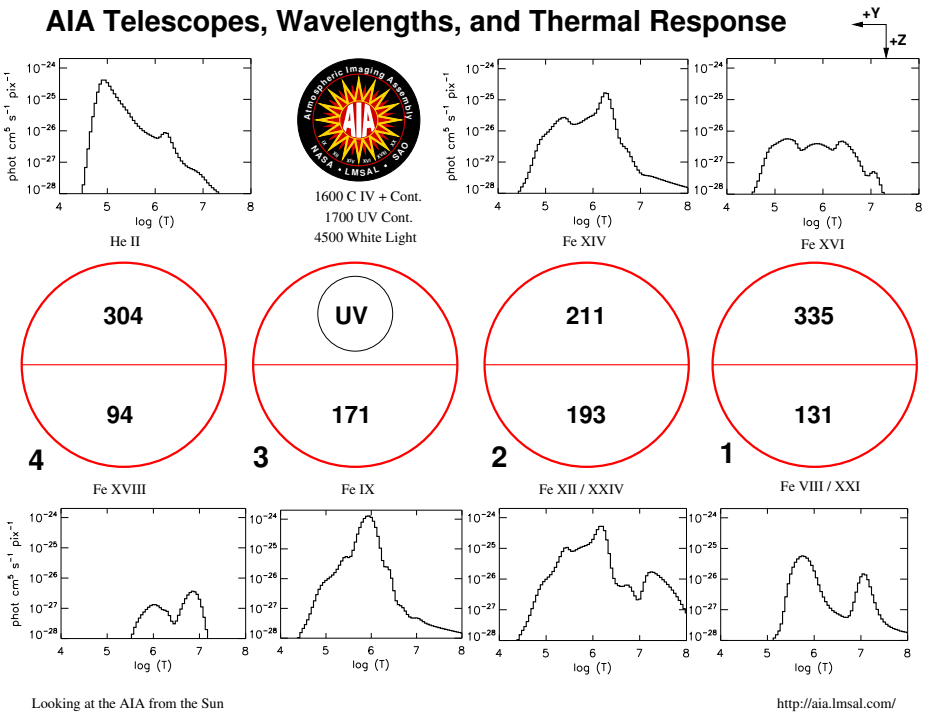

FIGURE 2.3: The thermal response functions of the seven EUV channels, the arrangement of the four telescopes and their observing wavelengths as viewed from the Sun. *Image credit:* http://aia.lmsal.com

resolution of 0.5″ per pixel. It also creates Dopplergrams of the full disk every 45 s at the same resolution using the Doppler shift measured from the same spectral line. EVE measures the solar spectral irradiance in 0.1 nm to 105 nm wavelength range which is the most variable and unpredictable part of the solar spectrum. It also measures the irradiance of Lyman-α at 121.6 nm, the single brightest line in EUV.

2.1.2 Hinode

Hinode, formerly known as Solar-B, is a space-based solar mission developed, launched, and operated by the Institute of Space and Astronautical Science (ISAS) – a division of the Japanese Aerospace Exploration Agency (JAXA), in collaboration with several space agency partners from the United Kingdom and the United States. It was successfully launched on 23 September, 2006 06:36 JST from Uchinoura Space Centre at Uchinoura Kagoshima, Japan. After the launch, the Solar-B

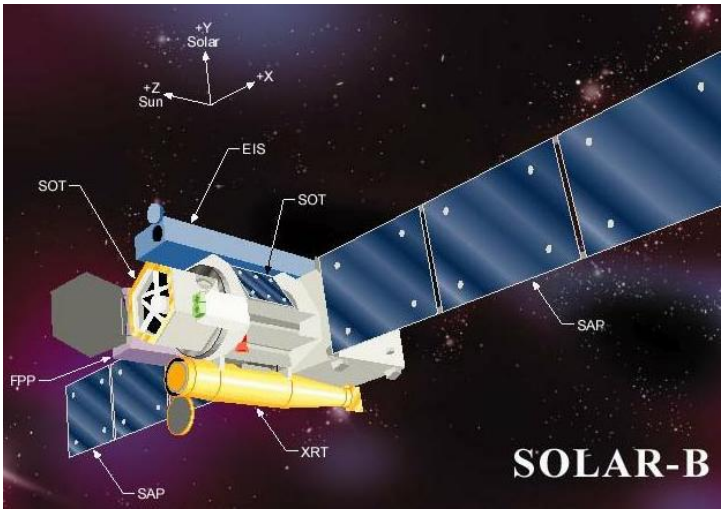

FIGURE 2.4: Hinode spacecraft with the positions of the instruments SOT, EIS and XRT. *Image credit:* JAXA

spacecraft was named Hinode which means *Sunrise* in Japanese. It was kept in a Sun-synchronous circular dawn/dusk orbit with an altitude of 600 km and an inclination of 97.9°. This orbit keeps the instruments in nearly continuous sunlight, with no day/night cycling for nine months each year. It was planned as a three-year mission designed to observe the response of the chromosphere and corona to changes in the magnetic and velocity fields of the photospheric and subphotospheric layers of the Sun. The huge temperature change from about 5,500 K at the Sun's surface to a few million kelvin in the corona, makes it necessary to study the Sun over a broad range of wavelengths. It has three instruments onboard, the Solar Optical Telescope (SOT), the Extreme ultraviolet Imaging Spectrometer (EIS) and the X-Ray Telescope (XRT) that observe the Sun in optical, EUV and X-ray wavelengths respectively. Figure 2.4 shows a cartoon image of the Hinode spacecraft with the three instruments onboard. The focal plane package (FPP) which is part of SOT and the solar arrays can also be seen in this figure. SOT is used to make quantitative measurements of all the three components of the magnetic field at the surface and the response of the solar atmosphere to changes in the magnetic field is measured by the EIS and XRT. Detailed information on the spacecraft design, its operations, and scientific objectives, can be found in Kosugi *et al.* (2007). In the following section, the spectrometer EIS is described in detail, since the data obtained from it form a part of this thesis.

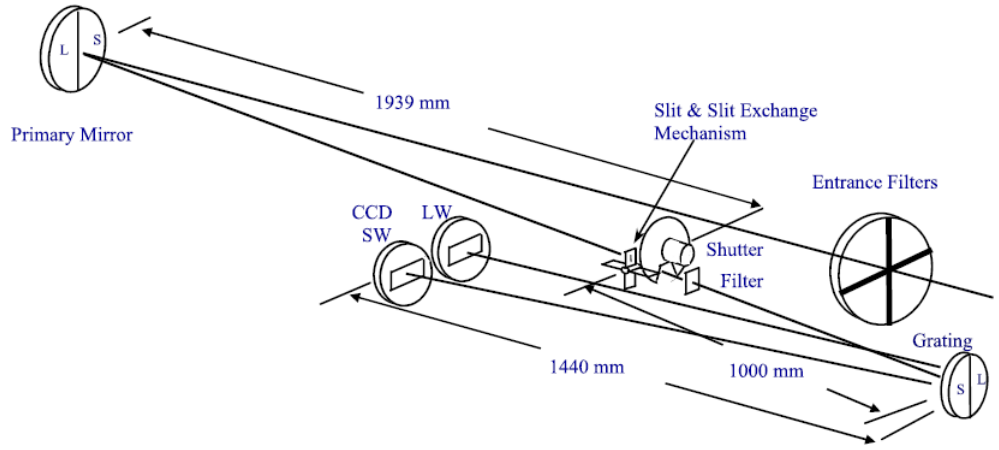

FIGURE 2.5: Optical layout of the EIS spectrometer. S/SW and L/LW refer to short and long wavelength bands respectively. *Image credit:* Culhane *et al.* (2007)

2.1.2.1 EIS

Extreme ultraviolet Imaging Spectrometer (EIS; Culhane *et al.* (2007)) is one of the three major scientific instruments onboard Hinode that is designed to observe emission from upper transition region and corona in the wavelength ranges 170 – 210 Å and 250 – 290 Å. The telescope has a unique two element, normal incidence design with an off-axis paraboloid primary of diameter 15 cm and focal length 1.9 m. Light enters the telescope through a thin 1500 Å Al filter which blocks the transmission of visible radiation. The primary mirror focuses the EUV radiation from the Sun onto a spectrograph slit. Light passing through the slit is dispersed and stigmatically re-imaged by a toroidal concave grating onto two 1024 × 2048 pixel CCD detectors, each covering 40 Å with the longer dimension of the detector in the dispersion direction. Both mirror and grating are applied with Mo/Si multilayer coatings for high reflectivity. To broaden the spectral range, the multilayer-coated optical elements were divided into two D-shaped sectors. The coating in each sector is tuned to produce high reflectivity in either of the wavelength bands 170 – 210 Å and 250 – 290 Å. This differential tuning is applied to matching halves of mirror and grating. Exposure times are controlled by a rotating shutter. Another small Al filter is placed behind the spectrometer slit to reject out of band light that might leak through pinholes. The complete optical layout of the spectrometer is shown in Figure 2.5. An interchange mechanism at the

telescope focal plane allows selection among four possible apertures, two slits of 1″ and 2″ width and two slots of 40″ and 266″ width. A piezoelectric drive system which rotates the primary mirror permits raster scanning with slits to produce spectroheliograms. Alternatively, slots can be used to obtain images of large areas in bright solar emission lines with a single exposure. However, spectral information is lost in the latter case. The overall field of view of the instrument is set by the usable slit height (8.5 arcmin) and the raster scan range (6 arcmin) in the dispersion direction. The centre of the field of the view is normally determined by the spacecraft pointing, but there is a coarse mechanism that can offset the primary mirror by ±15 arcmin from the pointing axis in E-W direction. This enables EIS to see a high-altitude region of the corona at the limb when the nominal observing region of Hinode is located near the centre of the sun. The spatial resolution of the instrument is 2″ (2 pixels) and the spectral resolution is 47 mÅ at 185 Å (Each spectral pixel corresponds to 22 mÅ). Numerous emission lines in the short and long wavelength bands cover a temperature range from about 0.05 MK to 20 MK and selection up to a maximum of 25 spectral lines is allowed in an observation. EIS can measure velocities of bulk plasma motions as small as ± 5 km s^{-1}. It can be used for measuring plasma flow velocity, temperature, and density in the region between the photosphere and corona using a multitude of spectral lines that can be observed simultaneously.

SOT is the largest of the three telescopes onboard Hinode, with 50 cm primary aperture. Three optical instruments at the SOT focal plane, the Broadband Filter Imager (BFI), the Narrowband Filter Imager (NFI), and the SpectroPolarimeter (SP), together known as Focal Plane Package (FPP), provide us diffraction limited images (≈0.2″ resolution) of the photosphere and chromosphere along with precise Dopplergrams and vector magnetograms over a subfield. The ability to make continuous, seeing-free, diffraction limited observations with enhanced stability using active image stabilization, is the highlight of SOT. XRT is a grazing incidence high resolution X-ray telescope that images the coronal plasma over a broad range of temperatures ($6.1 < \log T < 7.5$) using several narrow band filters. In addition, it also has the facility to take images in G-band for alignment purposes.

2.1.3 Norikura Coronagraph

Coronagraph is a specially designed telescope to facilitate longer duration optical observations of the solar corona by artificially blocking the disk light. Coronal light is a million times fainter than the radiation coming from the disk and the competing sky brightness due to atmospheric scattering makes the observations from ground limited to high-altitude sites with clear sky. Norikura solar observatory[1] was established in 1949 at the 2876 m summit of Norikura mountain located in the Northern Alps, Japan. This observatory has three coronagraphs, two 10 cm coronagraphs and a 25 cm coronagraph. One of the 10 cm coronagraphs was built in 1950 for continuous coronal observations in green line (5303 Å). The other one was built in 1990 for high sensitivity photometric observations of the solar corona using four different filters. The 25 cm coronagraph was built in 1971 for spectroscopic observations and was accepting proposals from the scientific community to plan and make observations until the observatory was shut down in 2009. This telescope uses a coude system, and the solar beam is led through the polar axis to the spectrograph room. The spectrograph setup can be changed according to the observational needs. For the work presented in this thesis, observations with this coronagraph were made by Prof. Singh, simultaneously in 2 to 4 emission lines. The required spectrograph setup was also made by him with the help of the staff at Norikura. The main setup had evolved over time but the key elements of the setup used for simultaneous observations in 4 lines is described below. Details on the initial setup for 2 lines are discussed in Singh *et al.* (1999, 2003a).

The 25 cm coronagraph had a provision to use doublet or singlet lens for imaging the sun and solar corona. This coronagraph with effective focal length of 8.80 m forms an image of the solar corona on the slit of the Ebert-Fastie type spectrograph with a scale of 25 arcsec/mm. After making the spectroscopic observations in two coronal emission simultaneously during the period 1997 – 2003, the need was felt to make observations in 4 emission line simultaneously. The feasibility study was made to mount another CCD camera and simulations indicated that the 4th order green emission line and 2nd order IR lines at 10747 Å and 10798 Å are conveniently located to mount two CCD cameras side by side and a third CCD camera at the

[1] http://solarwww.mtk.nao.ac.jp/en/norikura/norikura.html

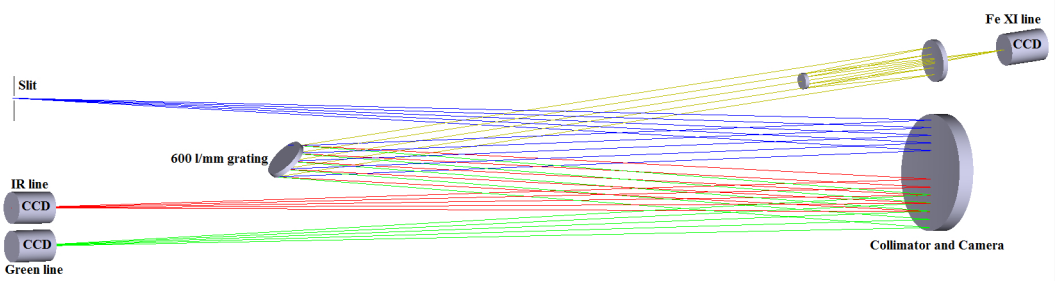

FIGURE 2.6: A schematic representation of the spectrograph setup at Norikura coronagraph. Different elements are labelled.

spill over diffracted light to record the spectra around [Fe XI] emission line at 7892 Å. The coude type coronagraph and large spectrograph of 7 m focal length permitted to mount these three cameras, two at the Littrow focus and the third at a part of the diffracted beam from the grating which spills over the collimating mirror. The optical arrangement of the spectrograph is shown in Figure 2.6. A new mechanical set up was designed accordingly and was fabricated to mount both the cameras at the Littrow focus for obtaining the spectra in the green and IR emission lines. A 20 cm Cassegrain telescope was used as camera optics to focus the [Fe XI] emission line spectrum on the third camera without any vignetting in the image. The IR lines are imaged over a 1024 × 1024 format detector with pixel size 24 microns and the other lines were imaged over a 512 × 512 format detectors. These detectors cover 500″ along the length of the entrance slit and 7 to 60 Å in wavelength depending on the lines and order of the used spectra. For this combination of emission lines, the 10747 and 10798 Å lines in the second order, the 7892 Å line in the third order, and the 5303 Å line in the fourth order were used to obtain the spectra. To save time for readout and data transfer the recording of spectra was restricted to about 6 Å around the green line, about 5 Å in the case of the [Fe XI] line and about 55 Å around the IR emission lines. A slit width of 200 microns corresponds to 5″ on the solar image. The dispersion values are 19.3 mÅ pixel^{-1}, 40.3 mÅ pixel^{-1}, and 74.2 mÅ pixel^{-1}, for the green, [Fe XI], and IR emission spectra, respectively.

The coronal region for making observations was selected on each day, by looking at the full disk green line images of the solar corona obtained with the 10 cm coronagraph. By changing the inclination of the glass block installed in front of

the entrance slit, spectra at successive positions were obtained to cover a two-dimensional region. A raster scan of the inner corona consisting of 50 positions with steps of $4''$ and an exposure time of 30 s could be completed in about 30 minutes. Observations were made both at polar and equatorial regions. Exposure times were varied depending on the emission line, target region and sky conditions. Even with the different exposure times, the spectra in different lines started at the same time at a given location. The CCD camera with short exposure time had to wait for the camera with long exposure time to complete before taking a new exposure. All the computers were interlinked to make the observations. In this way, spectroscopic data were collected over a two dimensional region, on a number of days, simultaneously in 4 coronal emission lines.

2.2 Data Reduction

Before one starts analysing the data, certain corrections are needed to be done on the raw data. Some standard procedure is usually followed to apply these corrections and to transform the data to a more useful form. This process is called data reduction. The steps to follow and the corrections needed vary with the instrument and the type of observation. The reduction procedure followed for the data used in this thesis work is described in this section separately for each instrument.

2.2.1 AIA

There is no onboard storage of data for the SDO mission. Instead, the data are transmitted continuously from the spacecraft to two dedicated ground stations located near White Sands, New Mexico using its high-gain antennas. The data transmission rate is about 130 Mbits per second. From the ground stations, the AIA and HMI data are transferred to the Stanford University campus where the AIA images are assembled from the telemetry packet data decompressed, and then stored using lossless Rice compression in the Joint SDO Operations Centre

(JSOC) science-data processing (SDP) facility. The data recorded at the JSOC-SDP are labelled as Level 0. These images are used to generate higher-level data products that include browse-quality data. Generation of Level 1 images involve the following corrections:

- In the first step, all the over-scan rows and columns, if any present, are removed. These are not real, but contain the charge remaining after 2048 parallel (serial) transfers and are only occasionally included to monitor the CCD charge transfer efficiency.

- The dark image is then subtracted to account for the digital offset and dark current of the CCD. The dark current is usually low for exposures of few seconds, as the CCD is maintained at very low temperatures.

- Each image is then corrected for the pixel to pixel variations on the detector using a flat-field image. Sources of these variations include, gain differences, vignetting, and shadowing caused by the focal-plane filter support mesh. Flat-field images are acquired on orbit regularly.

- The bad pixels that do not correctly respond to light are removed at this stage and their values are replaced with interpolated values from neighbouring pixels. These pixels were found to be very less ($< 0.1\%$) in number, but can increase with time.

- Cosmic spikes are removed. These are typically sharp isolated features that can be as small as one pixel or may in some cases leave a streak of deposited energy in many adjacent pixels. These locations are replaced with the median value of neighbouring pixels. There is a provision to undo this step.

- Each image is then flipped to put solar North at the top of the array.

These corrections are sufficient to produce calibrated AIA images. The processed images are then made freely available for public access at JSOC in FITS format. However, different AIA channels have different plate scales and roll angles, and the image orientation achieved in Level 1 processing may not be accurate, as it is done using the pointing information. This can make the multi-wavelength analyses, one of the key features of AIA, problematic. To get rid of these issues, Level 1 data can be further processed using the routine `aia_prep.pro` available through Solar SoftWare (SSW). This routine coaligns images from all of the AIA channels, rescales the images to a common plate scale (0.6″ per pixel), and derotates the image so that the solar east-west and north-south axes are aligned with the horizontal and vertical axes of the image, respectively. The product images are then labelled as Level 1.5. These images can be used for any further analysis. Further information on the Level 1 processing steps can be found at Lemen *et al.* (2012). Additional information on retrieval and processing of AIA data can be accessed from SDO user guide available at LMSAL site[2].

2.2.2 EIS

Hinode is open to the scientific community to propose and make observations according to their scientific needs. In addition, the data will not be restricted to the observer, rather open to the whole community. The data recorded during observations are stored onboard Hinode satellite. When the downlink opportunity comes, the data are downloaded at two ground stations Uchinoura station(USC) in Japan and Svalbard station in Norway. Raw data in the CCSDS packet format, are archived in the SIRIUS database at ISAS/JAXA. The Hinode team constructs FITS files from the raw data and provides to users. These FITS files are labelled as Level 0 and needs to be calibrated/corrected before using them for scientific analysis. Following are the corrections required for the EIS data to transform them into Level 1 usable files.

[2] http://aia.lmsal.com

- First step is to flag any saturated data. CCDs used for EIS have a 14 bit dynamic range and so saturation occurs at 16,383 data numbers (DN). All such pixels are flagged as missing.

- Subtract the CCD bias and dark current. The fixed CCD pedestal and the dark current can be subtracted using a dark frame, but it was found that the dark current varies in the orbit due to the CCD temperature changes. So, usually the dark counts to be subtracted are estimated from the science exposures themselves. Note that this subtraction can result in pixels with negative DN values which also need to be flagged as missing.

- Flag the hot pixels, warm pixels and cosmic ray spikes. Hot and warm pixels always show anomalously high DN values. These pixels are identified from the inspection of 100 s dark exposures that are generated approximately every week. Cosmic spikes can be located by setting some threshold level above the mean values.

- Several small pieces of dust accumulated on the CCD before launch and are found to completely block the signal on the CCD at their locations. They are at fixed positions and cover less than 0.1% of the CCD. However two of the pieces are the large enough to cover 15 to 30″ spatial ranges in solar-Y and affect the strong lines such as Fe XI 188.23, 188.30 and Fe XII 193.51. These pixels are called dusty pixels and need to be flagged.

- Optionally, the DN values can be converted to absolute intensities. When this is done, the degradation of EIS sensitivity has to be taken into account.

The `eis_prep.pro` routine available through SSW takes care of all these corrections and outputs the data in Level 1 form. It also estimates 1-σ errors associated with the calibrated intensities and outputs in a separate file. All the flagged pixels are usually replaced with the median of the neighbouring pixels and are assigned a value of -100 in the error file. The slot images can be directly used for analysis

after this step. The spectral data, however, needs a couple of important corrections before proceeding to extract the important parameters, peak intensity, line centre, and line width, by fitting a Gaussian. The EIS slits are tilted relative to the axes of the CCDs, resulting in a systematic shift in the line centre along the slit. This tilt was found to be more for 2″ slit compared to 1″ slit. For both the slits, the shift is considerable and can affect the Doppler shift measurements. Also as the spacecraft orbits the Earth, the instrument receives a variable illumination from Earth which will lead to periodic fluctuations in temperature. The temperature changes in the vicinity of the grating leads to a small rotation in the grating position. This in turn causes periodic shifts in the line positions. The amplitude of these oscillations is about ± 1.5 pixels, which causes Doppler shifts that can submerge the real motions on the Sun. The routine `eis_auto_fit.pro` available through SSW corrects for both these effects and computes the Gaussian parameters from the spectra. This routine is very flexible to implement multi-Gaussian fits, parameter limits, and parameter tying, whenever needed. The line width measurements can be corrected for instrumental width using some EIS routines.

There is a physical offset between two CCDs and a difference in grating tilt with respect to the two CCDs which together amount to an offset of 18.5 pixels in the Y-direction between the short wavelength (SW) and long wavelength (LW) CCDs. This needs to be corrected for some studies such as the derivation of densities from lines separated in wavelength. Detailed information on the individual corrections and the usage of several routines to process and analyse EIS data can be accessed from the EIS Wiki page[3] or from the software notes available through SSW.

2.2.3 Norikura Coronagraph

The data observed with the Norikura coronagraph, are usually stored in PMI format. Most of the observations comprise of raster scans, in which a slit is exposed at a position to record the spectra and then image is moved to adjacent positions to build the spectral information over a two dimensional region. Spectral image of the slit obtained from each exposure is stored in a PMI file and can be

[3] http://msslxr.mssl.ucl.ac.uk:8080/eiswiki/

read using specific routines written by the Norikura team. Steps given below may be followed to prepare Norikura data for scientific analysis.

- Bias and dark current should be subtracted. Dark frames are usually taken immediately after the observation by allowing the CCD to accumulate charge with the shutter closed, for the time equal to the exposure time of the spectra. These frames can be used for bias and dark subtraction.

- Spectra should be freed from pixel to pixel variations. The gain differences between different pixels can be normalized using the flat spectra that are taken as a part of the observation. A uniform source is required for taking the flat spectra. This is achieved by replacing the slit with a slot and pointing to the disk centre after the occulter is removed. Sometimes the grating is rotated in 4 to 5 steps to take different flats and merge them to remove any remnant absorption feature in the flat.

- Remove the scattered light component due to sky brightness. Although the solar disk is blocked, the light scattered in the Earth's atmosphere enters the telescope and becomes a significant component in the observed spectra. In addition there is scattered light due to the instrument. This can be subtracted by matching the absorption lines and continuum in the observed spectra with that of a disk spectra taken immediately after the observation.

- Perform wavelength calibration for the spectra. The absorption line in the disk spectra taken during the observation can be matched with an atlas spectra to find the dispersion and wavelength at each pixel position.

- Fit a Gaussian to extract the line parameters. This can be done using some standard routines. Some of the emission lines have an absorption line in its profile. This must have been removed during sky subtraction but any remnant left can affect the fitting. Those pixel locations should be carefully discarded while fitting.

- Correct the line width measurements for instrumental width. Instrumental width can be computed from the width of a weak absorption line in the disk spectra.

- Convert the DN values to absolute intensities. This can be done by comparing the average counts in the disk spectra with the standard solar flux at those wavelengths and using the same factor for the coronal values. Filter transmission percentage should be taken into account while computing these values.

- Finally spectroheliograms, Dopplergrams, and line width maps, can be constructed for the observed region. But the images in different lines may have different scales due to the differences in focal lengths of the optics used. These can be rescaled and brought to the same spatial scale using disk spectra obtained during observation with three fiducial marks.

A library or routines provided by the Norikura team is employed to make these corrections for the data used in this thesis work.

Chapter 3

Thermal Structure of Coronal Loops

The solar corona is highly structured with plasma confined to magnetic threads called coronal loops. It is important to study the physical properties of coronal loops and their variation along and across the length of a loop, to improve our understanding on solar corona. In particular, the temperature variation plays a crucial role in determining the exact plasma heating mechanism. To study this, high resolution spectroscopic observations of the off-limb corona obtained with the 25 cm Norikura coronagraph, located at Norikura, Japan, were used. Observations were made simultaneously in multiple iron emission lines in the visible and IR part of the electromagnetic spectrum. Using the temperature sensitive emission line pairs, (Fe XIV 5303 Å, Fe XIII 10747 Å) and (Fe XI 7892 Å, Fe X 6374 Å), the electron temperatures along 18 different loop structures were computed. For the loops studied using the former line pair, the temperature was found to decrease towards the apex in contrary to the theoretical expectations while those studied using the latter line pair are in agreement. Combining these results[1] with that existing in the literature, the general variation in temperature observed and its physical implications are discussed in this chapter.

[1]Results of this work are published in Krishna Prasad *et al.* (2013)

3.1 Introduction

Coronal loops are considered as the basic building blocks of the solar corona and any improvement in the knowledge on these loops, like the exact thermal structure of a coronal loop and other such properties, can therefore help us in solving several long-standing issues related to corona (for *e.g.* coronal heating). The temperature profile is of particular importance, due to its direct relation with the underlying plasma heating mechanism. So, how does the temperature of a coronal loop vary along its length? Theoretical models were developed several decades earlier, but the observations became progressive only in the recent past with the advent of the improved instrumentation and technology. Rosner, Tucker, and Vaiana, made one of the earliest attempts to propose a theoretical model for the coronal loops, which is widely known as RTV model. They derived scaling laws between temperature, pressure, and length of a loop and demonstrated that in a uniformly heated, stable, hydrostatic loop the temperature maximum must be located near its apex (Rosner *et al.* 1978). This model was later generalized by Serio *et al.* (1981), to long loops, by including the variation of pressure and heat deposition along the loop. Kano and Tsuneta (1996) derived temperature distribution in 16 steady loops observed with *Yohkoh* in soft X-rays and found that the temperature is highest around the loop top and decreases towards the foot points consistent with these models. Similar studies on cooler EUV loops, however, showed a little or no temperature variation along the loop which was not in agreement with the static loop models (Lenz *et al.* 1999; Aschwanden *et al.* 2000). Different theories were proposed to explain this isothermal nature. Reale and Peres (2000) suggested that a superposition of several unresolved thin strands at different temperatures can produce a flatter temperature profile in the observed loop. Aschwanden *et al.* (2001) proposed that the heating for long EUV loops may not be uniform and most part of it might be concentrated at the foot points resulting in the near isothermal loop structure. Another theory suggests that similar results can be obtained if the loops observed are non-static with significant flows inside (Winebarger *et al.* 2002). Non-uniformity in the loop cross section was found to be another possible explanation. The temperature profile can be isothermal if there is a significant decrease in cross-section of the loop near the foot points (Landi and Feldman 2004). A few other studies (Schmelz 2002; Del Zanna and Mason 2003; Reale and

TABLE 3.1: Details of observations

Date	Target region	Observation time (JST[1])
2005 Sep 21	West limb	09:28 – 09:50
2005 Oct 3	East limb	08:28 – 08:47
2005 Oct 6	East limb	06:05 – 06:41
2007 Oct 6[2]	West limb	11:57 – 12:29

[1] Japanese Standard Time
[2] Observed only in two lines Fe XI 7892 Å and Fe X 6374 Å.

Ciaravella 2006) disagree on the observed isothermal nature itself! More recently, Tripathi *et al.* (2009) observed an increase in temperature of a coronal loop with around 0.8 MK near its base to 1.5 MK close to its apex, by carefully subtracting the background emission. So, the observations themselves are not very consistent. Moreover, the main focus, in the recent years, had been shifted to the cross-field thermal structure of the loops. In this context, spectroscopic data obtained with the Norikura coronagraph was used to study the temperature variation in coronal loops, particularly along their length.

3.2 Observations

Spectroscopic observations of the off-limb corona were made on several days using the ground-based Norikura coronagraph located at Norikura, Japan. The observations were carried out simultaneously in four forbidden iron emission lines namely, [Fe XI] 7892 Å line, [Fe XIII] 10747 Å & 10798 Å (IR) lines, and [Fe XIV] 5303 Å line, using three different CCD cameras (spectra in both the IR lines were imaged on a single CCD). In addition to these, some observations were made simultaneously in only two lines, [Fe XI] 7892 Å and [Fe X] 6374 Å. Simultaneous observations in these lines were planned and obtained by Jagdev Singh in view of the observed complex nature of intensity ratios (Singh *et al.* 2004). The detailed instrumental setup is discussed in Section 2.1.3.

Four different raster scans, with relatively better signal-to-noise, were chosen for this study. Observation time and the target region for these four scans are listed

in Table 3.1. First three scans were observed simultaneously in four lines and the last scan was observed only in two lines. We refer to these two sets as set I and set II respectively, for the rest of the chapter. The slit length was around 500″ and the width was kept at 5″ for the scans in set I and 3″ for those in set II. Each scan covers a portion of the equatorial off-limb corona of about 200″ × 500″ size. Exposure times were varied from day to day and also between different lines from 25 s to 50 s depending on the target of observation to get good signal. This translates to a duration of 20 min to 35 min to complete a single scan (see Table 3.1). Disk spectra were obtained immediately after or before the scan, by keeping the slit at the centre of the solar disk. Corresponding dark and flat spectra were taken after each set of observations. Reference slit images (wire spectra) were also taken with the same setup by keeping three wires across the slit at a fixed known distance to correlate the spectral images obtained in different lines.

3.3 Data Reduction and Analysis

The data were prepared following the standard reduction procedure for the Norikura datasets[2]. Each spectral image had been corrected for the dark current and pixel to pixel variations using the corresponding dark and flat images. Scattered light component in the spectra was subtracted using the disk spectra. One of the scans in set I (taken on 2005 October 6) was binned on two pixels in spectral dimension to improve the signal-to-noise. The dispersion values at each CCD was computed by comparing the corresponding disk spectra with the standard solar spectra. The dispersion values for the scans in set I are 40.3 mÅ pixel^{-1}, 74.2 mÅ pixel^{-1}, and 19.3 mÅ pixel^{-1}, respectively for Fe XI, Fe XIII, and Fe XIV lines (twice the values for the binned case) and the values for those in set II are 23.6 mÅ pixel^{-1} and 26.6 mÅ pixel^{-1} respectively for Fe XI and Fe X lines. All the spectra were fitted with a single Gaussian profile and the parameters such as amplitude (peak counts), peak position, and line width, were derived. Only those spectra, with a signal-to-noise ratio 5 or greater, are considered. Gaussian amplitudes were converted to absolute intensities using the disk spectra and standard solar flux

[2]Step-to-step reduction procedure is described in Section 2.2.3. The information relevant only to the current dataset is given here.

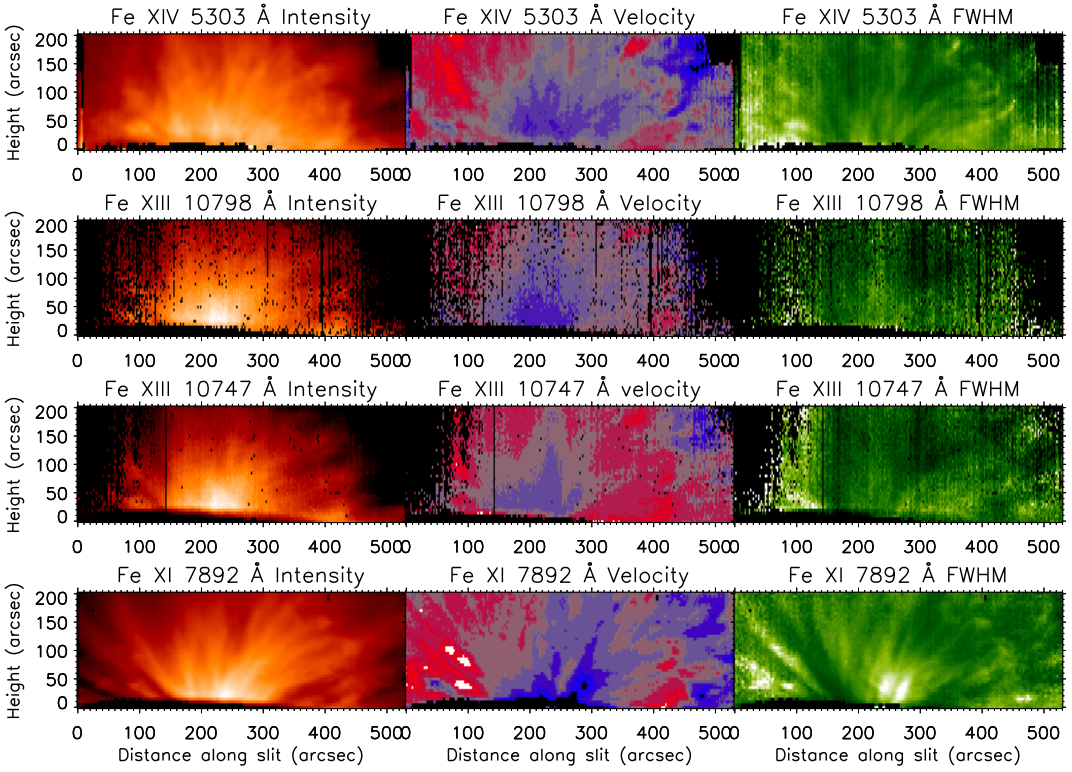

FIGURE 3.1: Intensity, Velocity, and FWHM maps of a coronal region in all the four lines observed simultaneously on 2005 September, 21.

values at respective wavelengths. The total area under the fitted Gaussian curve is taken as the total intensity in the line profile which is used in this analysis. Peak positions were converted to Doppler velocities taking the average position in the scan as reference. Line widths were converted to FWHM after correcting for the instrumental broadening as explained in Prasad *et al.* (2013). A 2-D monochromatic image of the observed region was then constructed in each of these parameters. Spatial scale of these images in each spectral line is not same due to different focal lengths of the optics used to focus the spectra. This is also affected by the differences in pixel sizes of detectors. These images were therefore aligned and brought to same spatial scale using the wire spectra in each line. The pixel scale after this correction is found to be $\approx 2.2''$ per pixel for the scans in set I and $\approx 2.4''$ per pixel for those in set II. However, the spatial resolution in the scan direction is limited by the slit width. After performing all these corrections, final images of a coronal region constructed from intensity, velocity, and FWHM of the four emission lines corresponding to a scan taken on 2005 September 21, are shown in Figure 3.1. These images show distinct loop structures clearly visible in

Fe XI line. The temperature profiles along these loops can be computed, by using temperature sensitive emission line ratios. In order to do that, first one needs to prepare a calibration curve with modelled intensities at different temperatures and use that to translate the observed intensity ratios to temperature values. This process is performed for 18 loop structures identified in all the scans as explained in the following sections.

3.3.1 Translating Emission Line Intensity Ratios to Temperature

Emission line intensity ratios from a suitable line pair can be used to extract thermal information of the source. For accurate estimation, while choosing the emission lines, it has to be ensured that the emission in both the lines is coming from the same plasma volume. The line pairs (Fe XIV 5303 Å, Fe XIII 10747 Å) and (Fe XI 7892 Å, Fe X 6374 Å) were chosen in the present study due to the closeness in their maximum abundance temperatures[3]. These line ratios are also known to be sensitive to electron temperature and weakly dependent on density which means that any change in the temperature will be reflected in the ratio of the observed intensities. For instance, the theoretical calculations by Srivastava *et al.* (2007) indicate the Fe XIV/Fe XIII line ratio to be temperature sensitive and a weak function of density. A model had been developed for the temperature dependence of these ratios using CHIANTI (version 7.1; K.P. Dere *et al.* (1997); Landi *et al.* (2012)). The calculations are done at constant density using the coronal abundances of Schmelz *et al.* (2012) and ionization fractions of Arnaud and Raymond (1992). Photo-excitation[4] from a radiation field of temperature 6000 K at a distance of 1.1 $R_{\odot}$ is included. A calibration curve is constructed with the modelled intensity ratios for a range of temperatures at a particular density. Similar calibration curves were also produced for different densities varying from $10^{7.5}$ to $10^{9.0}$ cm^{-3} in steps of 0.1 in the log scale to check if there is any density dependence. The constructed curves for both the line pairs are shown in Figure 3.2

[3]The temperatures of maximum abundance for the ions Fe XIV, Fe XIII, Fe XI, and Fe X are 2.0 MK, 1.8 MK, 1.4 MK, and 1.1 MK respectively, as noted from the atomic database CHIANTI

[4]This process is important for IR lines.

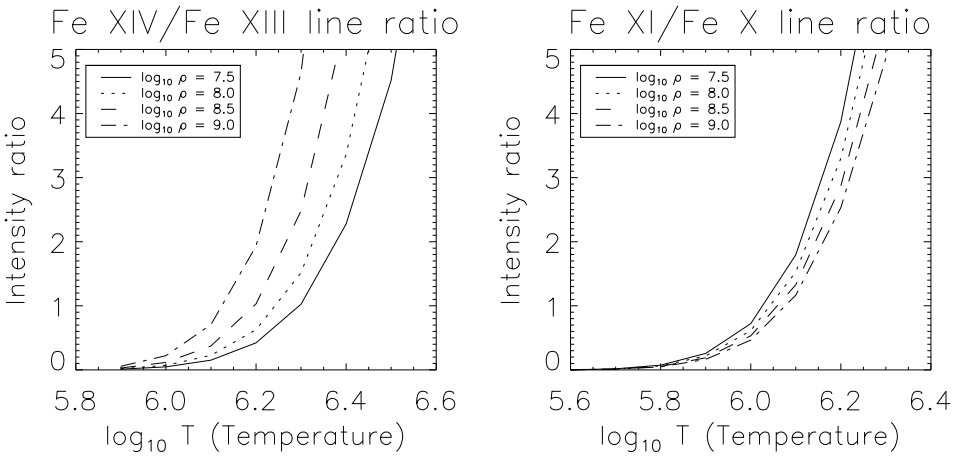

FIGURE 3.2: Variation of emission line ratios Fe XIV/Fe XIII (left) and Fe XI/Fe X (right) with electron temperature modelled using CHIANTI. Different curves are plotted for different densities. See text for other parameters used in the model.

at four density steps. Surprisingly, these calculations indicate the density dependence of the Fe XIV/Fe XIII line ratio to be significant, contradicting the results of Srivastava *et al.* (2007). The density dependence of the Fe XI/Fe X ratio is relatively weaker. Figure 3.2 also shows an opposite dependence for the two ratios on density. The curves in the left panel shift towards the higher temperature side as the density decreases whereas that in the right panel shift towards the lower temperature side. So, apart from the observed intensity ratio, the density information is additionally needed to estimate the temperature. Then, these calibration curves for the appropriate line pair, can be used to estimate temperature at any location on the loop. The necessary density values are computed using the density sensitive IR line pair as explained in the following section.

3.3.2 Temperature Variation along Loop Structures

Individual loop structures that are clearly visible in the images for both the lines of a line pair were identified. These structures were followed manually by clicking at many locations along the structure in one of the emission lines and the same pixel locations are automatically chosen from the images in other lines observed at the same time. Only those parts of the loops that are clearly discernible and seemingly

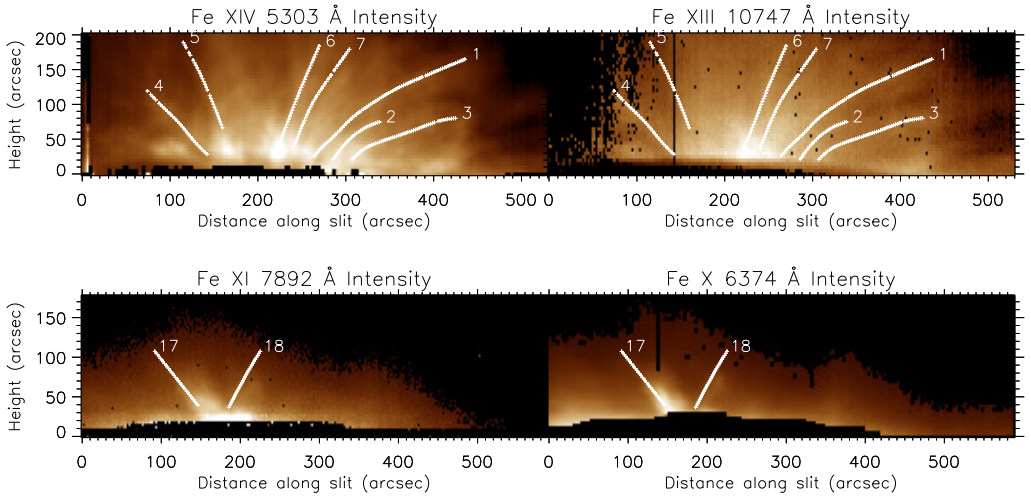

FIGURE 3.3: Spectroheliograms in Fe XIV 5303 Å and Fe XIII 10747 Å (top two panels) constructed from the scan taken on 2005 September 21 and that in Fe XI 7892 Å and Fe X 6374 Å constructed from the scan taken on 2007 October 6. Locations chosen along individual loop structures are denoted with plus symbols. Each structure is given a number, marked at the end, for reference.

isolated are chosen. A total of 18 loop segments were selected from all the scans. Figure 3.3 displays the constructed spectroheliograms for both the line pairs with the selected loop segments denoted by plus symbols. Numbers given at the end of these structures, are for reference. Intensity ratios required for the temperature estimation, were obtained along each of these structures. However, as explained in the previous section, density information for all these structures is additionally needed. The density values were derived using the simultaneously observed IR line pair Fe XIII 10747 Å & 10798 Å, whose ratio is sensitive to changes in density but a weak function of temperature (Noens *et al.* 1984). Also, this had been verified with CHIANTI and the ratio was found to be fairly constant with $\lesssim 1$ % changes over a temperature range of 1 – 4 MK. However, the signal in 10798 Å line is poor and the density information could not be obtained at all the locations along a loop. So, the log values of the observed densities were fitted linearly to get the value at each pixel location along a desired structure. Obtained electron density was found to vary between $10^{8.5}$ and $10^{8.0}$ cm^{-3} in the chosen structures. Density information could not be obtained for the scans in set II as they are observed only in Fe XI and Fe X. For the structures chosen from these scans, we model the density variation with the average gradient observed in the structures from set I and taking the density at the base to be $10^{8.5}$ cm^{-3}. This may have

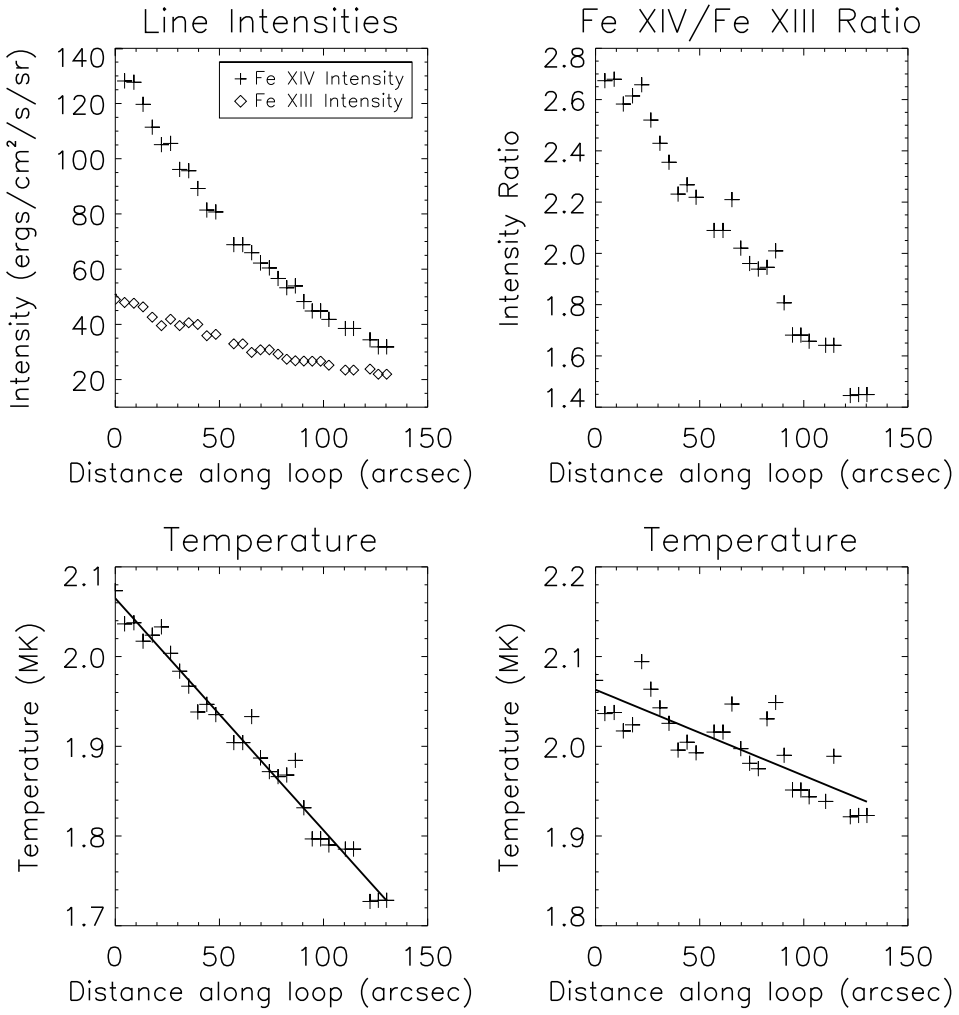

FIGURE 3.4: Variation of different parameters along loop #5 marked in Figure 3.3. Temperature values in the bottom panels are for a constant (left) and varying (right) density models. The solid lines over plotted on these values represent a linear fit.

some uncertainty, but at least allows us to take the density variation into account. Combining thus derived density information with the observed line ratios, the temperature along each loop structure is computed using the already constructed calibration curves. The temperature values are then plotted with distance from the base of the chosen segment and fitted with a first order polynomial to obtain the temperature gradients. Similar computations were also done for a constant density scenario to illustrate the effect of density variation. The observed intensities in 5303 Å and 10747 Å lines, their ratio and the temperature profiles along loop #5 (see Figure 3.3) are shown in Figure 3.4. Temperature values in the bottom left panel are derived for a constant density $10^{8.5}$ cm^{-3} and that on the bottom right

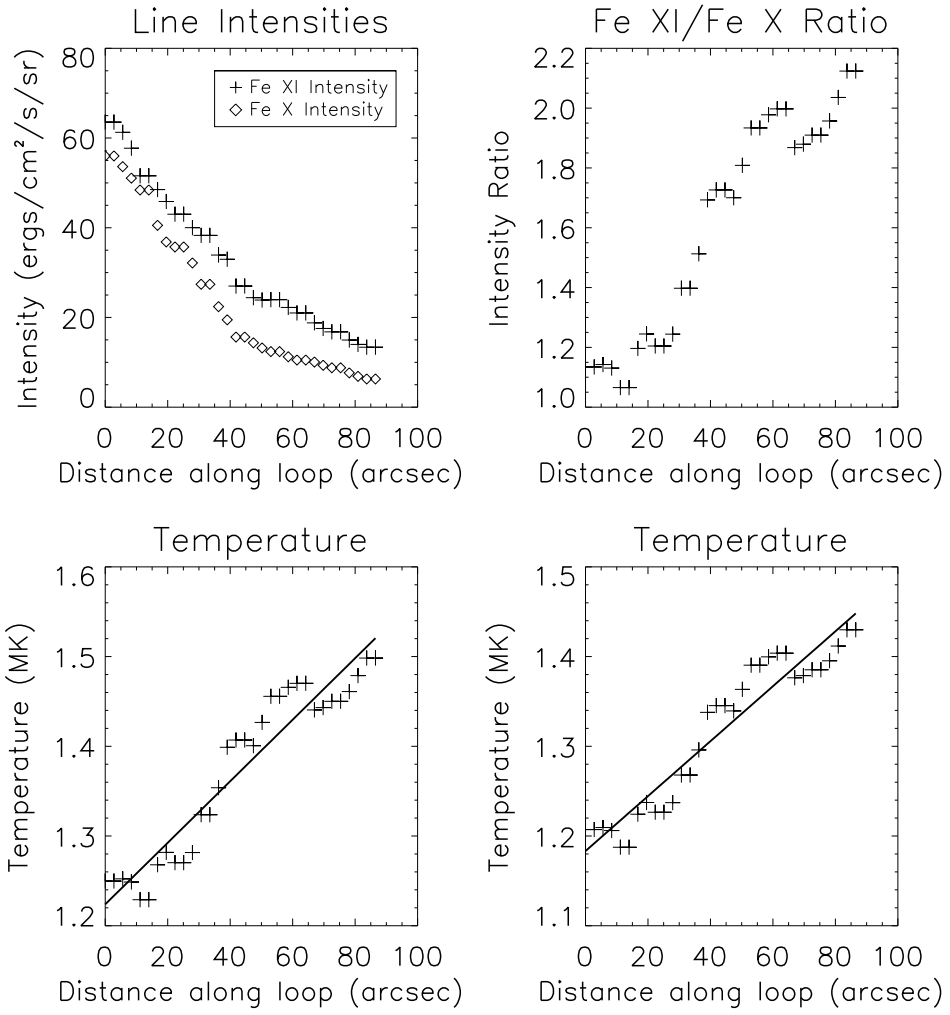

FIGURE 3.5: Observed intensities, their ratio and the temperature values obtained along loop #17 marked in Figure 3.3. Bottom panels display the temperature values derived for constant (left) and varying (right) density models. The solid lines over plotted represent a linear fit.

are derived taking the observed density variation into account. The solid lines over plotted on these values represent a linear fit to the data. Similar plots for loop #17, observed in 7892 Å and 6374 Å lines, are shown in Figure 3.5. Despite the contrasting behaviour observed in temperature for the two line pairs, the density variation made the temperature gradients flatter for both the cases. This is due to the opposite dependence of these ratios on density (see § 3.3.1). The scatter in temperature values increased when the density dependence of the line ratios is taken into account which could possibly arise due to uncertainties in the density estimation. The gradient values obtained for all the selected structures along with the actual temperature values at 10″ & 100″ distances from the base of a

TABLE 3.2: Temperature values and their gradients along individual structures.

Set	Date	loop (#)	Temperature at 10″ (MK)	Temperature at 100″ (MK)	∇T_d[1] (MK arcsec^{-1})	∇T[2] (MK arcsec^{-1})
I	2005 Sep 21	1	2.12±0.009	2.05±0.005	-0.0007±0.00007	-0.0013±0.00006
	2005 Sep 21	2	2.23±0.006	2.02±0.007	-0.0023±0.00016	-0.0022±0.00015
	2005 Sep 21	3	2.26±0.008	2.04±0.006	-0.0024±0.00012	-0.0033±0.00009
	2005 Sep 21	4	2.02±0.010	1.92±0.010	-0.0012±0.00018	-0.0021±0.00020
	2005 Sep 21	5	2.05±0.009	1.97±0.007	-0.0010±0.00014	-0.0026±0.00008
	2005 Sep 21	6	2.05±0.008	2.07±0.005	0.0003±0.00011	-0.0010±0.00009
	2005 Sep 21	7	2.06±0.008	2.03±0.005	-0.0003±0.00010	-0.0011±0.00007
	2005 Oct 3	8	2.00±0.014	1.93±0.009	-0.0008±0.00018	-0.0010±0.00014
	2005 Oct 3	9	2.17±0.013	2.18±0.008	0.0001±0.00015	-0.0007±0.00012
	2005 Oct 3	10	1.93±0.012	1.95±0.014	0.0002±0.00025	-0.0020±0.00020
	2005 Oct 3	11	2.30±0.020	2.29±0.014	-0.0001±0.00028	-0.0007±0.00024
	2005 Oct 6	12	2.17±0.007	1.95±0.009	-0.0025±0.00019	-0.0015±0.00017
	2005 Oct 6	13	1.99±0.011	1.97±0.011	-0.0003±0.00021	-0.0023±0.00016
	2005 Oct 6	14	1.99±0.010	1.79±0.010	-0.0022±0.00017	-0.0013±0.00018
	2005 Oct 6	15	1.96±0.010	1.92±0.011	-0.0005±0.00020	-0.0014±0.00014
	2005 Oct 6	16	1.97±0.012	1.89±0.013	-0.0009±0.00022	-0.0015±0.00016
II	2007 Oct 6	17	1.21±0.011	1.49±0.017	0.0031±0.00022	0.0034±0.00020
	2007 Oct 6	18	1.40±0.012	1.46±0.017	0.0006±0.00022	0.0008±0.00022

[1] Temperature gradients taking the density dependence of the line ratio into account.
[2] Temperature gradients for a constant density ($10^{8.5}$ cm^{-3}).

chosen structure are tabulated in Table 3.2. The values listed in the last column are temperature gradients obtained assuming the density to be constant at $10^{8.5}$ cm^{-3}. The 1-σ uncertainties in each of these parameters, computed from the fit, are also given in the table.

3.4 Results and Discussion

The temperature profiles had been constructed for 18 individual loop structures using emission line ratios. Out of these 16 are from the scans in set I and the rest two are from those in set II. Table 3.2 lists the computed temperature values at 10″ & 100″ distances along with the temperature gradient for each of these structures. The gradient values represent a significant change in temperature along the loop length (see Figures 3.4 & 3.5). Also, none of the structures was observed from the foot point through the full length of a loop, so the temperature difference between the foot point and apex of the loop can be even larger. Clearly, the gradients are negative for most of the loops (positive but close to zero for the rest)

under set I and positive for those under set II. The average gradient values are -0.0009±0.00004 MK arcsec^{-1} and 0.0018±0.00016 MK arcsec^{-1} respectively, for these two cases after accounting for the density variation along the loops. Note that the temperature estimation in the former case is from [Fe XIV] 5303 Å/[Fe XIII] 10747 Å ratio whereas that in the latter case from [Fe XI] 7892 Å/[Fe X] 6374 Å ratio. The data sample in set II is limited (only two loops #17 & #18) due to the non-availability of many off-limb loops with good signal during the observation time which is close to the solar minimum. However, it complements the extensive analysis done by Singh *et al.* (2004), who finds an increase in 7892/6374 line intensity ratio along 90 % of the structures studied, implying a positive temperature gradient. Therefore, the observed variations in temperature from [Fe XIV]/[Fe XIII] and [Fe XI]/[Fe X], is possibly a general behaviour. The line pair (Fe XIV, Fe XIII) represents a slightly hotter plasma compared to the (Fe XI, Fe X) pair. So, it appears that the loop tops are, in general, colder when observed in hotter lines and hotter in relatively colder lines, with respect to their coronal foot points. Further, the average temperature values from both the sets are closer to each other at larger heights (100″) indicating the likelihood to reach a common value at greater heights (Singh *et al.* 2006b).

As mentioned earlier, theoretical calculations suggest that the temperature in a uniformly heated stable hydrostatic loop increases along its length and peaks at the loop top (Rosner *et al.* 1978; Priest *et al.* 1998). Also, if the heating is non-uniform with a bulk of the heat deposited close to the foot points, then the temperature maximum can occur well below the loop top leading to a negative temperature gradient along its length (Antiochos *et al.* 1999; Aschwanden *et al.* 2001). But in such cases, if the heating scale height is smaller than one-third of the loop half-length, loops become thermally unstable and are short lived (Serio *et al.* 1981). Recently, Huang *et al.* (2012) report the ubiquitous presence of such loops in the low latitude quiet corona. However, taking the generality of our results into account, it is not possible to explain the contrasting trends observed in different temperature plasma with different types of heating. Alternatively, if the loop structures studied here are composed of several unresolved strands that are impulsively heated resulting in a multi-thermal structure and if we allow the hotter and colder plasma to interact with each other gradually, the observed temperature decrease in hotter plasma and increase in colder plasma can be easily

explained. Since the loops are observed here at a moderate spatial resolution ($\approx 2''$ per pixel), it is possible that they are multi-stranded (Reale and Peres 2000) and multi-thermal (Patsourakos and Klimchuk 2007). At this point, the exact mechanism causing the gradual interaction between the hotter and colder plasma remains unclear. But this process seems to hold the key to constrain loop heating models and needs further investigation.

Chapter 4

Variation of Emission Line Width with Altitude and Latitude

Spectral line profiles contain important information of the emission source. For an optically thin emission line from corona, the line broadening is mainly due to thermal and non-thermal sources. Any observed increase in line width with height is often attributed to the presence of outwardly propagating Alfvén waves in the corona while a decrease in it is interpreted in terms of dissipation of these waves. It is also argued that an increase in ion temperature due to preferential heating can also cause line broadening. A few other studies found the average line widths in polar regions to be larger than that in equatorial regions which was again linked to the presence of some non-thermal source powering the fast solar wind. Although the exact reason is not clear, their relation to coronal heating and fast wind acceleration makes the line width variation studies important. Spectroscopic studies of the equatorial off-limb corona, using the high spatial and spectral resolution data obtained with the Norikura coronagraph indicated that the variation of line width with height is different for different temperature lines. The line width of the forbidden red emission line [Fe X] 6374 Å was found to increase with height and that of the green emission line [Fe XIV] 5303 Å decrease with height. A gradual interaction between different temperature plasmas is proposed to explain this. To

investigate the behaviour of these lines in other parts of corona, further observations were made covering the mid-latitude and polar regions which allowed us to make a latitudinal comparison as well. Similar behaviour of green and red lines was found in the mid and polar regions indicating this nature to be global. Latitudinal comparison revealed an increase in line width of the red and other emission lines except the green line. The details of these investigations[1] are presented in this chapter.

4.1 Introduction

The solar corona consists of very hot, tenuous plasma, and the processes responsible for its multi-million kelvin temperature still remains unexplained. Spectroscopic observations are necessary to improve our understanding as the three line parameters peak radiance, Doppler shift, and line width, provide vital information about the physical and dynamical properties of the source. Line profiles contain both thermal and non-thermal information of the source. For an optically thin emission line from corona, the Full Width at Half Maximum[2] (FWHM) can be given as

$$\mathrm{FWHM} = 2\sqrt{\ln 2}\,\frac{\lambda}{c}\left(\frac{2\,kT_{\mathrm{ion}}}{\mathrm{M}} + V_{nt}^2\right)^{\frac{1}{2}} \tag{4.1}$$

where λ is the wavelength of the line, T_{ion} is the temperature of the emitting ion, V_{nt} is the non-thermal velocity, k is the Boltzman constant, M is mass of the ion and c is velocity of light. Any changes, thermal or non-thermal will therefore result in change of line width. Hassler *et al.* (1990) studied the line profiles of some EUV lines using a rocket experiment and observed an increased broadening with height above the limb. Coronal hole Fe X spectra taken at the National Solar Observatory showed an increase in the line width with height (Hassler and Moran 1994). SOHO/SUMER (Wilhelm *et al.* 1995) was used to record the off-limb, height-resolved spectra of a Si VIII density-sensitive line pair, in equatorial coronal regions (Doyle *et al.* 1998) and in polar coronal holes (Banerjee *et al.* 1998) which indicate an increase in non-thermal velocity with height. A similar analysis by

[1] Results of this work are published in Prasad *et al.* (2013)

[2] Corrected for the instrumental width

Wilhelm *et al.* (2004), in several other spectral lines, also showed an increase in Doppler width with height. Observations by Erdelyi *et al.* (1998) suggest a centre-to-limb variation in the broadening of upper chromospheric and transition region lines. Using the EIS spectrometer on *Hinode*, Banerjee *et al.* (2009a) reported that for the polar region, the line width data show that the non-thermal line-of-sight velocity increases from 26 km s^{-1} at 10″ above the limb to 42 km s^{-1} at some 150″ (*i.e.* ≈110 000 km) above the limb. The measured variation in line width with height supports undamped wave propagation in coronal structures. This was a strong evidence of outwardly propagating, undamped Alfvén waves in the corona, which may contribute to coronal heating and the high-speed solar wind in the case of coronal holes. But, Seely *et al.* (1997), based on SUMER observations, suggested that the increase in line width could be due to an increase in ion temperature which significantly deviates from ionization equilibrium temperature, due to preferential heating.

Singh *et al.* (1999, 2002b, 2003a) using extensive data obtained with the 25 cm Norikura coronagraph, found that the FWHM of [Fe X] 6374 Å (red emission line) increases with height whereas that of the [Fe XIV] 5303 Å (green emission line) decreases with height in the same region. Since, the damped/undamped waves cannot cause different changes in line widths of different lines, they suggested that this behaviour can be explained by gradual mixing of different temperature plasma with height above the limb. By including the IR lines [Fe XIII] 10747 Å and 10798 Å in their study, Singh *et al.* (2003a) found that the FWHM of spectral lines with ionization temperatures less than 1.6 MK increase and more than 1.6 MK decrease with height. Singh *et al.* (2004) observed similar complex variations in radiance ratios of different lines, with respect to red line. The green line to red line radiance ratio decreases with height above the limb, whereas the IR to red and [Fe XI] 7892 Å to red ratios increase with height. They proposed that such a behaviour in the radiance ratios of emission lines can also be explained if we consider the gradual interaction between relatively cold and hot plasma. As a further confirmation, Singh *et al.* (2006a) found that the FWHM of the red and green lines does not vary after heights greater than ≈250″ above the limb. This is expected in the case of gradual mixing of multi-thermal plasma with increasing altitude, as the plasma reaches a uniform temperature and non-thermal velocity after a certain height.

Recently, Raju *et al.* (2011) reported an increase in the line width of the green line with height, up to about 400″ above the limb, from the line profiles obtained during the total solar eclipse of 21 June 2001 using a Fabry−Perot [FP] etalon. Singh *et al.* (2011) also observed a case where the green-line width increases with height and showed that the FWHM of emission lines is different for different coronal features. By analysing over 130 coronal structures Singh *et al.* (2003a) observed that 89 % of the structures show a negative gradient in the green emission line and 95 % of those show a positive gradient in the red emission line. It may be just a coincidence that different structures with different physical and dynamical characteristics showed such a result reported by Raju *et al.* (2011). Also, the results by Singh *et al.* are based on a large data base spread over many years whereas those of Raju *et al.* are based on observations during an eclipse of short duration. It may also be noted that the instrumental line width in their case is 0.2 Å and the uncertainty in the line width determination is 0.03 Å compared to the values < 0.1 Å and 0.002 Å respectively, in the spectroscopic measurements made by Singh *et al.* (2002a). In addition, the observed line profiles of emission with FP are asymmetric as compared to those with the spectrograph, because of the varying dispersion in FP interference fringes.

Since, the observational results of Singh *et al.* are based on extensive analysis using a large dataset, it can be assumed as the general variation. However, the analysed coronal regions are mostly restricted to equatorial regions and it is necessary to check if the behaviour is same in the high latitude regions. Observations with the same coronagraph were made to perform this.

4.2 Observations

Raster scans of the off-limb polar corona were taken using the 25 cm coronagraph at Norikura, Japan, on several days in September and October, 2004. Most of the scans were taken simultaneously in two iron emission lines using two CCD cameras, with one line being [Fe X] 6374 Å (red line) and the other being [Fe XI] 7892 Å or [Fe XIII] 10747 Å or [Fe XIV] 5303 Å (green line). A few scans were taken in the

TABLE 4.1: Date of observations, emission lines, pixel scale, and dispersion. Observations in a single line are blank under Line2.

Date	Emission line		Pixel scale	Dispersion (mÅ pixel^{-1})	
	Line1	Line2	(″)	Line1	Line2
12 Sep. 2004	6374 Å	7892 Å	4.2	47.1	47.3
15 Sep. 2004	6374 Å	7892 Å	4.2	47.1	47.2
16 Sep. 2004	6374 Å	7892 Å	4.0	47.1	47.2
14 Oct. 2004	6374 Å	10747 Å	4.6	57.2	122.5
	5303 Å	....	4.0	46.9	....
	5303 Å	....	4.0	46.9	....
16 Oct. 2004	6374 Å	10747 Å	4.7	57.2	122.5
	6374 Å	10747 Å	4.7	57.2	122.5
17 Oct. 2004	5303 Å	....	4.0	39.8	....
	5303 Å	....	4.0	39.8	....
	5303 Å	....	4.0	39.8	....
21 Oct. 2004	6374 Å	5303 Å	4.7	57.2	31.5
25 Oct. 2004	6374 Å	10747 Å	4.7	57.2	122.0
	6374 Å	10747 Å	4.7	57.2	122.1
27 Oct. 2004	6374 Å	10747 Å	4.7	57.2	123.0
	6374 Å	10747 Å	4.7	57.2	123.0
	6374 Å	10747 Å	4.7	57.2	123.0
	5303 Å	....	5.0	39.9	....

green line alone when the second camera did not work. Details on the instrumental setup can be found in Singh *et al.* (1999, 2003b, 2003a). The length of the slit is around 500″ and the width is 4″ for most of the scans and 5″ for the rest. Each scan covers around 100″ of the solar corona above the limb. The exposure times were varied from scan to scan and day to day, over a broad range from 50 to 180 seconds for each spectrum, according to the target of observation to get a good signal. The dark, flat, and disk spectra were taken immediately after each set of observations. Although the main target was to scan the polar corona, due to some miscalculation during the setup, the centre of the slit was kept around 65° solar latitude which means our scans cover the region roughly from 46° to 84° solar latitude. This allowed us to study the line-width behaviour in the mid- and the high-latitude regions separately and compare them with the earlier equatorial region results. The pixel scale, dispersion, and the emission lines observed on each date are listed in Table 4.1.

4.3 Data Analysis

Following the standard procedure[3], each spectral image was corrected for the dark current, and pixel to pixel sensitivity changes using flat field and the scattered light component due to sky brightness using disk spectra. The subtraction of sky brightness, including the scattered disk light due to the instrument, yields clean emission line spectra free of absorption lines in most of the cases. The spectra obtained on some days when the exposure time was kept short due to sky conditions, were binned, both in spatial and spectral dimensions, to improve the signal-to-noise ratio. The dispersion values have been computed for each spectra and on each day of observation, using the solar-disk spectra obtained immediately after the scan and the standard solar spectra. Then the spectra is fitted with a simple Gaussian profile to obtain the parameters such as peak radiance (counts), Doppler velocity, and line width (FWHM) at each location in the solar corona. Figure 4.1 shows the typical line profiles in all four emission lines at two different heights (10″ and 60″) above the limb. The overplotted solid lines (in green) are the fitted Gaussian profiles. It may be noted that the green and 7892 Å emission lines have a dip (second and fourth rows from top in Figure 4.1) over the emission profile due to a photospheric absorption line at locations where the signal is lower. The pixel locations with this dip were carefully discarded while fitting the Gaussian profiles although the subtraction of the scattered light component from the spectrum has removed this absorption line feature in most of the spectra. The derived FWHM values from the Gaussian fit were then corrected for the instrumental effect using the relation, $\mathrm{FWHM_{line}}=(\mathrm{FWHM^2_{obs}}-\mathrm{FWHM^2_{ins}})^{\frac{1}{2}}$, where $\mathrm{FWHM_{line}}$ is the true width of the emission line, $\mathrm{FWHM_{obs}}$ is the observed value, and $\mathrm{FWHM_{ins}}$ is the instrumental contribution calculated from the disk spectra. FWHM values after this correction and the corresponding uncertainties are listed in the respective panels of Figure 4.1. The scans taken in two lines simultaneously have different image scales due to different focal lengths of the camera optics used. These are brought to same spatial scale using a reference slit image on the two CCD cameras taken with wires across the slit separated by a known fixed distance. The final spatial scales and the dispersion values for each scan used in this analysis are listed in Table 4.1.

[3]Refer to Section 2.2.3 for the standard reduction procedure

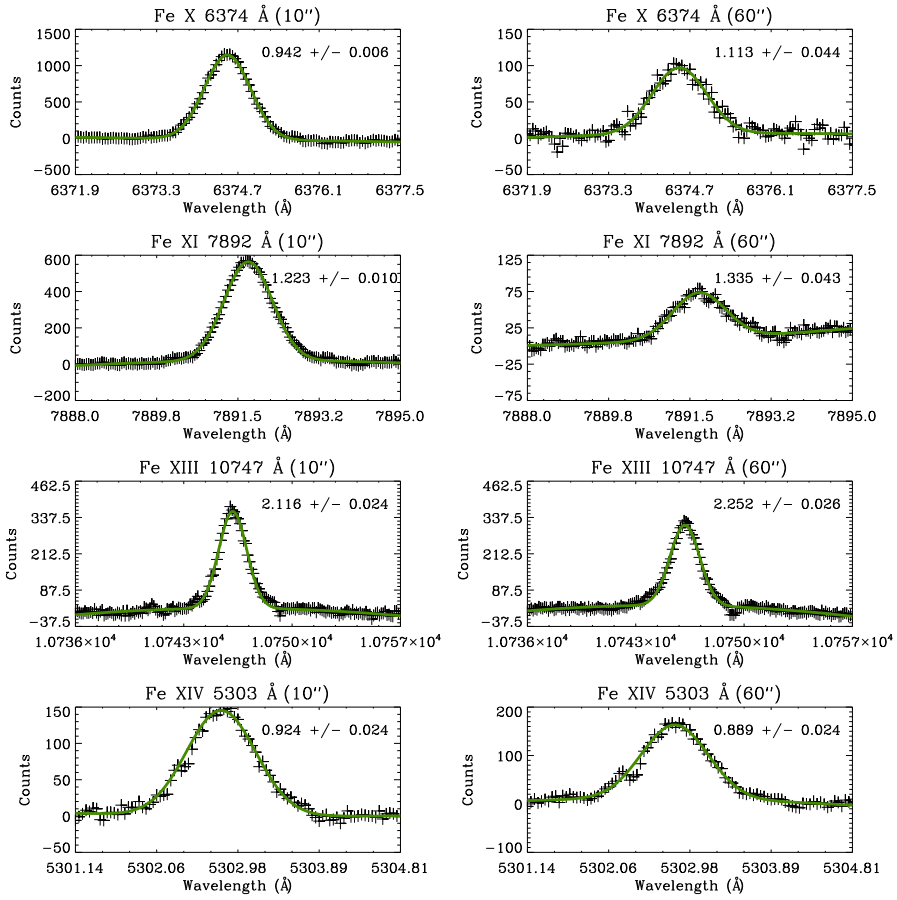

FIGURE 4.1: Line profiles of all four emission lines at two different heights 10″ (left) and 60″ (right) off-limb. The overplotted green solid lines are the fitted Gaussian profiles. Values inside each plot are the FWHM values and the corresponding uncertainties. An absorption line over the emission profile of green line (bottom row) is visible, which is discarded while fitting the profile.

Radiance and line-width maps were then constructed for each scan. A typical set of radiance maps taken simultaneously in two lines, the red line and one of the other three emission lines, can be seen in Figure 4.2. The radiance maps in this figure show that the coronal structures (loops) in the red and 7892 Å emission lines are well defined, whereas those in the green and 10747 Å lines are diffuse. EUV observations also show similar fuzziness in the coronal structures in hotter lines (Tripathi *et al.* 2009). Also some portion of the coronal region can be seen to be dimmer, particularly in the higher-temperature emission lines. These regions correspond to the high-latitude portions of the scan.

Now to study the variation of line width with height above the limb, scatter plots can be constructed from these maps. But at a few locations, especially at

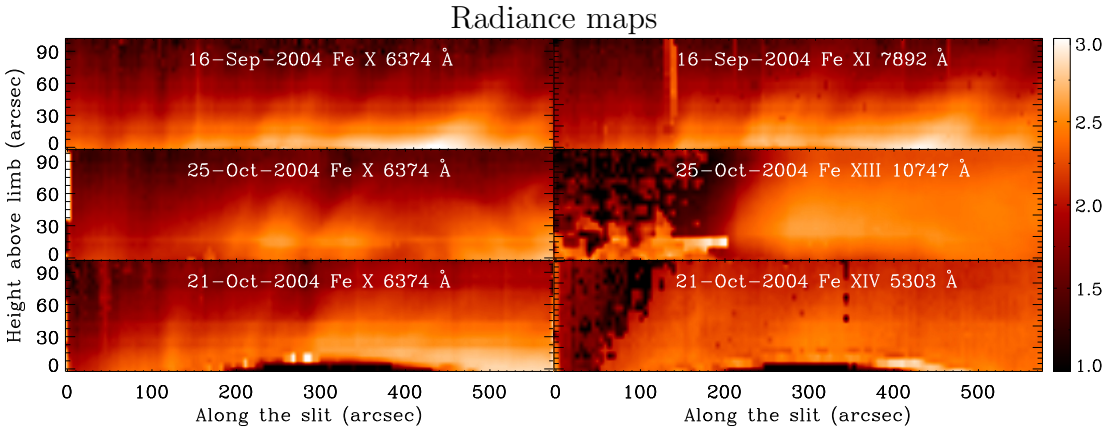

FIGURE 4.2: Radiance maps (log-scaled) constructed from the raster scans taken on different dates. In each row, the left side show a radiance map of coronal region (about 500″ × 100″), in the red emission line and the right side show corresponding region in one of the other three emission lines observed simultaneously. Respective dates and the spectral lines are written on each image.

TABLE 4.2: FWHM limits chosen to exclude locations with unreliable data

Emission line [wavelength]	T_m [1] (MK)	FWHM (Å)	
		Lower limit	Upper limit
Fe X 6374 Å	1.0	0.6	1.4
Fe XI 7892 Å	1.2	0.8	1.8
Fe XIII 10747 Å	1.6	1.3	2.5
Fe XIV 5303 Å	1.8	0.6	1.3

[1] Temperature of maximum abundance

larger heights, due to low signal-to-noise ratio, the spectra were not fitted properly leading to either very low or high FWHM values. To exclude such data locations, we restrict our analysis to the regions with FWHM values between the limits listed in Table 4.2. Lower limits are calculated from the peak temperature values with zero non-thermal component and the upper limits are calculated by adding 1 MK to the peak temperature along with 30 km s^{-1} non-thermal component (maximum reported value for these lines). However small, there will always be some non-thermal component which makes our lower limits cover the temperature regime below the peak values.

Having set the upper and lower limits for the FWHM in each emission line, we make binary images from the FWHM maps and compare them with the respective radiance maps to confirm our criterion. Binary images are constructed with 0

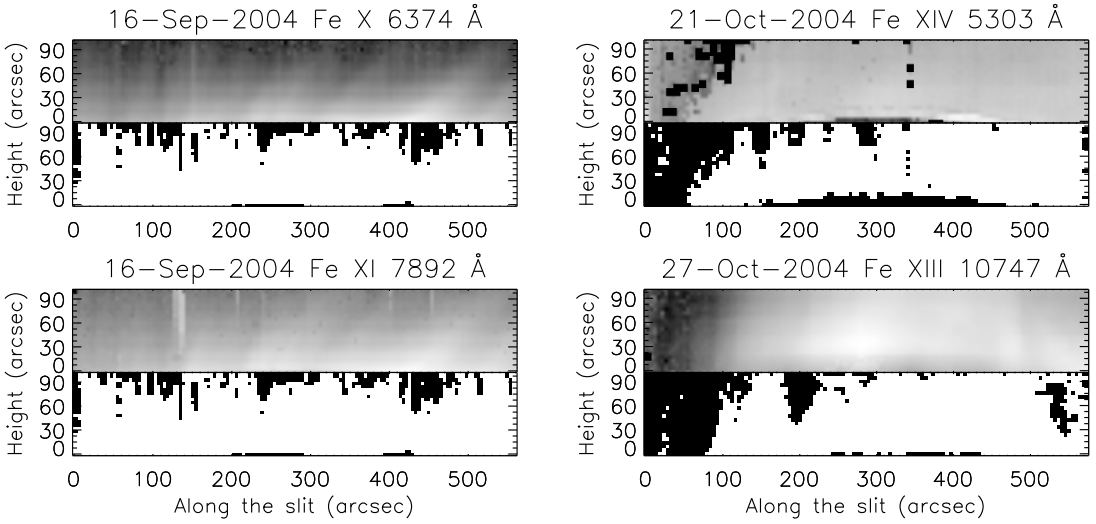

FIGURE 4.3: Radiance maps and the corresponding binary images in all four emission lines Fe X 6374 Å, Fe XI 7892 Å, Fe XIII 10747 Å, and Fe XIV 5303 Å. Radiance is displayed in the top half with the corresponding binary image in the bottom half. Dark pixel locations are the discarded locations with FWHM values outside the limits.

(dark) for locations with FWHM values outside the limits and 1 (bright) for those within limits, which are chosen for our analysis. Figure 4.3 displays such binary images along with the corresponding radiance maps in all four emission lines. In each plot, the top half displays the radiance image and the bottom half displays the corresponding binary image. Any location with FWHM values outside the limits, in either line in the simultaneously observed pair, is discarded. The figure shows that using this criterion we exclude only a minor part of the observed coronal region from our study. The visual comparison of the radiance maps with the binary images indicates that the discarded locations with very low and high FWHM values coincides with the locations of very low radiance signal. At these locations the Gaussian fits to the observed profiles are not reliable and hence their omission in the scatter plot and our choice of limits are justified. Moreover, our aim is to study the general variation of line width with height above the limb and any real events causing abnormally high/low line-width values should be avoided from causing contamination in our general results.

4.4 Results

In the previous investigation over the equatorial region, Singh *et al.* (2006b) studied the variation in FWHM with height by choosing the locations on the loops separately and then over the diffused coronal region around loops but discarding the unreliable data of low radiance. They found that the results from the loop data, diffused plasma and the scatter plots taking the whole scan region are similar. In the current dataset, loop structures are clearly visible only in a few scans and also the simultaneous observations with green line as one of the pair are limited. Therefore, it was decided to investigate the variation of FWHM with height in each line individually, using the scatter plots.

4.4.1 FWHM Variation from the Full Scan Region

Taking the full scan region from each observation, scatter plots of FWHM were made with height above the limb, in all four emission lines. Figure 4.4 shows one such plot for each of the four emission lines observed. These plots correspond to the set of scans shown in Figure 4.3. It can be seen that the points at individual heights are scattered over a range of FWHM values. This vertical scatter is mainly due to the varying physical characteristics of the different coronal structures lying along the slit.

Now to determine gradients, the mean values at each height are computed and fitted linearly. Although most of the points at individual heights fall close to one another, there are some occasional outliers particularly from parts of the scan nearer and farther from the limb, which could be from the low-signal regions that crept in, despite setting the limits. To avoid this, we compute the standard deviation at each height and use them as weights in computing the linear-fit parameters. The larger is the standard deviation, the smaller is the weight given to that value. In this way, the linear fit represents most of the points and allows us to assess the general behaviour of the observed coronal region. Figure 4.5 displays the mean values and their linear fits for the plots corresponding to those in Figure 4.4. The

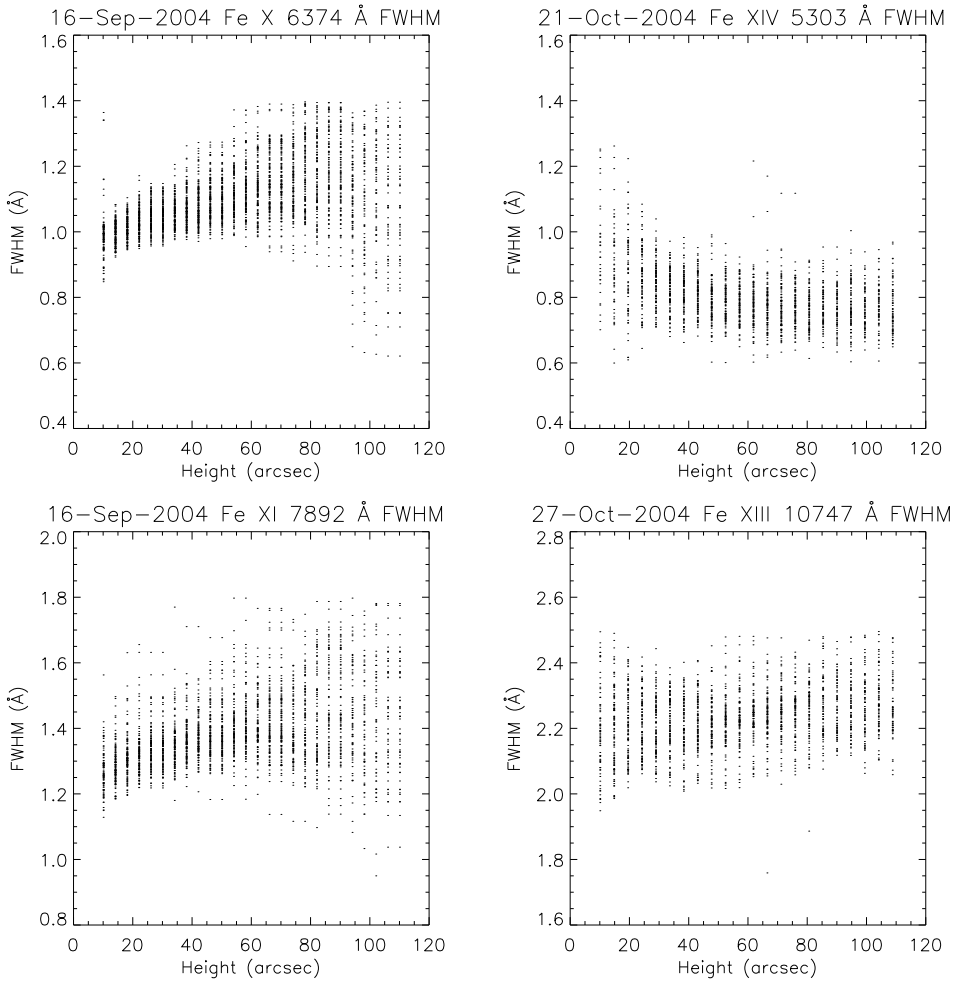

FIGURE 4.4: FWHM variation over the full scan region observed, in the emission lines Fe X 6374 Å, Fe XI 7892 Å, Fe XIII 10747 Å, and Fe XIV 5303 Å. It appears that the vertical scatter at each height is due to varying physical properties of different structures along the slit as the uncertainty in determination of FWHM is much less ($\approx$ 10 mÅ) compared to the observed variations with height.

mean values at each height are represented by circles, bars denote the corresponding standard deviations, and the solid line is the linear fit. Y-axes of all the plots are scaled to the same length for better visual comparison. These plots clearly show that the variation of FWHM is different for different-temperature lines.

The values of FWHM at 10″, 60″ and the gradients obtained from the linear fits, are tabulated for all of the lines over the full scan covering the latitude region 46° to 84°, in Table 4.3. Mean values of FWHM [μ], for all the observations made on different days and the standard deviation [σ] are computed and listed in a row at the end of the values for each spectral line in the table. Below the

TABLE 4.3: FWHM mean values and their gradients over the full scans (46° to 84° latitude) for different days at 10″ and 60″ heights above limb, for different emission lines. Average values of all the scans and those at equatorial regions from earlier results are also listed for comparison.

Emission line (line centre)	Date	FWHM [Å]		Gradient [mÅ arcsec^{-1}]
		10″	60″	
6374 Å	27 Oct. 2004	1.07	1.11	0.90
	25 Oct. 2004	1.01	1.07	1.21
	27 Oct. 2004	1.07	1.11	0.77
	14 Oct. 2004	1.06	1.10	0.71
	27 Oct. 2004	0.97	1.01	0.85
	16 Sep. 2004	0.98	1.13	2.89
	21 Oct. 2004	1.02	1.09	1.43
	15 Sep. 2004	1.06	1.07	0.23
	16 Sep. 2004	1.00	1.12	2.33
	25 Oct. 2004	1.00	1.04	0.74
Mean ($\mu \pm \sigma$)		1.02±0.04	1.08±0.04	1.21±0.77
Equatorial regions[1]		0.80±0.05	0.86±0.06	1.05
7892 Å	16 Sep. 2004	1.20	1.42	4.35
	15 Sep. 2004	1.25	1.27	0.23
	16 Sep. 2004	1.31	1.40	1.91
Mean ($\mu \pm \sigma$)		1.25±0.04	1.36±0.07	2.16±1.69
Equatorial regions[1]		1.08±0.09	1.10±0.10	0.57
10747 Å	27 Oct. 2004	2.23	2.27	0.82
	25 Oct. 2004	2.22	2.22	0.18
	27 Oct. 2004	2.19	2.24	0.90
	14 Oct. 2004	2.11	2.12	0.13
	27 Oct. 2004	2.13	2.12	-0.11
	25 Oct. 2004	2.13	2.18	1.00
Mean ($\mu \pm \sigma$)		2.17±0.05	2.19±0.06	0.49±0.43
Equatorial regions[1]		1.86±0.10	1.88±0.14	0.22
5303 Å	14 Oct. 2004	0.82	0.79	-0.45
	14 Oct. 2004	0.81	0.78	-0.54
	27 Oct. 2004	0.81	0.81	0.05
	27 Oct. 2004	0.77	0.73	-0.84
	17 Oct. 2004	0.81	0.81	0.12
	17 Oct. 2004	0.88	0.87	-0.24
	17 Oct. 2004	0.87	0.86	-0.21
	21 Oct. 2004	0.85	0.80	-1.06
Mean ($\mu \pm \sigma$)		0.83±0.03	0.81±0.04	-0.40±0.38
Equatorial regions[1]		0.85±0.05	0.82±0.06	-0.66

[1] Corresponding values at equatorial regions computed from the values in Table III of Singh *et al.* (2003b). For 10747 Å values from Table I of Singh *et al.* (2003a) are used.

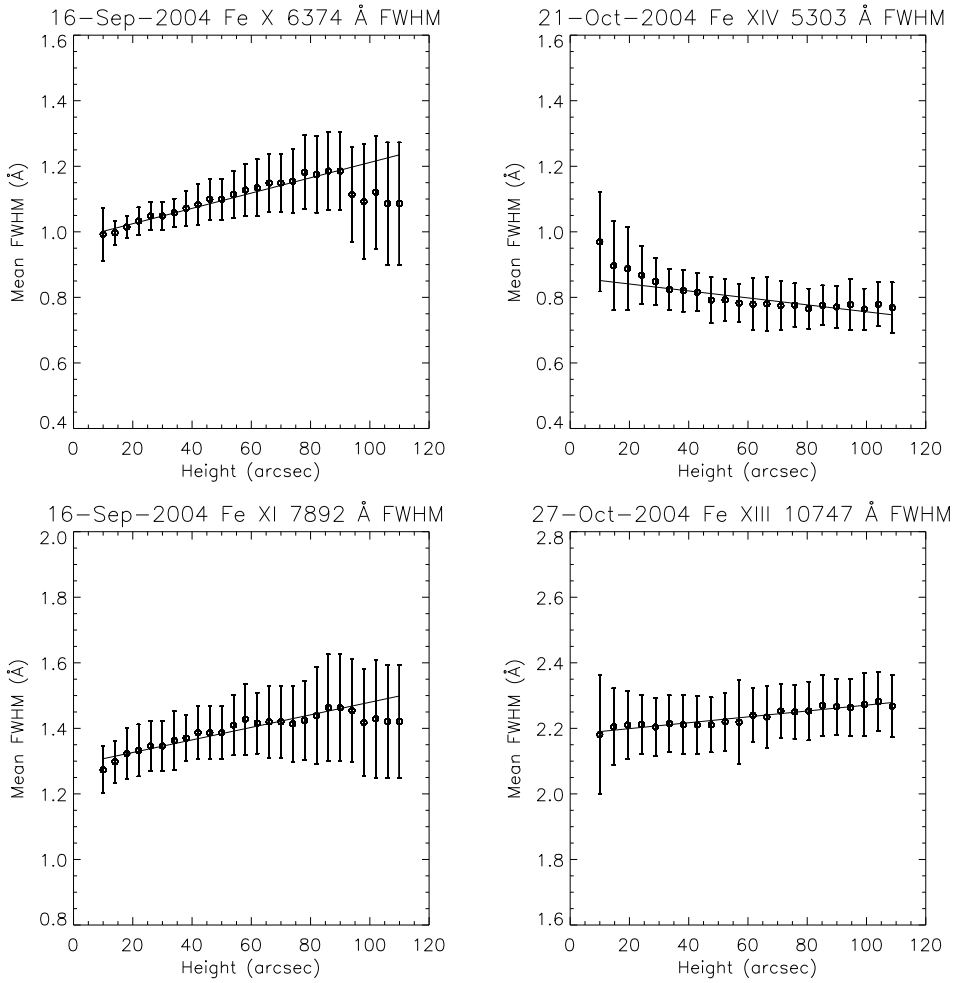

FIGURE 4.5: Mean FWHM variation with height, over the full scan region observed in the emission lines Fe X 6374 Å, Fe XI 7892 Å, Fe XIII 10747 Å, and Fe XIV 5303 Å. Circles represent the mean values at individual heights and the bars denote the respective standard deviations. The solid line is the weighted linear fit to the mean values using the inverse of standard deviation as weights in fitting.

mean values, corresponding values for equatorial regions, taken from the earlier work by Singh *et al.* (2003b, 2003a), are also listed for comparison. The authors listed the FWHM values for the heights 50″ and 100″ above the limb and their gradients. We computed the values for heights 10″ and 60″ above the limb using the corresponding gradients, for direct comparison. The σ-values in gradients at equatorial regions are not listed in the table as these values are not given in the respective references. It is very important to note that the σ-values here do not represent uncertainties in determining FWHM values but indicate the dispersion in the mean values of FWHM and gradients, which arise due to different physical

characteristics of different coronal structures observed on different days.

Variation in FWHM of the [Fe X] Emission Line:

The values of FWHM and the gradients (Table 4.3) indicate that the FWHM of the red line increases with height. All of the scans show a positive gradient, although the actual values vary over a broad range which might be due to different temperature or magnetic topology associated with different coronal structures. The average FWHM for these regions covering latitudes 46° to 84°, is 1.02 ± 0.04 Å at the height of 10″ as compared to 0.80 ± 0.05 Å for equatorial regions. The relative increase of this value compared with that of equatorial regions is 30 %. The average gradient also seems to show a relative enhancement of about 15 %.

Variation in FWHM of the [Fe XI] and [Fe XIII] Emission Lines:

The average FWHM values in 7892 Å and 10747 Å lines are 1.25 ± 0.04 Å and 2.17 ± 0.05 Å respectively, compared to 1.08 ± 0.09 Å and 1.86 ± 0.1 Å for the equatorial regions at 10″ above the limb. These values indicate a relative increase of about 20 % in the FWHM for this region over those for equatorial regions. The gradient values in the 10747 Å line are mostly low and positive with negative value in one of the scans. The mean gradient value for 7892 Å line seems to have changed drastically from that for equatorial regions, but the smaller data sample limits us from further analysis.

Variation in FWHM of the [Fe XIV] Emission Line:

The green emission line shows mostly negative gradients along with a couple of positive, but close to zero values, in this latitude region. The average FWHM of this line at 10″ height above the limb is 0.83 ± 0.03 Å compared to 0.85 ± 0.05 Å for equatorial regions. The values of mean gradients are -0.40 ± 0.38 mÅ arcsec^{-1}

compared to -0.66 mÅ arcsec^{-1} for equatorial regions. It is surprising that the FWHM of the green emission line in this region is almost the same as that for equatorial region, whereas the other three emission lines show an increase in these values. It may be noted that the FWHM of the green line still decreases with height, although the gradient is less steep than in equatorial regions.

4.4.2 FWHM Variation in Mid- and High-Latitude Regions

Each of our scans covers a broad region from 46° to 84° latitude. The results presented so far are from this full scan region over which the physical conditions can be different. So, we divided each scan into two parts one representing the mid-latitude region and the other high-latitude/polar region, by careful inspection of radiance profiles along the slit at different heights and comparing the structures with closest in epoch EIT images. This allows us to study the FWHM variations in the polar and mid-latitude regions separately and compare them. In some of the scans, particularly in polar regions, the signal is low and the reliable locations are poorly distributed. These are not suitable for the height-variation study and hence discarded. Mean FWHM values are then plotted for both mid- and high-latitude parts, and linear-fit coefficients are calculated as done before. These results are tabulated in Table 4.4, which indicates systematic variations in FWHM with height above the limb and also with solar latitude. FWHM values at 10″ and 60″ above the limb and the respective gradients both for mid- and high-latitude regions are listed in this table. Values corresponding to the discarded parts of the scans are left blank. Mean and σ values for all of the scans, along with the values from equatorial regions, are also listed for individual lines. It can be seen that the average FWHM values in polar regions are higher than that in equatorial regions, in all of the emission lines except green line.

We find a systematic change in FWHM values from equatorial to mid-latitude to high-latitude regions and it is different for different lines. To compare different lines, we plot the average FWHM values for all of the observed emission lines at

TABLE 4.4: FWHM values at 10″ and 60″ and their slopes for different lines in mid- and high-latitude regions. Values at equatorial regions from earlier results are also listed.

Emission line (line centre)	Date	FWHM [Å] 10″ Mid-lat.	10″ High-lat.	60″ Mid-lat.	60″ High-lat.	Gradient [mÅ arcsec^{-1}] Mid-lat.	Gradient [mÅ arcsec^{-1}] High-lat.
6374 Å	27 Oct. 2004	1.04	1.09	1.08	1.17	0.71	1.66
	25 Oct. 2004	1.00	–	1.05	–	1.11	–
	27 Oct. 2004	1.05	1.09	1.09	1.16	0.73	1.28
	12 Sep. 2004	0.99	–	1.06	–	1.49	–
	14 Oct. 2004	1.05	–	1.08	–	0.49	–
	27 Oct. 2004	0.96	–	1.01	–	0.83	–
	21 Oct. 2004	0.94	1.12	1.05	1.14	2.26	0.49
	15 Sep. 2004	1.06	0.96	1.02	1.12	-0.81	3.13
	16 Sep. 2004	1.00	1.00	1.14	1.10	2.68	1.93
	25 Oct. 2004	1.01	–	1.03	–	0.44	–
Mean (μ)		1.01	1.05	1.06	1.14	0.99	1.70
$\pm\sigma$		±0.04	±0.06	±0.04	±0.03	±0.93	±0.86
Equatorial regions[1]		0.80±0.05		0.86±0.06		1.05	
7892 Å	12 Sep. 2004	1.22	–	1.27	–	0.97	–
	15 Sep. 2004	1.25	1.15	1.25	1.26	-0.04	2.20
	16 Sep. 2004	1.28	1.34	1.40	1.40	2.50	1.28
Mean (μ)		1.25	1.25	1.31	1.33	1.14	1.74
$\pm\sigma$		±0.02	±0.10	±0.07	±0.07	±1.04	±0.46
Equatorial regions[1]		1.08±0.09		1.10±0.10		0.57	
10747 Å	27 Oct. 2004	2.22	2.22	2.25	2.29	0.64	1.42
	25 Oct. 2004	2.23	–	2.21	–	-0.24	–
	27 Oct. 2004	2.17	2.20	2.21	2.28	0.77	1.67
	14 Oct. 2004	2.11	–	2.08	–	-0.56	–
	27 Oct. 2004	2.09	–	2.09	–	-0.04	–
	25 Oct. 2004	2.13	–	2.19	–	1.26	–
Mean (μ)		2.16	2.21	2.17	2.29	0.30	1.54
$\pm\sigma$		±0.05	±0.01	±0.06	±0.01	±0.63	±0.12
Equatorial regions[1]		1.86±0.10		1.88±0.14		0.22	
5303 Å	14 Oct. 2004	0.80	0.83	0.78	0.81	-0.57	-0.31
	14 Oct. 2004	0.83	0.79	0.78	0.78	-1.02	-0.04
	27 Oct. 2004	0.80	0.74	0.74	0.71	-1.16	-0.49
	17 Oct. 2004	0.80	0.82	0.80	0.82	0.11	0.13
	17 Oct. 2004	0.86	0.90	0.86	0.88	0.08	-0.50
	17 Oct. 2004	0.86	0.88	0.86	0.86	0.01	-0.40
	21 Oct. 2004	0.84	0.87	0.79	0.81	-0.92	-1.29
Mean (μ)		0.83	0.83	0.80	0.81	-0.50	-0.41
$\pm\sigma$		±0.03	±0.05	±0.04	±0.05	±0.51	±0.42
Equatorial regions[1]		0.85±0.05		0.82±0.06		-0.66	

[1] Corresponding values at equatorial regions computed from the values in Table III of Singh *et al.* (2003b). For 10747 Å values from Table I of Singh *et al.* (2003a) are used.

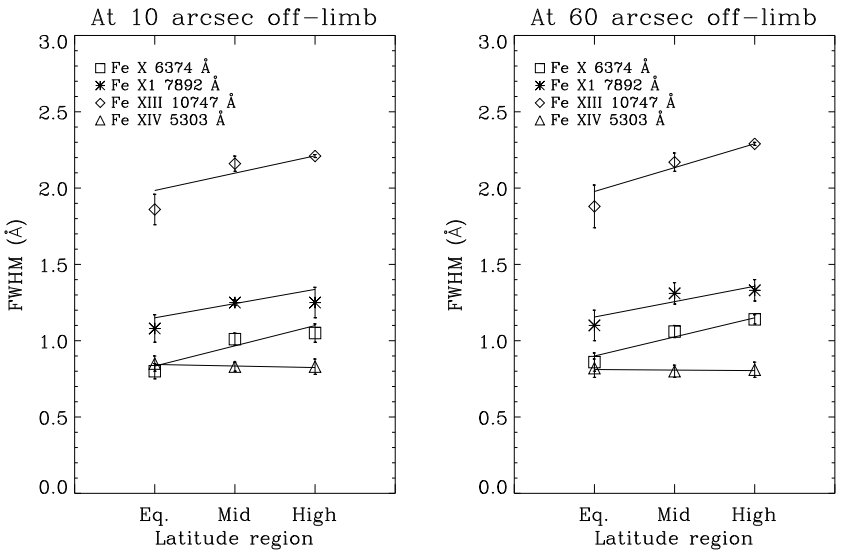

FIGURE 4.6: Change in mean FWHM values from equatorial to mid-latitude to polar regions at 10″ (left) and at 60″ (right) heights above the limb in all four emission lines. Bars at each value denote the standard deviation [σ] at that value as listed in Table 4.4 and the solid lines are the linear fits to the mean values. Different symbols denote different emission lines as given in the legend in the plots.

TABLE 4.5: Change in FWHM from equatorial to polar regions in different emission lines. Values are derived from the linear fits shown in Figure 4.6

Emission line [wavelength]	Change in FWHM (Å) at 10″	at 60″
Fe X 6374 Å	0.26	0.25
Fe XI 7892 Å	0.19	0.20
Fe XIII 10747 Å	0.23	0.31
Fe XIV 5303 Å	-0.02	-0.01

the equatorial, mid-latitude, and polar regions for heights 10″ and 60″ above the limb in Figure 4.6. Vertical bars over the mean values denote the dispersion of FWHM (one-σ values) at these regions and the overplotted solid line is the linear fit to these values. It may be noted that these values do not represent a particular latitude but represent average latitudes of about 20°, 55°, and 75°. So they are not plotted to scale in x-axis. This can alter the fit coefficients significantly, but does not affect the comparison much. Both of the panels in this figure, for 10″ and 60″ heights, indicate significant increase in mean FWHM from equatorial to polar regions, in all of the lines except for the green line, which shows very marginal changes. The quantitative changes for each line in these plots are given

in Table 4.5.

4.5 Discussion

Spectral line width, in the middle and high-latitude corona, is observed to vary with altitude differently in the four emission lines studied. It can be clearly seen from Figure 4.5 and Tables 4.3 and 4.4 that the FWHM of the red line shows a positive gradient and that of the green line shows a negative gradient with height up to 100″ distance off-limb. This implies that the red-line width increases with height and that of the green line decreases with height which is consistent with the earlier results for equatorial regions (Singh *et al.* 2003b). Despite the small number of scans in the other two emission lines, [Fe XI] and [Fe XIII], the trend of variation in FWHM with height in these lines, in polar regions, is similar to that observed in equatorial regions. The IR line at 10747 Å shows mixed behaviour in gradient as seen in the table for mid-latitude, which is consistent with the earlier results. So this complex variation in line widths of different emission lines seems to be global and general, *i.e.* not restricted to any particular region or to the coronal conditions on any particular day.

Several space-based observations indicate different variations in the off-limb line widths. Many of them show an increase in line width with height which is mostly interpreted as due to the presence of outward propagating Alfvén waves. Harrison *et al.* (2002) examined the Mg X 625 Å line in the equatorial quiet region using the CDS instrument on SOHO and observed narrowing of the emission line as a function of altitude above 50 000 km. They attributed this narrowing to the dissipation of Alfvén waves in the close field loops. However, the joint observations from CDS and SUMER by Wilhelm *et al.* (2005) indicate a slight plateau rather than a decrease in the line width. Similar analysis by O'Shea *et al.* (2003) in the north polar coronal hole, extending from the disk part of the coronal hole to ≈90 000 km above the limb suggest a turnover point, around 65 000 km above the limb, where the line widths seem to suddenly decrease or level-off. They further pointed out that this change in behaviour occurs at approximately the

same line width value in each of the data sets examined, suggesting a key value for non-thermal velocity. O'Shea *et al.* (2005) studied the height variation of both line width and line ratio of Mg x 609.78 and 624.94 Å line pair in an off-limb north polar region. They observed that the line widths, after an initial increase, start to decrease at a height (≈1150″) where the dominant excitation changes from collisional to radiative as derived from the line ratio. Based on this, it is suggested that the reduction in the non-thermal velocity, and thereby line width, is somehow linked to the excitation mechanism, probably through changes in electron density. Pekünlü *et al.* (2002) show that Alfvén waves propagating along a magnetic flux tube go through refraction and get damped via viscous dissipation and resistivity under linear incompressible MHD approximation. They see a peak in the energy flux density at about 1.15 $R_\odot$ after which it declines supporting the observational evidences of damping of upwardly propagating waves. Mierla *et al.* (2008), using LASCO-C1 data, found a gradual increase of line width of the red line, and an initial increase followed by a decrease in the case of green line. They suggested that ion−cyclotron heating or propagating Alfvén waves can explain the gradual increase and the resonant absorption of Alfvén waves might explain the decrease of line width after an increase. More recent observations using *Hinode*/EIS, reveal a gradual decrease in line width after an initial increase in polar coronal holes which is attributed to Alfvén wave damping (Bemporad and Abbo 2012; Hahn *et al.* 2012). All of these explanations definitely have their implications in coronal heating and solar-wind acceleration but can not explain the line width increase with height in one line and decrease in the other, of a co-spatially and simultaneously observed pair.

Singh *et al.* (1999) and Singh *et al.* (2006a) explained this complex behaviour of line widths in terms of gradual mixing of different temperature plasma with increasing height. Although, this explanation seems to fit the observations very well, this model requires the interaction between different temperature plasma, magnetically isolated near the foot points and gradually mixed with increase of altitude. This may not be easy in a low-β environment such as the solar corona, more particularly in polar regions. May be the different temperature plasma regions in a loop are not magnetically isolated, instead they are physically connected through thermal conduction, as suggested by Akiyama *et al.* (2005). It is possible that individual loop structures that are observed have many strands at sub-pixel

resolution. If we assume that these strands are fed by small-scale impulsive events such as nano flares and have shorter life span compared to the broader loop structure, then the disappearing strands with different temperature plasma may allow interaction between them. Such impulsive heating events were considered by several authors. For instance, Mendoza-Briceño *et al.* (2002) performed a numerical study on heating of coronal loops by random energy releases near the footpoint.

Now coming to the latitudinal changes, FWHM values are considerably higher in the polar region as compared to the equatorial region, for all of the lines except the green line. This behaviour of the green line is surprising! Contesse *et al.* (2004) analysed the spectra in the green line at several off-limb locations both in equatorial and polar corona up to $12'$ heights above the limb. They did not find any decrease in the green-line width with height, besides finding higher values of line width in the polar regions. Our current findings do not seem to agree with their results although a direct comparison is difficult due to the observations at different coronal heights. However, our findings assume importance because of the better spectral and spatial resolutions, closely spaced observations, and the large data base generated from observations made on a number of days. If the temperature difference, anything present between the polar and equatorial regions is ignored, the higher FWHM values imply higher non-thermal velocities in the polar regions. So, these results may suggest the existence of a non-thermal source, such as waves or turbulence, that can possibly provide additional energy to power the fast solar-wind acceleration and may also indicate that the acceleration of the solar wind takes place at the base of the solar corona itself. But then the reason for the lack of change in FWHM of the green emission line becomes a puzzle.

Chapter 5

Propagating Intensity Disturbances in Open Structures

Propagating quasi-periodic intensity disturbances were first observed in polar plumes and were interpreted as slow magneto-acoustic waves based on the propagation speeds and other observed properties. Similar disturbances were later observed in the extended loop structures at the edges of active regions but with shorter periods. These are usually identified from the alternating, slanted, bright and dark ridges in the space-time maps constructed from a sequence of images. Although the initial energy calculations indicate their inability to meet the coronal heating requirements, ample amount of observations on these waves proved them to be useful for seismological applications. But, some of the recent spectroscopic studies suggest the requirement of a careful inspection on the nature of these disturbances, as the quasi-periodic upflows ambiguously produce similar signatures in intensity images. In this context, propagating intensity disturbances were studied in open/extended structures at both polar regions and active regions. Several properties were identified and necessary tools/techniques were developed to unambiguously differentiate the slow waves from periodic upflows using imaging and spectroscopic observations[1]. These elements are discussed in this chapter.

[1]Results of this work are published in Krishna Prasad *et al.* (2011, 2012a)

5.1 Introduction

Polar corona, dominated by the open field lines, contains elongated tube like structures projected out from the Sun called polar plumes. These structures are prominent during solar minimum. The dark lanes between the plumes, are called interplume regions. Plumes and interplumes are characterized by slightly different properties. Plumes are denser and cooler than interplume regions (e.g., Wilhelm 2006). Interplume regions exhibit broader line profiles than plumes (Banerjee *et al.* 2000b). Quasi-periodic intensity variations were first reported in polar plumes using the white light channel of UVCS/SOHO (Ofman *et al.* 1997). They proposed that they are signatures of compressional waves. Soon after, observations from EIT/SOHO revealed their ubiquitous presence in the polar regions (Deforest and Gurman 1998). Ofman *et al.* (1999, 2000) interpreted these disturbances as slow magneto-acoustic waves. Similar work has been performed by many others using spectroscopic observations of CDS/SOHO (Banerjee *et al.* 2000a, 2001a,b; O'Shea *et al.* 2006, 2007) and more recently using SUMER and EIS (Banerjee *et al.* 2009b; Gupta *et al.* 2010), and all concluded that these disturbances were magneto-acoustic waves (Banerjee *et al.* 2007).

Active regions are dominated by close field lines in contrast to the polar regions. Oscillations in active regions had been reported by several authors, both from imaging (Nightingale *et al.* 1999; De Moortel *et al.* 2000; Robbrecht *et al.* 2001; King *et al.* 2003; McEwan and De Moortel 2006) and spectroscopic (Ireland *et al.* 1999; O'Shea *et al.* 2001, 2002; O'Shea and Doyle 2009; Mariska *et al.* 2008; Mariska and Muglach 2010; Wang *et al.* 2009a,b) observations. The periods observed are usually shorter compared to the polar regions. Ireland *et al.* (1999) and O'Shea *et al.* (2001) find oscillations with periods as short as 1 min using observations from CDS/SOHO. In a recent study, O'Shea and Doyle (2009) reported active region oscillations over a range of frequencies from 2 mHz (500 s) to 154 mHz (6.5 s) using the *Extreme-ultraviolet Imaging Spectrometer* (EIS) onboard *Hinode*. At the edges of the active regions, one can find expanding fan like loop structures which often host propagating disturbances (PDs) similar to that observed in polar regions. These extended loop structures were also widely studied using imaging observations mainly from TRACE (for *e.g.* Schrijver *et al.* 1999; King *et al.* 2003;

De Moortel *et al.* 2000, 2002b,a) and EIT/SOHO Berghmans and Clette (1999). Statistical studies on PDs observed in active region loops indicate that the average values of the propagation speed, amplitude relative to the background and periodicities are 99.7±3.9 km s^{-1}, 3.7±0.2% and 284±10.4 s, respectively (see the review by De Moortel 2009). Simultaneous observations from TRACE and CDS/-SOHO by Marsh *et al.* (2003), also reveal intensity oscillations of 5 min periodicity. Only recently, longer periods (12 min and 25 min) were reported in these loops (Wang *et al.* 2009b) both in intensity and velocity using spectroscopic data from EIS/*Hinode*. Majority of these reports conclude the observed oscillations as due to magneto-acoustic waves. There are also a few reports on outflows from the edges of active regions which can contribute significantly to the slow solar wind (Sakao *et al.* 2007; Harra *et al.* 2008; McIntosh and De Pontieu 2009).

Detection of waves and oscillations in the outer solar atmosphere is useful not only to understand their role in coronal heating but also to remotely diagnose the properties of the corona using a technique called coronal seismology (Uchida (1970); Roberts *et al.* (1984); refer to Banerjee *et al.* (2007) and Mathioudakis *et al.* (2013) for nice reviews on this subject). It is this advantage that motivated many studies on PDs despite their energy being insufficient to heat the corona. But recently, McIntosh *et al.* (2010) studied PDs in polar plumes using observations from STEREO and suggested that these are high speed quasi-periodic outflows rather than waves. After a detailed spectroscopic analysis, De Pontieu and McIntosh (2010) pointed out that the oscillations in intensity and velocity observed for the PDs, in some cases, are accompanied by in-phase oscillations in line width of the same period when the line profiles are fitted with a single Gaussian. They show that the presence of faint quasi-periodic upflows driven from below leading to an additional blue-shifted component in the line profile can cause oscillations in all the three line parameters. Hence, it is difficult to differentiate between waves and flows using only imaging data. Similar reports on PDs supporting the quasi-periodic upflow scenario were made by Tian *et al.* (2011) using the simultaneous observations from XRT and EIS. More recently, Nishizuka and Hara (2011), using data from EIS/*Hinode*, reported the observation of propagating slow mode waves along the continuous outflow. They found an increasing correlation between intensity and velocity disturbances as one moves away from the base of the outflow region. A clear understanding of the basic physical mechanism

involved is essential to quantify the significance and contribution of these PDs to coronal heating and/or fast wind acceleration. It is important to verify the wave nature of these disturbances before proceeding to the seismological applications. Using different observations, PDs in a polar region and in an active region fan loop system were studied to understand their exact nature. Details of the observations, analysis methods employed, and the results obtained, are discussed in the following sections separately for these two regions.

5.2 Propagating Disturbances in Polar Regions

Propagating intensity disturbances were known to be present ubiquitously in the polar corona. Imaging data from different temperature channels were used to investigate the nature of these PDs.

5.2.1 Observations

Atmospheric Imaging Assembly[2] (AIA; Lemen *et al.* 2012) onboard SDO, images the full-disk Sun in 10 different channels nearly simultaneously. Three of the coronal channels centred at wavelengths 171 Å, 193 Å, and 211 Å, are chosen for this study. These three coronal channels correspond to their emissions mainly from Fe IX, Fe XII, and Fe XIV and their temperature responses peak at 0.8 MK, 1.25 MK, and 1.6 MK, respectively. Hereafter, the central wavelengths are used to refer to these channels. A data block of two hours length corresponding to the observations on July 20, 2010 from 02:00 UT to 03:59 UT is selected. It is Rice compressed, calibrated level 1.0 data and is directly used in this analysis without applying any further corrections. De-rotation is not performed, since the rotation effect would be insignificant in this analysis. Fewer than ten frames out of 600 frames from these two hours, in each passband are missing, which are added by

[2]Refer to Section 2.1.1.1 for instrument details.

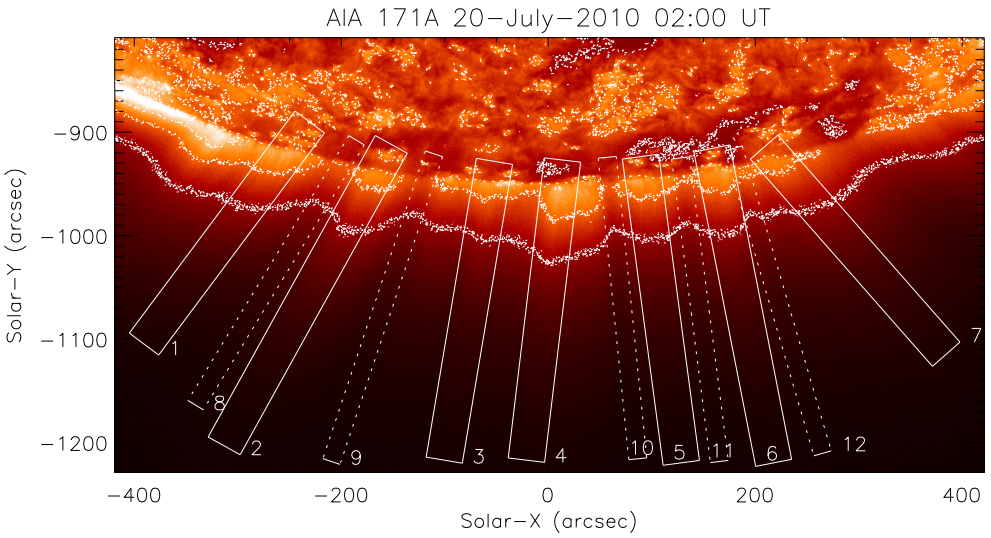

FIGURE 5.1: South polar region of the Sun as seen by SDO/AIA through one of its EUV channels centred at 171 Å. Overplotted dotted curves are the contours for three different intensity levels indicating clear plume and interplume structures. The rectangular boxes delineate the locations of artificial slits extracted for the analysis, following intensity contours. Slits over plume regions are 60 pixels (≈36″) wide and those over interplume regions are 30 pixels (≈18″) wide. These are marked differently using solid lines for plume locations and dotted lines for interplume locations. Slit numbers are labelled at the bottom right of each slit.

linear interpolation. South polar region was chosen for this study for its clear plume structures. AIA pixel size is ≈0.6″ and the cadence is 12 s.

5.2.2 Analysis & results

The selected sub-region near the Sun's south pole is shown in Figure 5.1. Several plume and interplume regions were identified by following the peaks and depressions in intensity using different contour levels. Artificial slits of 60 pixels (≈36″) width in each plume region and 30 pixels (≈18″) width in each interplume region, are extracted from each time frame, averaged over width and stacked together to construct space-time maps. A total of 12 slits, seven in plume and five in interplume regions, were chosen covering the on-disk part of the plumes wherever visible and extended almost to the end of the AIA field of view. The intensity contours and chosen slits with their exact widths are overplotted with solid (plume)

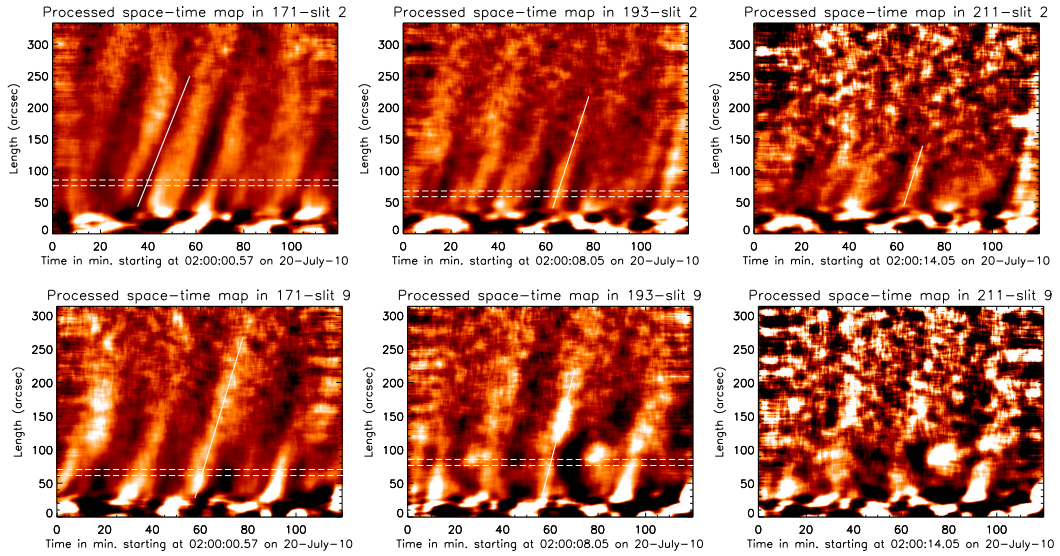

FIGURE 5.2: Space-time maps with time on X-axis, constructed from slits 2 and 9 (See Figure 5.1) and processed, in all the three coronal channels of AIA, 171 Å, 193 Å, and 211 Å. Top panels are for slit 2 (plume) and those in the bottom are for slit 9 (interplume). The slanted solid line following the ridges is used for the propagation speed estimation. The horizontal dotted lines enclose the rows averaged for wavelet analysis. See text for details.

and dotted (interplume) lines in Figure 5.1. The slit numbers are marked at the bottom right of each slit. Different widths are chosen to isolate interplume regions from the plume regions, hence study them separately. Same locations are used in all the three passbands as shifts of a few pixels between them (because of any misalignment), if at all present, can be ignored. The space-time maps thus obtained for each slit are then processed to bring up the low amplitude oscillations. A background obtained by smoothing the space-time map in time over 200 points (≈40 min) is subtracted and the resultant is normalized by the smoothed image. The background subtraction enhances the faint variations and the normalization will take care of the radial intensity fall. Any quasi-periodic disturbance in intensity, propagating along the slit will appear as alternate bright and dark ridges in this processed map. These processed maps for slit 2 (plume) and slit 9 (interplume), can be seen in Figure 5.2. The slanted bright and dark ridges can be clearly seen in all these maps, except in those for 211 Å channel. It can also be seen that one such disturbance travelled almost 250″off-limb, reaching the end of slit, and might have travelled yet further. The slope of these slanted ridges gives the projected propagation speed of the disturbance, and the spacing between two successive ridges gives the periodicity. Since these ridges are fainter and rarely

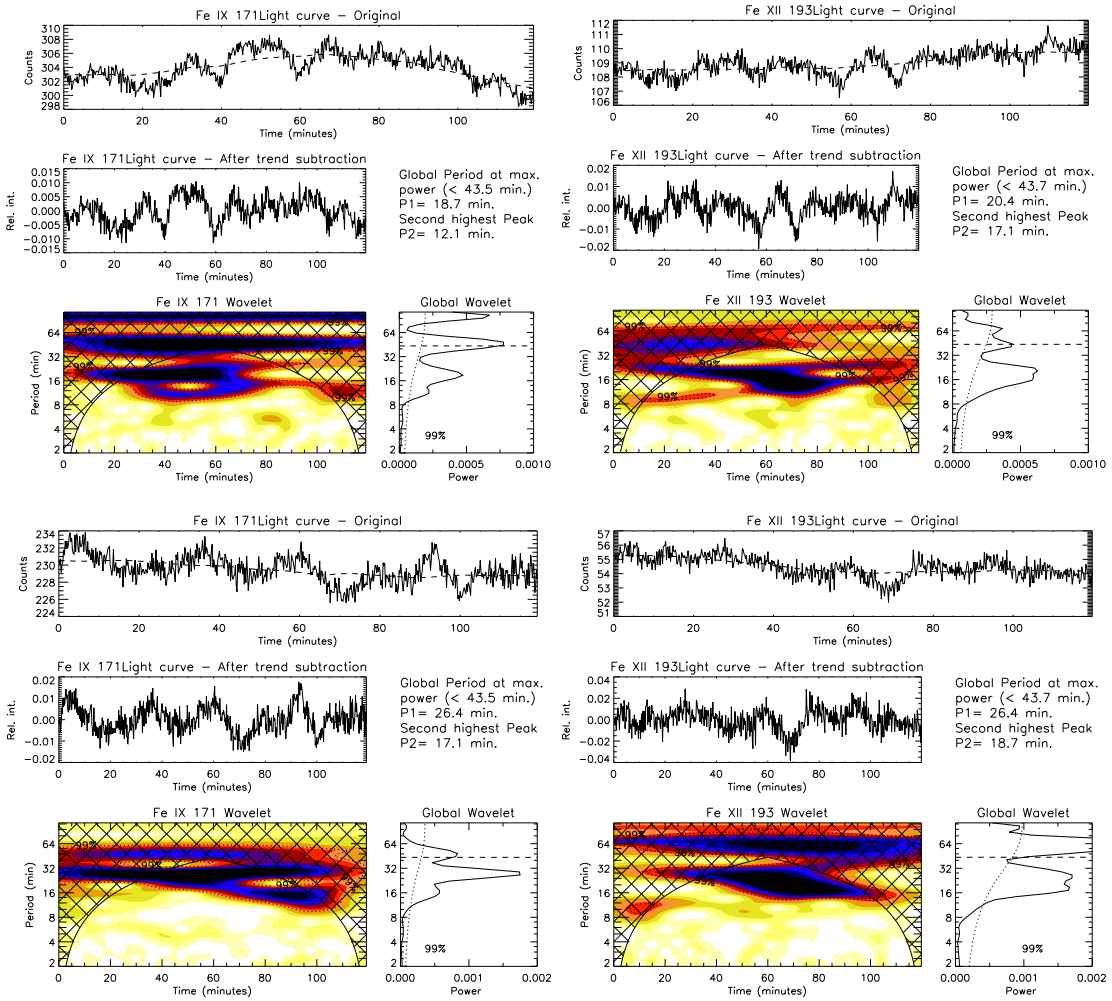

FIGURE 5.3: Wavelet analysis results for slits 2 (top) and 9 (bottom) marked in Figure 5.1. Top two panels in each of these plots, show the light curves, original and background-trend-subtracted, for the region enclosed by horizontal lines in Figure 5.2. The bottom left panel shows the wavelet plot with contours enclosing the 99 % confidence regions, for a white-noise process. Bottom right panel is the global wavelet plot with 99 % global confidence level, overplotted as a dotted line. The periods of primary and secondary peaks are also written in the text (middle-right).

seen in 211 Å, further analysis is limited to 171 Å and 193 Å channels. The speeds are calculated by fitting straight lines to the ridges and periodicity calculations are performed using a wavelet analysis. The horizontal lines marked on Figure 5.2 enclose the region averaged and used in our wavelet analysis. Morlet function is used as the mother wavelet (see Torrence and Compo 1998). Results of the wavelet analysis for slits 2 (top) and 9 (bottom) can be seen in Figure 5.3. The top panels of each subfigure in Figure 5.3 shows the original light curve which sometimes

TABLE 5.1: Observed periods and projected propagation speeds for all the slits marked in Figure 5.1, in both 171 Å and 193 Å.

Slit No.	Fe IX 171 Å		Fe XII 193 Å	
	P1(P2) (min)	Speed (km s^{-1})	P1(P2) (min)	Speed (km s^{-1})
1	24.3 (13.2)	103.2±1.4	28.8 (12.1)	133.1±2.3
2	18.7 (12.1)	113.8±1.4	20.4 (17.1)	140.2±2.3
3	31.4 (13.2)	110.9±1.5	26.4 (13.2)	124.2±1.6[1]
4	18.7 (11.1)	117.5±1.9	22.2 (10.2)	142.2±3.2[2]
5	28.8 (14.4)	109.9±1.6	26.4 (10.2)	137.6±2.5
6	26.4 (12.1)	116.5±1.7	24.3 (17.1)	132.6±1.9
7	28.8 (18.7)	121.5±2.1	31.4 (17.1)	136.9±3.4
$\mu \pm \sigma$		113.4±5.6		135.2±5.6
$\pm\delta$		±0.6		±0.9
8	24.3 (14.4)	137.4±2.3	24.3 (14.4)	149.8±2.6[1]
9	26.4 (17.1)	142.5±1.8[1]	26.4 (18.7)	164.7±2.9[1]
10	18.7 (12.1)	144.9±2.7[2]	18.7 (11.1)	153.9±3.6[2]
11	24.3 (...)	127.2±1.6[1]	22.2 (...)	167.4±3.8[1]
12	20.4 (13.2)	121.2±2.1	28.8 (15.7)	165.1±3.9
$\mu \pm \sigma$		134.6±9.1		160.2±7.0
$\pm\delta$		±0.9		±1.5

Notes. P1 and P2 are the primary and secondary periods (see Figure 5.3). μ is the average of all the values above, σ is the standard deviation representing statistical error, and δ is the instrumental uncertainty propagated from individual values.

[1] Jet-like features that can be seen from the movies.

[2] Enhanced intensity regions showing a decelerating ridge at the end of space-time map. This is due to an eruption from a region above slits 4 and 10.

contains longer periods that may be due to background variations. These are removed by choosing the appropriate background from the running average (over 50–60 min) of the original, which are overplotted. The middle panel shows this background trend subtracted light curve. The description of other panels can be found in corresponding figures. The primary and secondary peaks in periodicities, represented as P1 and P2, are well above the 99 % confidence level (Torrence and Compo 1998) for a white noise process. The periods and propagation speeds obtained for all the slits are tabulated in Table 5.1. If the second peaks are not available or below the 99 % significance level, they are marked by an ellipsis (...) in the table. The periodicities are in the range of 10–30 min and the propagation speeds are 100–170 km s^{-1}. The errors in the calculation of speed, are due to instrumental uncertainties, given by $\delta v = v(\frac{\delta x}{x} + \frac{\delta t}{t})$, where v, x, and t are the

propagation speed, and the vertical and horizontal extents of the lines marked in space-time maps, and in addition, δx, and δt are the pixel scale ($0.6''$) and time cadence (0.2 min), respectively. The errors are small, owing to the high spatial and temporal resolutions of the instrument, but the true uncertainty in the slope measurement might be larger than this. One may alternatively consider the width of the strip, in time direction as δt, but despite choosing the narrower ones, the uncertainties are too large and the actual human error would be definitely smaller than this. Hence, the standard deviation (σ) over the average propagation speed (μ) of all the values is considered as the measurement error. These values are listed in the table. There is a noticeable difference in the average speeds between plume and interplume regions and also between different passbands.

Mostly in 193 Å passband, in a few cases, one or two ridges were found to be steeper and brighter than other ridges. In one instance, a decelerating bright ridge at the end of the time sequence was observed, and found to be brightest in 211 Å. The former case is identified as the effect of strong jets and the latter is due to an eruption that occurred just above the slits 4 and 10 and propagated off-limb. The slits affected by these events are marked in Table 5.1. The eruption can be seen most clearly from the processed movies available online[3]. Stronger jets should be identifiable in the original movies since the movies, processed to extract the fainter variations ($< 5\%$) may produce the same visual impression for both waves and jet outflows. The fainter jets, if at all present, do not affect this analysis because of the wider slits.

5.2.3 Discussion

Several plume and interplume structures were studied, using contrast-enhanced images recorded in three coronal channels 171 Å, 193 Å, and 211Å of SDO/AIA, to understand the nature of quasi-periodic propagating disturbances in intensity. PDs were identified in all the structures studied confirming their ubiquitous presence observed earlier. They appear very faint in 211 Å channel which limited the analysis to two channels. For the construction of space-time maps, artificial slits

[3] ftp://ftp.iiap.res.in/krishna/aia_polar

wider than usual were chosen to avoid the effects of fainter (few % above background) jets, if any were present. It is appropriate here to note that, although the case with 60 (plume) and 30 (interplume) pixel widths is presented here, the results did not change for slits as wide as 90 pixels (≈54″) and as narrow as 15 pixels (≈9″) which implies that a coherent mechanism is involved in producing these PDs. Since the jets cannot be produced so coherently, the wider slits will average out the effect of fainter jets, but the strong jets may remain. Using simple calculations, one can roughly estimate that a jet of a five pixel (≈3″) width and of intensity 10 % above background will become a $< 1\%$ variation assuming there is one jet at a time inside the 60 pixel slit. Hence, the stronger ($> 10\%$) jets may appear in the space-time maps, but can be easily identified from the movies and filtered out. Few such examples were seen and most of them were easily identified from the presence of distinct ridges with steeper slopes that are indicative of higher speeds. A faster jet that was indistinguishable from the other ridges because of its inclination to our slit 9, was also identified. These cases increase the ambiguity and shall be avoided by a careful inspection of movies. Following these steps carefully, most of the jets were avoided and still the propagating quasi-periodic disturbances were seen in almost all cases and more importantly they were found to be insensitive to changes in slit width within certain limits. Deforest *et al.* (1997) suggested that the ionization temperature of the plume and interplume regions is around 1.0-1.5 MK. The PDs observed here are clearly seen in 171 Å and 193 Å but rarely in 211 Å, whereas the jets are seen mostly in 193 Å and 211 Å. This might be because jets are streams of hotter (than background) material whereas the (compressive) waves are local modulations in density. Another point is, though the periodicity values range from 10 min to 30 min there being three periodicities in most cases, with the first one varying between ≈12 min and ≈18 min, the second one in-between 18 min, 24 min, and 30 min, and the third one around 45 min (though, inside the cone of influence, see global wavelet plots in Figure 5.3). The repeated presence of these selective periodicities might be indicative of harmonics. Furthermore, the difference in the propagation speeds between 171 Å and 193 Å cannot be explained by a multi-thermal jet or outflow scenario whereas the temperature dependence of acoustic speed can explain the difference. The acoustic speeds are related to temperature by the formula, $C_S \approx 152\, T^{1/2}\ m\ s^{-1}$ with T in K, as given by Priest (1984). The ratio of observed speeds is 1.19, which can be compared to the theoretical value 1.25 which is obtained considering the peak temperatures of

171 Å (0.8 MK) and 193 Å (1.25 MK). Now, comparing theoretically estimated acoustic speeds in 171 Å (136 km s^{-1}) and 193 Å (170 km s^{-1}) to those observed average values listed in Table 5.1, it is suggested that these disturbances are more likely to be due to slow magneto-acoustic waves rather than due to periodic upflows. However, if the actual uncertainties in speed calculations are larger (about 20%) then the difference in speed can be negligible and the interpretation in terms of acoustic type may not be valid. Coordinated imaging and spectroscopic observations are more useful to explore the exact nature of these disturbances, as demonstrated by De Pontieu and McIntosh (2010) and Tian *et al.* (2011).

An attempt has been made to use the 211 Å and 171 Å pair, since their acoustic speed ratio is large. But, as mentioned earlier the ridges are barely visible in 211 Å channel and it was possible only for slit 2 (see Figure 5.2). The measured propagation speed for slit 2 in 211 Å is 142.3±4.4 km s^{-1} and the speed ratio with respect to 171 Å is 1.25 compared to the theoretical value 1.41. It is also often debated whether the plumes (Casalbuoni *et al.* 1999; Gabriel *et al.* 2003, 2005) or the interplumes (Wilhelm *et al.* 2000; Teriaca *et al.* 2003; Gupta *et al.* 2010) are the preferred channels for the acceleration of the fast solar wind. The propagation speeds observed here are slightly higher for the interplume case, but there is no noticeable difference in the ridge pattern unlike the case reported by Gupta *et al.* (2010) who observed acceleration in these regions. The slight curvatures observed at the bottom of the ridges, close to the limb, could be more due to projection effects.

5.3 Propagating Disturbances in Active Region Fan Loops

Extended loop structures at the edges of active regions, are known to host propagating disturbances similar to that observed in polar regions. Spectroscopic observations made over an active region fan loop system were combined with simultaneous imaging observations from AIA to study the nature of these disturbances. Other active region oscillations observed in this study, will also be discussed.

5.3.1 Observations

Spectroscopic observations were planned and made with EIS[4] to study high frequency oscillations and to perform plasma diagnostics in active region loops. The target region was NOAA active region (AR) 11076 when it was close to the west limb on June 5, 2010. Initially, a context raster was taken with the 2″ slit starting at 10:57:27 UT, covering a region of 82″ × 400″. This was followed by a temporal sequence of 150 exposures with the 40″ slot at nearly 5 s cadence. Three consecutive sets of sit-and-stare observations taken after this, with the 1″ slit, each of 100 exposures at ≈6 s cadence completed the observational sequence. The three sit-and-stare sets were taken at the same location with a short time gap of 7 s to 8 s between each set. These observations were made under the Hinode Operation Plan, HOP 156. The slit position in the sit-and-stare mode, was found to cross the fan loop system of the target active region which compelled us to use this dataset to study PDs, though it was not the main goal of this observation. Co-temporal and co-spatial imaging observations from SDO/AIA, are also used. The locations of the slits, slot and the region covered by the raster are marked over the subfield of an AIA image, which is shown in left panel of Figure 5.4. It can be seen that a part of the slit is located over the active region fan loops. Our primary focus in this work is only on sit-and-stare observations by this slit. These observations were made in 5 spectral lines of EIS, out of which, two lines Fe XII 195.12 Å and Fe XIII 202.04 Å are used in this work. The other lines were ignored either due to poor signal or due to blending issues.

Standard reduction procedure[5] had been followed in preparing the EIS data to make it suitable for further analysis using the routines available in Solar SoftWare (SSW). This procedure involves corrections for dark current and detector bias, removal of warm, hot and saturated, and dusty pixels, removal of cosmic rays, and applying a radiometric calibration which results in intensities in absolute units. The spectra were then fitted with single Gaussian line profiles plus a background to get the spectral parameters namely, line intensity, peak position, and line width. Before fitting, a three-pixel binning is done in the spatial dimension along the slit

[4]Instrument details are described in Section 2.1.2.1
[5]Step-to-step procedure is explained in Section 2.2.2

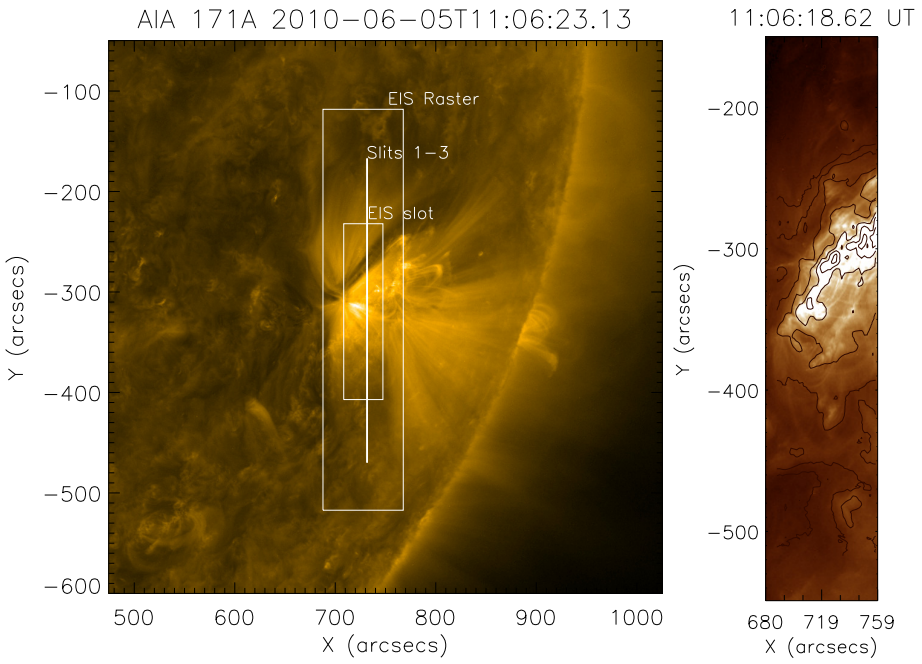

FIGURE 5.4: *Left:* A snapshot of the region covering AR 11076 taken during the time of EIS raster using AIA/SDO in 171 Å channel. Overplotted outer box displays the region covered by EIS raster, inner box indicates the location of EIS 40″ slot and the vertical line denotes the position of EIS slit used in sit-and-stare mode. *Right:* Portion of the AR covered by EIS raster, taken in the 193 Å channel of AIA. Overplotted curves in black are intensity contours constructed from EIS raster after accounting for the offsets between the two instruments. This panel illustrates the goodness of the alignment.

to improve the signal. The fitting task for the whole time sequence is automatically done using `eis_auto_fit.pro` routine. This routine corrects for the EIS slit tilt and orbital variation in the line centroids. This also does the absolute wavelength calibration using the method described in Kamio *et al.* (2010) and reference wavelengths for the Doppler shift measurements were taken from rest wavelengths listed in Brown *et al.* (2008). The maximum shifts in the position of the slit during the observations, due to instrument jitter are -0.86″ and +0.12″ in X and -2.3″ and +0.64″ in Y directions, as given by the routine `eis_jitter.pro`. Since the effective spatial resolution in Y-direction is 3″ (binned over three pixels), the effects of jitter may be small. An isolated bright structure along the slit does not show any visible shifts in its position during the entire observation confirming this.

Subfield images from AIA/SDO, covering the active region, in two coronal channels

centred at 171 Å and 193 Å are also used. A total of 900 images (≈3 hrs duration at 12 s cadence), in each channel, roughly starting at 10:00:11 UT, covering the EIS observation time, are used here. The initial data set was at level 1.0 which has already been processed to make basic corrections like removal of dark current, cosmic spikes, bad pixels etc. The routine `aia_prep.pro` (available with SSW) was then used to adjust the plate scales and roll angles in different channels to a common value. This transforms the data from level 1.0 to level 1.5[6]. All the subfield images are tracked for solar rotation taking the reference time as the time when slit was roughly at the centre of the raster.

Pointing offsets between EIS/*Hinode* and AIA/SDO were calculated using the intensity cross-correlation technique to overlay the spectroheliogram constructed from EIS raster in Fe XII 195.12 Å line on the AIA subfield, closest in time, taken through 193 Å channel. Panel on the right in Figure 5.4 shows the EIS raster in 195.12 Å line overplotted on corresponding AIA subfield, after applying the offsets. Visual inspection by zooming into the smaller features tells that the alignment should be accurate at least up to a couple of arcseconds.

5.3.2 Data Analysis

The techniques used to detect the oscillations and their properties observed both from AIA/SDO and EIS/*Hinode* data are discussed in this section. The portion of the slit crossing the fan loop system had been explored for temporal variations in different line parameters and two locations were identified with significant oscillations. Figure 5.5 displays the AIA images, taken during EIS raster observations, in two channels 171 Å and 193 Å, with the locations of our interest marked. The region enclosed by the box marked with dash-dotted lines in the left panels, is processed using the unsharp masking technique to show the fine structure, and displayed on right for a closer view. Unsharp masking is done by taking a boxcar smooth of 8×8 pixels and subtracting it from original. In all the panels, the vertical line represents the location of the EIS slit, horizontal cuts mark the positions of the two EIS pixels identified with significant oscillatory behaviour and the curved

[6]All the steps involved in converting the raw data to level 1.5 are described in Section 2.2.1

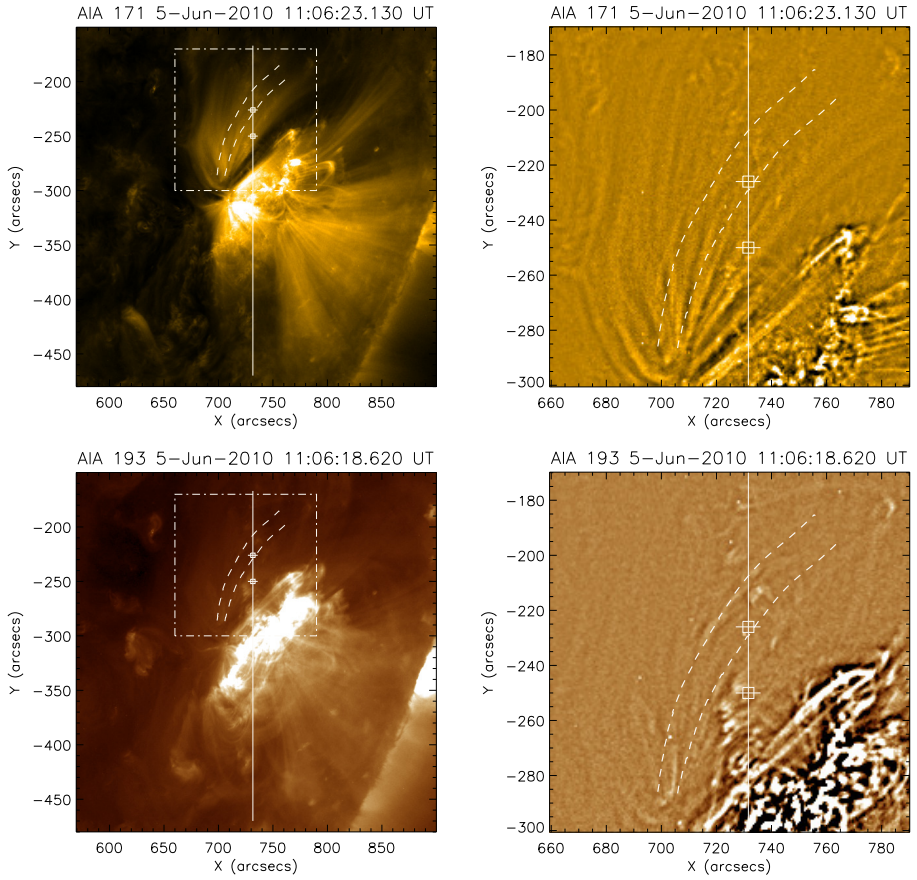

FIGURE 5.5: Snapshots of the active region (left panels) taken during the EIS raster time, in 171 Å and 193 Å channels of AIA. In both rows, images on the right are produced from the box region marked over the images on left by subtracting an 8×8 pixel boxcar smoothed image of each from itself. The vertical line marks the slit position and the horizontal cuts correspond to the locations over EIS slit displaying significant oscillatory behaviour. The top and bottom cut locations correspond to solar-Y positions of -226″ and -250″ respectively. Overplotted boxes at each of these cuts, represent the corresponding region from AIA used in the analysis. The dashed curves enclose a portion of the fan loop system used in the space-time analysis.

lines enclose the loop region analysed from AIA data. Square boxes marked over each cut also represent the corresponding AIA regions analysed. The locations of these two cuts, top and bottom, correspond to -226″ and -250″ , respectively, in solar-Y. Oscillations with long periods ($\approx$ 9 min) were found at the top cut location and that with short periods ($<$ 3 min) were found at the bottom cut location. It should be noted that the terms long and short used here are relative and are used only with reference to the observed periodicities from this particular dataset. Now let us investigate these oscillations in detail to understand their nature.

5.3.2.1 Long period oscillations

The location marked by the top horizontal cut in Figure 5.5 (solar-$Y \approx$ -226″), shows oscillations of longer periods, roughly of the order of 9 min. This pixel location falls over the portion of fan loops with no visible background structure. Since, the duration of each sit-and-stare set is around 10 min, all the three sets were combined to observe such long periods. The short time gap (7 s to 8 s) between each set allowed us to do this easily. There are 8 missing frames, not all consecutive, probably due to telemetry loss, in the first set which are linearly interpolated. Light curves from EIS in intensity, velocity, and line width were constructed from this pixel location. A square region (see Figure 5.5) of dimension 3″ centred around this pixel has been chosen from each AIA channel (171 Å and 193 Å) and co-temporal light curves are constructed from intensity averaged over this region. Since the AIA data is available throughout the observation time we construct AIA light curves of slightly longer duration to increase the frequency resolution. Note that increasing the duration allows the longer periods to come in whose amplitudes are normally larger and carries more power suppressing the shorter periods. So, it is optimally chosen.

Wavelet technique (Torrence and Compo 1998) was used to find the periodicities present in these light curves. Figure 5.6 shows some of the results. These plots show results for intensity, Doppler shift and line width in EIS Fe XII 195.12 Å line and intensity in AIA 193 Å channel (See the corresponding labels to identify individual plots). Each light curve from EIS in intensity, Doppler shift, and line width, was smoothed over 8 temporal points before proceeding for wavelet analysis. This removes any variations shorter than ≈48 s. For AIA, the light curves are directly used without doing any such smoothing. These are shown in the top panels of each plot in Figure 5.6. All of them clearly show some oscillatory behaviour. A 110 point (≈ 11 min) running average for EIS and that with 55 points (≈ 11 min) for AIA light curves, was subtracted from these to filter the longer periods. In all the cases discussed in this analysis the long period filtering is chosen such that no reliable periods are eliminated from EIS and the equivalent filtering scale is followed in AIA. The subtracted trend is shown with a dashed line overplotted on the light curves in the top panels. The resultant light curves are displayed in

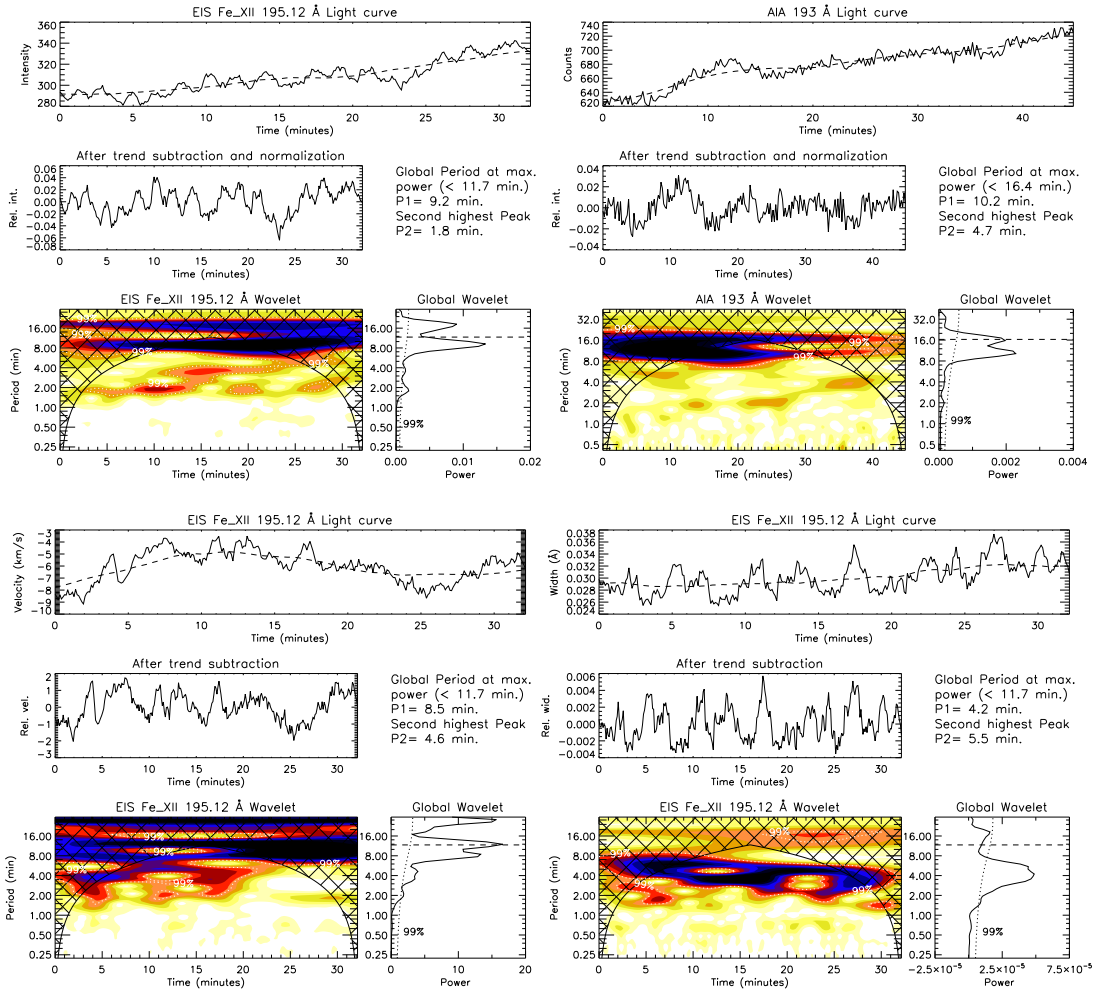

FIGURE 5.6: Wavelet analysis results for the location marked by the top cut (solar-$Y \approx$ -226″) in Figure 5.5. These plots are for intensity, velocity and line width in Fe XII 195.12 Å EIS line and intensity in 193 Å channel of AIA. See text for the description of individual panels and other details.

the middle panel of each plot. For the intensity, the resultant light curves are also normalized by the subtracted trend and displayed here. These are input to the wavelet program for identification of various periods. The wavelet results are displayed in the bottom left panels of each plot in this figure. This shows the different periodicities present and their temporal evolution. The cross hatched region in this plot is the region that can suffer from edge effects and hence the periods observed in this region are not reliable. This region is called Cone of Influence (CoI; Torrence and Compo 1998). The power at different periods is averaged over time and displayed in the bottom right panels of each plot. This is called the global wavelet plot which shows the strength of different frequencies for the total duration. The dashed horizontal line in this plot marks the cut

off for the longest period that can be observed from this data. Different peaks observed in this plot indicate simultaneous presence of different periodicities. The confidence of detection of these periods is measured by calculating a significance level assuming a white noise process (Torrence and Compo 1998). A curved dotted line overplotted on this plot marks this level for 99% significance. This essentially means that the probability that any peak above this level is real, is 99%. The peak periodicity values above this level are identified and the top two strongest periods are listed as P1 and P2 in the text adjacent to the central panels. Oscillations with periodicity around 9 min (see Figure 5.6) were found with 99% confidence both in intensity and velocity, but not in line width. Corresponding results in intensity from AIA 193 Å channel show a broader peak at 10.2 min which may or may not correspond to this period. However, results from 171 Å channel show this period clearly peaking at 9.4 min. Though not significant, a period at 4.7 min is observed in both channels.

To verify this further and extract more information, imaging data from AIA in 171 Å and 193 Å channels were used. The duration of this dataset is 3 hrs covering the EIS observation time. Details on preparation of this data is given in Section 5.3.1. A portion of the fan loop system that crosses the slit and encloses the pixel location marked by the top cut (solar-Y $\approx$ -226″) in Figure 5.5, was selected. Dashed curves in this figure bound the chosen loop portion. An analysis similar to that described in De Moortel *et al.* (2000) was followed, to construct a space-time map for this region. First the selected region was divided into several cross-sections depending on the average length of the loop. Counts in each cross-section were then summed and normalized to the number of pixels in that region. This results in a 1-D array of average counts along the length of the loop. All such arrays from different snapshots of the time sequence were stacked together to construct a space-time map. These maps were then processed by detrending and normalizing, to enhance fine variations. Smoothing over 55 points was used while detrending which normally filters out all the periods longer than 11 min. Figure 5.7 shows these processed space-time maps in 171 Å and 193 Å channels of AIA. Alternating slanted ridges, representing the propagating disturbances, are visible in both the channels. Positive slope indicates that they are propagating outward. This analysis was also done for the hotter 211 Å channel of AIA but these disturbances were hardly visible. To measure the periodicity, a light curve

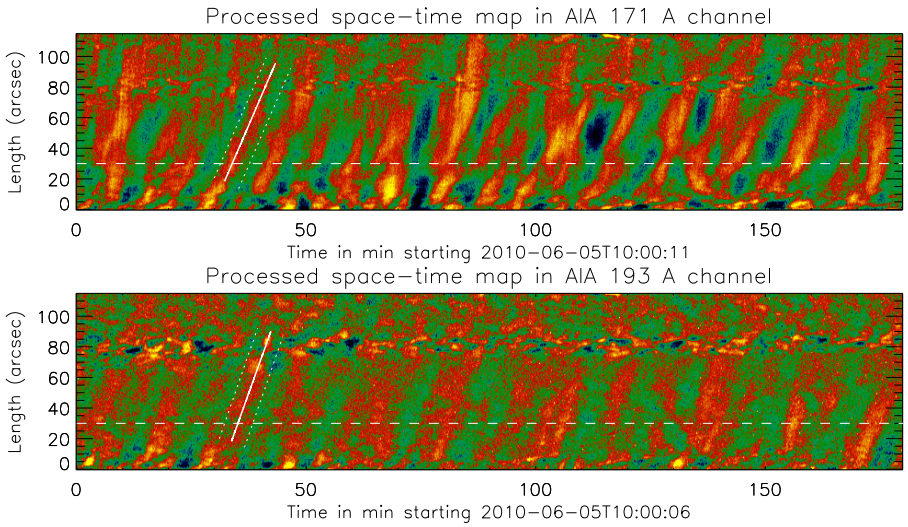

FIGURE 5.7: Processed space-time maps in 171 Å (top) and 193 Å (bottom) channels of AIA constructed from the loop region bounded by dashed curves in Figure 5.5. The dashed horizontal line marks the centre of 3 adjacent rows used in the wavelet analysis for periodicity estimation. The slanted dotted lines in each of these plots, bound the strip considered to identify peaks in propagation speed estimation. Solid line in the centre traces the peak positions obtained from the linear fit, the slope of which gives the propagation speed value.

was constructed from the original space-time map by averaging over three rows centred at the row marked by the horizontal dashed line in Figure 5.7. This is 30″ above the foot point of the loop and is arbitrarily chosen. Wavelet analysis results for these light curves in both the AIA channels are shown in Figure 5.8. A period peaking at 8.6 min in both channels was found which is close to the ≈9 min period observed at EIS pixel location showing longer periods. Also the disturbances in the space-time maps can be clearly seen up to the end of the chosen loop portion. So, it is more likely that these are one and the same. The apparent propagation speed of these disturbances can be measured from the slope of slanted ridges in the space-time maps. This is done by following the method described below.

Propagation Speed Estimation:

Any periodic propagating disturbance will appear as alternating ridges of brightness with finite slope, in a space-time map. The amplitude of the disturbance is normally low and it requires some processing to remove the background and enhance the visibility of these ridges. The slope of these ridges gives the apparent

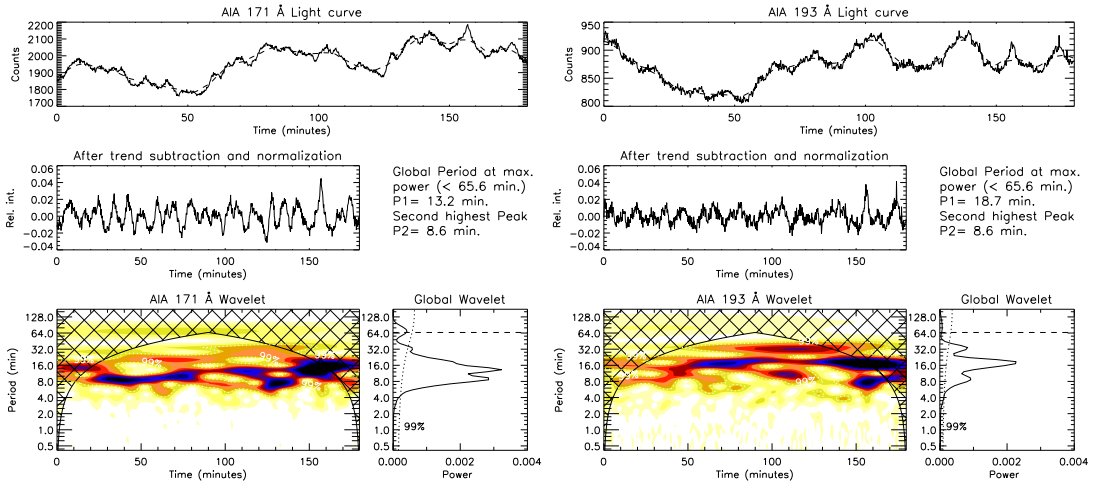

FIGURE 5.8: Wavelet results for the light curves from 171 Å and 193 Å channels of AIA. These are generated from an arbitrarily chosen pixel location which is 30″ far from the foot point of the loop bounded by the dashed curves shown in Figure 5.5. The light curves in the middle panels are made by detrending and normalizing the originals (top panels) with a 55 point (11 min) running average. Overplotted dashed line in each top panel shows this running average. Description of individual panels can be found in text.

propagation speed. This is one of the important observational parameters that help to understand the nature of the detected oscillations. For instance, the temperature dependence of the speed indicates the acoustic nature of the observed oscillations. But to establish this, the measurements of speed should be considerably precise, in at least two different channels representing different temperature plasma. The traditional way to calculate the speed is to manually select two points on one of the clean ridges, connect them with a straight line and find the slope of that line. This roughly gives the propagation speed, but the error in this estimation is very high. An attempt has been made here to reduce this error, by following a more rigorous method. First, a clean ridge was extracted from the space-time map, (processed to display the alternate ridges) by choosing a strip roughly parallel to it and sufficiently wide to only include that particular ridge. The dashed lines in each panel of the Figure 5.7 enclose such strips. Then the positions of the local maxima were found at each spatial location along the strip. These positions were then converted back to the actual positions in the space-time map using co-ordinate transformations. Ideally, for a clean oscillatory disturbance propagating with constant speed, these positions should fall on a straight line in the space-time map, and the slope of that line gives the propagation speed with no error. But the presence of some background structures, lower amplitudes, and/or

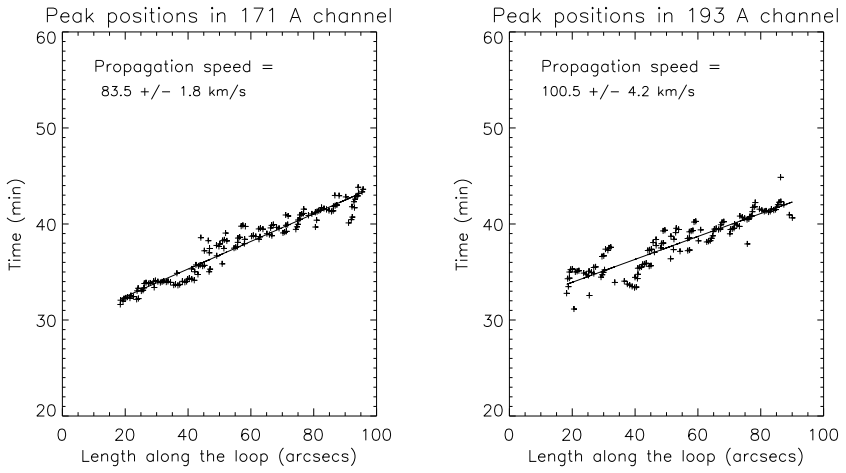

FIGURE 5.9: Results of the propagation speed analysis in AIA 171 Å and 193 Å channels. In each plot '+' marks denote the observed positions of the peaks along the strip bounded by dotted lines in Figure 5.7. The overplotted solid line is the linear fit. The inverse slope of this line gives the propagation speed. Estimated propagation speeds are written in respective panels.

multiple periodicities can affect these positions and deviate them significantly. Nevertheless, most of them fall on a straight line. Figure 5.9 displays the observed positions of the peaks along the chosen strips in 171 Å and 193 Å channels which are denoted by '+' symbols. The overplotted solid line in each plot, is the linear fit. The positions derived from this linear fit are marked by a continuous line on the chosen strip in Figure 5.7. The slope of this line gives the propagation speed. The propagation speeds thus measured are 83.5 $\pm$ 1.8 km s^{-1} in 171 Å and 100.5 $\pm$ 4.2 km s^{-1} in 193 Å channels. Error values in these estimations are calculated from 1-σ errors in the linear fit. Propagation speeds calculated with this method are more reliable with considerably small errors. Since the peaks are identified from the local maxima, this method requires a clean continuous ridge with good contrast between the peak values and the background, in other words amplitudes should be sufficiently large. Note the propagation speeds in both channels are calculated from the same but single disturbance. It may better to compare the speeds for more than one propagating disturbance, but it is very hard to find a clean continuous ridge of sufficient length, in this dataset, simultaneously in both channels. Particularly in the 193 Å channel the amplitudes were small and the ridges were mostly bad making our attempts futile.

Tomczyk and McIntosh (2009) used a similar method to calculate the propagation

speeds using the time lag at different positions along the ridge obtained from the cross-correlation between the time series. The accuracy in their measurement is also similar to that obtained in the current method. However, the correlation may not be good all the time if we consider the full time series and the additional advantage in this method by isolating individual ridges is that any change in speed in the successive disturbances because of some additional events can also be explored and compared.

5.3.2.2 Short period oscillations

Studying high frequency oscillations was one of the principal aims of this observation for which the sit-and-stare observations were made at high cadence (≈6 s). Due to telemetry restrictions, the observations were limited to five spectral windows and out of them two, namely, Fe XII 195.12 Å and Fe XIII 202.04 Å are used in the current investigation. As mentioned in the previous section, there were three sets of scans in sit-and-stare mode at the location marked by the vertical line in Figures 5.4 and 5.5. The third set of these shows significant oscillation at a pixel location marked by the bottom cut in Figure 5.5. Light curves in intensity, velocity and line width were generated at this pixel location in the two EIS lines. A square region similar to that explained in the previous section had been chosen from each AIA channel and co-temporal light curves were constructed from intensity averaged over this region.

Wavelet analysis was done to find the significant periodicities present in these light curves. The results for the light curves in intensity, Doppler shift and line width from EIS Fe XII 195.12 Å line and in intensity from AIA 193 Å channel are shown in Figure 5.10. Each light curve from EIS was smoothed over two temporal points before proceeding for wavelet analysis which removes any variations shorter than ≈12 s. No smoothing was done for those from AIA. A running average constructed by smoothing over 40 points (≈4 min) in EIS and equivalent in AIA (20 points) is subtracted from the light curves to filter the longer periods. The detrended light curves which were used in the wavelet analysis are shown in the middle panels of each plot. In case of intensity, the resultant light curves were also normalized with

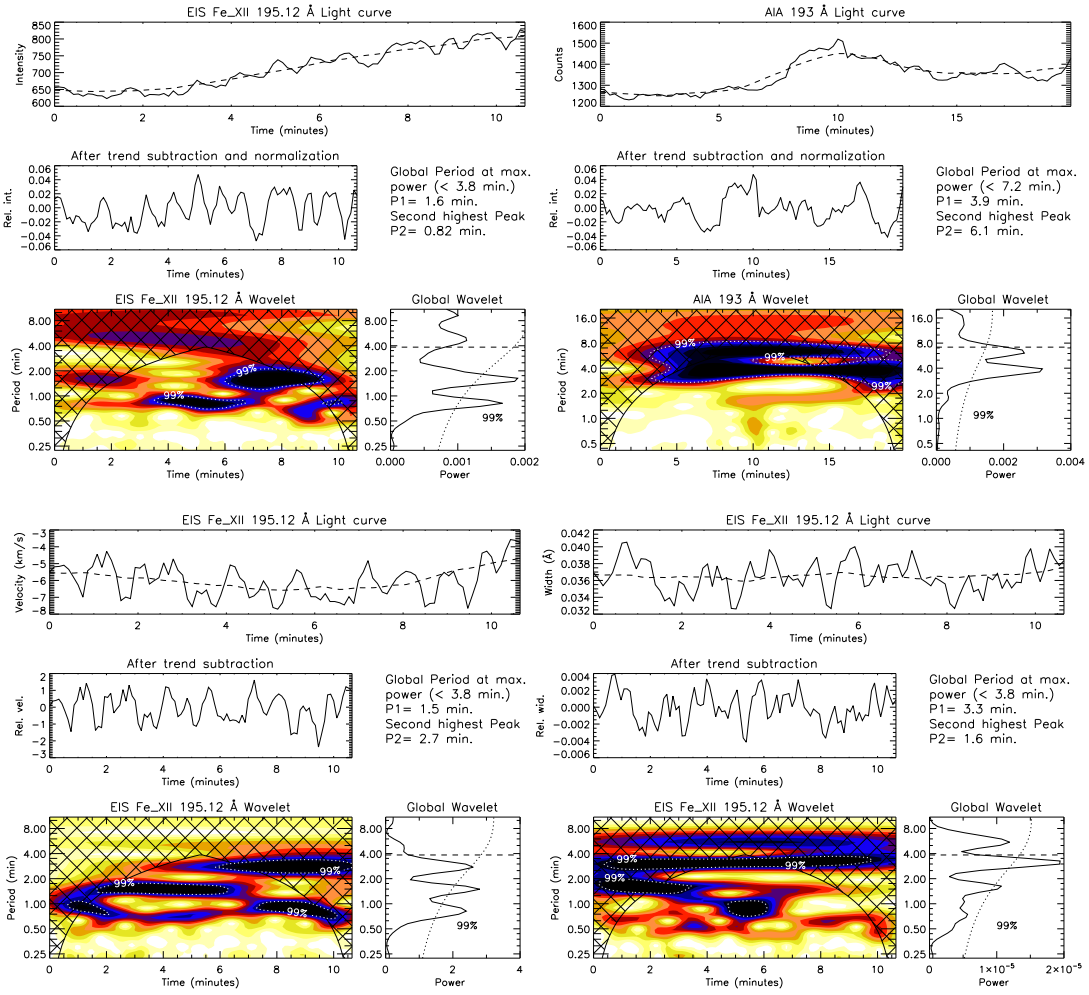

FIGURE 5.10: Results of wavelet analysis for the light curves generated from the bottom cut location (solar-$Y \approx$ -250″) in Figure 5.5. These plots are for intensity, velocity, and line width in Fe XII 195.12 Å EIS line and intensity in 193 Å channel of AIA (see the corresponding labels). Values of the top two strongest periods are listed as P1 and P2 in the text adjacent to the middle panels. See text for the description of individual panels and other details.

the subtracted trend. Oscillations with periodicity ≈1.6 min (see Figure 5.10) were found in all the three line parameters intensity, velocity, and line width with 99% confidence. Analysis using other EIS line Fe XIII 202.04 Å shows similar periodicity peaking at 1.2 min in all the three line parameters. Corresponding results from AIA 193 Å channel show two periods peaking at 3.9 min and 6.1 min. The period at 6.1 min has a larger power and hence was not eliminated completely, though its power was reduced due to 4 min filtering. A peak at ≈1.7 min can also be seen, but it is not significant. In 171 Å channel two peaks were seen at 4.7 min and 2.0 min, of which, again the latter is below the confidence level.

TABLE 5.2: Top two strongest periods above the 99% significance level obtained from wavelet analysis. Results from the two AIA channels and the two EIS lines at both locations marked by horizontal cuts in Figure 5.5 are listed. Values in brackets correspond to the secondary peaks.

Solar-Y	Emission line/ Channel	Intensity	Velocity	Line width
-226″	Fe XII 195.12 Å	9.2 (1.8)	8.5 (4.6)	4.2 (5.5)
	Fe XIII 202.04 Å	7.1 (2.1)	6.0 (3.3)	3.9 (10.1)
	AIA 171 Å	9.4 (4.7*)	—	—
	AIA 193 Å	10.2 (4.7*)	—	—
-250″	Fe XII 195.12 Å	1.6 (0.82)	1.5 (2.7)	3.3 (1.6)
	Fe XIII 202.04 Å	1.2 (0.82)	1.4 (2.3)	2.7 (1.2)
	AIA 171 Å	4.7 (2.0*)	—	—
	AIA 193 Å	3.9 (6.1)	—	—

* Not above the 99% significance level.

5.3.3 Results and Discussion

A portion of EIS slit crossing the AR fan loop system was studied in search of oscillations and two locations were identified with significant oscillatory behaviour. Table 5.2 summarizes the different periods observed at these two locations. The top two strongest periods with 99% confidence from the wavelet analysis were listed. Values that are not significant are marked with (*).

Long period oscillations were observed at the location corresponding to solar-$Y \approx$ -226″. Results from EIS Fe XII 195.12 line show a periodicity around 9 min in both intensity and velocity, but not in line width. Intensities from both 171 Å and 193 Å channels of AIA, also show this periodicity. Space-time analysis over a loop crossing this region shows propagating disturbances with periodicity 8.6 min in both the AIA channels confirming that the oscillations seen in EIS are due to these PDs. However, the hotter EIS line (Fe XIII 202.04) shows different peaks ranging from 6 min to 10 min (see Table 5.2) in intensity, velocity and line width which may or may not be related to this. Mean line profiles were constructed at this location and are shown in Figure 5.11 for both the EIS lines. These profiles were constructed by averaging over all the three sit-and-stare sets. Single Gaussian fits, along with a polynomial background, to these profiles are overplotted as solid lines. There is no apparent blue shifted component (deviation from the single Gaussian fit) visible

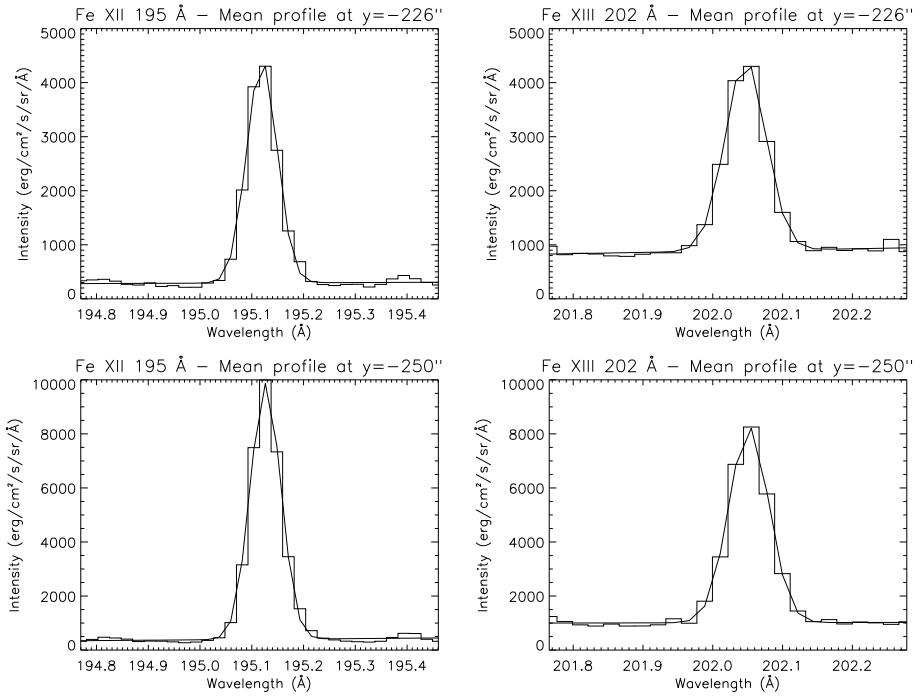

FIGURE 5.11: Line profiles averaged over time of the sit-and-stare observation, taken in EIS spectral lines, Fe XII 195.12 Å and Fe XIII 202.04 Å using 1″ slit. Panels in the top row correspond to the top cut location and that in the bottom row correspond to the bottom cut location in Figure 5.5. In each of these panels, overplotted solid line is the single Gaussian fit obtained considering a polynomial background.

from these profiles. The projected propagation speeds were calculated using an improvised technique to minimise errors in the estimation. The speeds were found to be 83.5±1.8 km s^{-1} and 100.5±4.2 km s^{-1} respectively, in 171 Å and 193 Å channels. These values are significantly lower than the theoretical acoustic speeds, 136 km s^{-1} and 170 km s^{-1} computed from the peak temperatures 0.8 MK and 1.25 MK respectively, in these channels. The ratio of the observed speeds is 1.20 compared to the theoretical acoustic speed ratio 1.25. Oscillations only in intensity and velocity with no corresponding peak in line width and no visible blue-shifted emission in the line profiles, accompanied by higher propagation speeds in hotter channels, suggest that the observed PDs are possibly due to slow magneto-acoustic waves rather than periodic upflows. It can also be seen that the amplitudes are lower in the hotter 193 Å channel (see Figure 5.8). This is consistent with the damping in a multi-thermal loop due to thermal conduction and may further support the nature of these oscillations as of slow magneto-acoustic type. However, there was no clear correlation observed between intensity and Doppler shift which

is expected in case of propagating slow waves. Although they go in phase at a few locations, overall the correlation seems to be poor. It is possible that the presence of higher frequencies, which do not have correlated variations in Doppler shift, is spoiling the overall correlation. Figure 5.8 also show a period at ≈18 min along with the ≈9 min period, in both channels. It is not so clear in the 171 Å channel because of the 11 min filtering, but it can be clearly seen by filtering periods longer than 20 min. This may suggest the presence of harmonics in the propagating disturbances, similar to those observed by Wang *et al.* (2009b) who report 12 min and 25 min periods in the active region fan loops.

Short period oscillations were observed at the pixel location corresponding to solar-$Y \approx$ -250″. Results from EIS in Fe XII 195.12 Å and Fe XIII 202.04 Å lines show a periodicity peaking at ≈ 1.6 min and ≈ 1.2 min, respectively, in all the three line parameters. Similar periodicities were also seen from AIA, but they are not significant in either of the channels. This might be due to the wider passbands of AIA filters (compared to the narrow spectral lines of EIS) covering a larger temperature range, which allows more background in the line of sight and may result in reduction of the relative oscillation amplitudes. This can cause problem in detecting, particularly, short period oscillations whose amplitudes are normally less. Presence of significant oscillations in all the three line parameters, intensity, velocity and line width makes it difficult to point a particular wave mode as the cause. De Pontieu and McIntosh (2010) discussed that a faint blue-shifted emission component in the line profile, caused by quasi-periodic high velocity upflows, can actually cause these small amplitude oscillations, in intensity, velocity and line width when fitted with single Gaussian. Moreover, this particular pixel location is adjacent to a bright structure which is close to the active region core and could possibly be the foot-point of a hotter loop where the chances of upflows are more probable. In fact, there was a small loop system at this location, 1 hour earlier to this observation, which disappeared later leaving this bright structure. Mean line profiles constructed from the time average at this location are shown in Figure 5.11 (bottom row) for both EIS lines. Since analysis at this location is only on the third set in sit-and-stare mode time average was restricted to this. The solid lines are the single Gaussian fits to the profiles considering a polynomial background. Presence of any additional periodic component should be visible in this profile, although averaging can reduce its amplitude. It can be clearly seen from this figure that

there is no enhancement in the blue wing of the profile and a single Gaussian fit is a very good approximation. Individual line profiles were also seen at several time steps, but no visible blue shifted component was found in any of them. So, the possible explanation of these oscillations in terms of quasi-periodic upflows may be ruled out. However, there can be continuous upflows in the background. Doppler shift values (see Figure 5.10) indicate that the line of sight speeds of such flows at this location are less than 10 km s^{-1}. Singh *et al.* (2011) found oscillations of very short periods (25 s to 50 s), from eclipse observations, in all the three line parameters and discussed this behaviour as due to possible coupling of more than one wave mode. Also in our observation, a period at ≈3 min was found only in velocity and line width and another period at ≈0.8 min significant only in intensity and velocity. So, it is quite possible that the oscillations observed here are due to coupling of various MHD modes at this location. The relative amplitude of these oscillations was found to be higher in Fe XIII 202.04 line than that in Fe XII 195.12 line in all the line parameters. It is difficult to explain this behaviour, since the oscillations at this location do not correspond to a particular mode.

Chapter 6

Damping in propagating disturbances

Quasi-periodic propagating disturbances are regularly observed in extended loop structures of active regions and polar plume/interplume regions. The properties of these disturbances observed in these two regions are almost same with the only difference being the relatively shorter periods observed in active region fan loops. A vast amount of observational and theoretical studies on these PDs made it possible to utilise them for seismological applications. However, as mentioned in the previous chapter, the recently realized ambiguity of distinguishing them from high speed quasi-periodic upflows kept these applications at stake. It is important to study different properties of these PDs in detail to get a better insight into their exact nature. One of the interesting properties of PDs is that they tend to disappear after travelling a certain distance along the supporting structure. Their amplitudes rapidly decay down, pushing them beyond detection within a short distance. The observed damping in different open structures was studied in detail along with other properties which suggest the PDs are more likely due to slow MHD waves rather than periodic upflows. A qualitative comparison with a simple slow wave model indicates thermal conduction as the damping mechanism. The details of this study[1] are discussed in this chapter.

[1]Results of this work are published in Krishna Prasad *et al.* (2012b)

6.1 Introduction

Small-amplitude propagating intensity disturbances were studied by several authors both in active region fan loops (Berghmans and Clette 1999; De Moortel *et al.* 2000; King *et al.* 2003) and in polar plumes (Deforest and Gurman 1998; McIntosh *et al.* 2010; Krishna Prasad *et al.* 2011). Majority of the studies are based on imaging alone where the PDs are usually identified as alternating slanted ridges in the space-time maps. Based on the general observed properties such as periodicities and propagation speeds (see De Moortel 2009, and references therein), these PDs were thought to be signatures of slow magneto-acoustic waves due to leakage of photospheric p-modes (De Pontieu *et al.* 2004, 2005). Their contribution to the coronal heating and the acceleration of the solar wind has been worked out by several authors (De Moortel *et al.* 2000; McEwan and De Moortel 2006; Deforest and Gurman 1998; O'Shea *et al.* 2007) assuming them to be slow waves. They were used for seismological applications as well (Wang *et al.* 2009b). But, as mentioned in Chapter 5, the recent spectroscopic studies on these PDs reveal periodically enhanced emission in blue wings, which is indicative of quasi-periodic upflows (De Pontieu and McIntosh 2010; Tian *et al.* 2011). It is also argued that a quasi-static plasma component in the line of sight may induce the slow waves to produce similar spectral signatures (Verwichte *et al.* 2010). This makes the general nature of these disturbances somewhat ambiguous and puts their applicability in question. It is worth exploring different properties of these PDs, in order to get a better understanding on their real nature. Spatial damping is one of the interesting properties observed in PDs. Their amplitudes were found to decrease rapidly as they travel along the supporting structure. Assuming them to be slow magneto-acoustic waves, thermal conduction, compressive viscosity, optically thin radiation, and area divergence, were proposed to be some of the causes for the decay in their amplitude. Efforts were also made to theoretically model the observed decay using some of these processes (De Moortel and Hood 2003, 2004). In this context, the damping observed in different open structures is explored in detail to find the true nature of PDs. This will further supplement the other properties of PDs discussed in Chapter 5.

6.2 Observations

A three-hour-long imaging sequence taken by the Atmospheric Imaging Assembly[2] (AIA; Lemen *et al.* 2012) onboard SDO, on June 5, 2010 starting from 10:00:11 UT, was used in this analysis. Two different coronal channels centred at 171 Å, and 193 Å, with their peak temperature responses at 0.8 MK, and 1.25 MK, respectively were chosen. Images at level 1.0[3] were already subjected to basic corrections that involve removal of dark current, de-spiking, flat-fielding, and bad-pixel removal. These were then processed to coalign all images in different channels to a common centre, to correct the roll angles, and to rescale the images to a common plate scale using the `aia_prep.pro` routine (version 4.10), available in Solar SoftWare (SSW). The final pixel scale is $\approx 0.6''$ and the cadence of the data is 12 s.

Three different open-loop structures, one isolated on-disk plume-like structure, a set of fan loops extending off-limb, and plume/interplume structures above the north pole of the sun were chosen in this study. Square subfield regions of dimensions 350, 600, and 700 pixel units, respectively, were considered to cover these three target regions. In both channels, images corresponding to the on-disk region were tracked for solar rotation and then coaligned using the intensity cross-correlation, taking the first image as reference. Images in the off-limb locations were coaligned directly because it was not possible to correct for solar rotation.

6.3 Analysis and results

Regular space-time analysis and movies indicate propagating disturbances in all the three regions chosen. Multiple periodicities were often observed in these disturbances (see Figures 5.3, 5.8, & 5.10 in the previous chapter). To study their behaviour at different frequencies, powermaps for each of the selected regions were constructed following the procedure described below.

[2]Description of the instrument is given at Section 2.1.1.1
[3]Different levels are explained in Section 2.2.1

The time series at each pixel was subjected to wavelet analysis to determine the distribution of power at different frequencies. Keeping the total length of the time series (3 hrs) in mind, periods longer than 30 min were eliminated by detrending the time series with a 150 point ($\approx$ 30 min) smoothed average before performing the wavelet analysis. Frequencies with power above the 99% confidence level were chosen to be significant for a white noise process (Torrence and Compo 1998). Three different periodicity ranges, henceforth referred to as short (2 min – 5 min), intermediate (5 min – 12 min), and long (12 min – 25 min) were selected. Power maps corresponding to these three ranges were produced by adding the total significant power within the periodicity limits at each pixel location. Figure 6.1 displays these powermaps for the off-limb loop structure in 171 Å and 193 Å channels of AIA. The original intensity image is shown in the top left panels. Interestingly, the extent of the loop structures visible is increasing from shorter to longer periods which implies that the power in longer periods is significant up to larger distances along the loop. In other words, this could mean that the longer periods travel farther compared to the shorter ones, which might have got damped faster. This trend is observed in both channels. This is true even for the other two structures, the on-disk plume-like structure and the north polar plume/interplume structures. Powermaps for these regions are shown in Figure 6.2. Another interesting feature observed in these maps is the omnipresence of longer periods. Very few observations (Wang *et al.* 2009b) showed periods longer than 10 min to be present in active region loops. These results indicate the ubiquitous presence of longer periods and seems to wipe out the differences in PDs observed at polar regions and active region loops.

Further analysis is done on the on-disk plume structure to extract other properties. Space-time maps were constructed by tracing a part of the loop structure and were processed to enhance the visibility of the alternating ridges. Figure 6.3 shows the location of the loop on a snapshot displaying the plume like structure along with the processed space-time maps in two AIA channels. The processing was performed by subtracting a background trend constructed from a 55 point ($\approx$ 11 min) smooth average of the original and then dividing by it. The trend subtraction removes or suppresses periods longer than 11 min, and division by the trend compensates for the intensity fall along the loop. PDs can be clearly seen in both channels. The apparent propagation speed was measured at three clean ridges

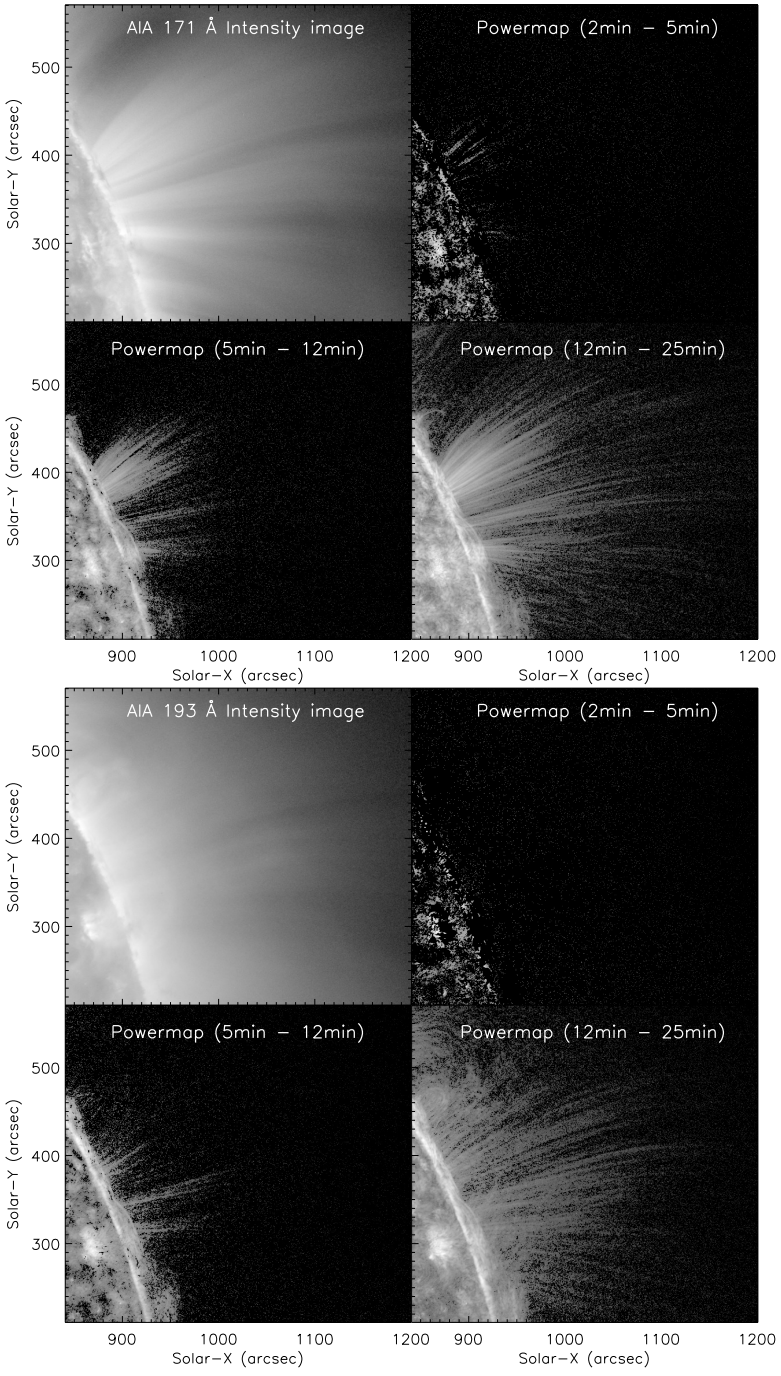

FIGURE 6.1: Powermaps in different periodicity ranges for the off-limb loop structure in 171 Å (top) and 193 Å (bottom) channels of AIA. The intensity image is shown in the top left panels. All powermaps show the total power above the 99% confidence level in the periodicity limits.

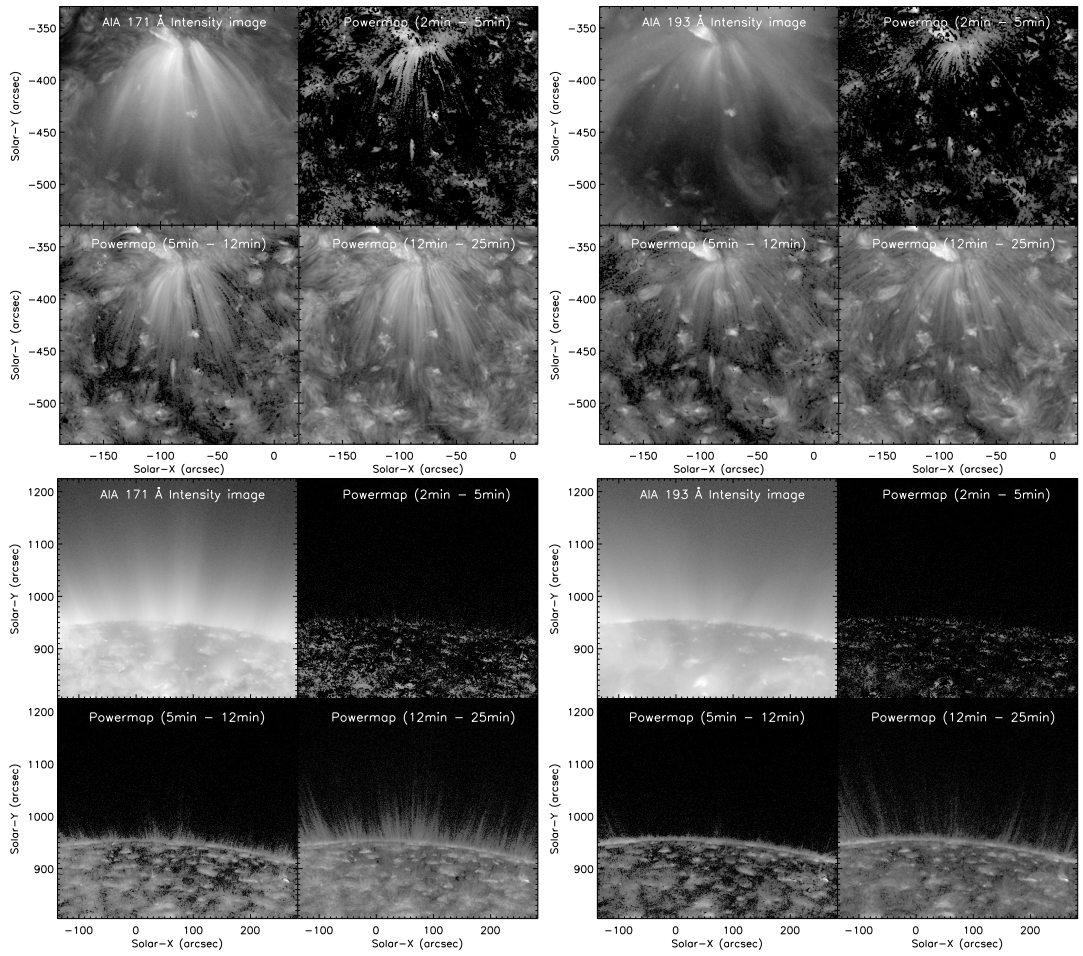

FIGURE 6.2: *Top row:* Powermaps constructed in different periodicity ranges for the on-disk plume structure in 171 Å (left) and 193 Å (right) channels of AIA. The intensity image is shown in the top left panels. All powermaps show the total significant power above the 99% confidence level in the periodicity limits. *Bottom row:* Same, but for the north polar region

following the method described in Krishna Prasad *et al.* (2012a). This method involves identifying the peak positions in time from the space-time map at each spatial location along the ridge and then fitting them linearly. The peak positions were identified from the locations of maxima within a strip wide enough to cover the ridge alone. The apparent propagation speed and the error in its estimation could then be derived from the slope of the fit and the goodness of the fit. The boundaries of the chosen strips and the final fitted peak positions are shown as dotted and solid lines along the ridge, respectively, in the space-time maps shown in Figure 6.3. Unlike the case of choosing two points manually on each ridge, this method takes several points along the ridge and uses the peak positions in the speed estimation and hence improves the error in it (see Section 5.3.2.1 for

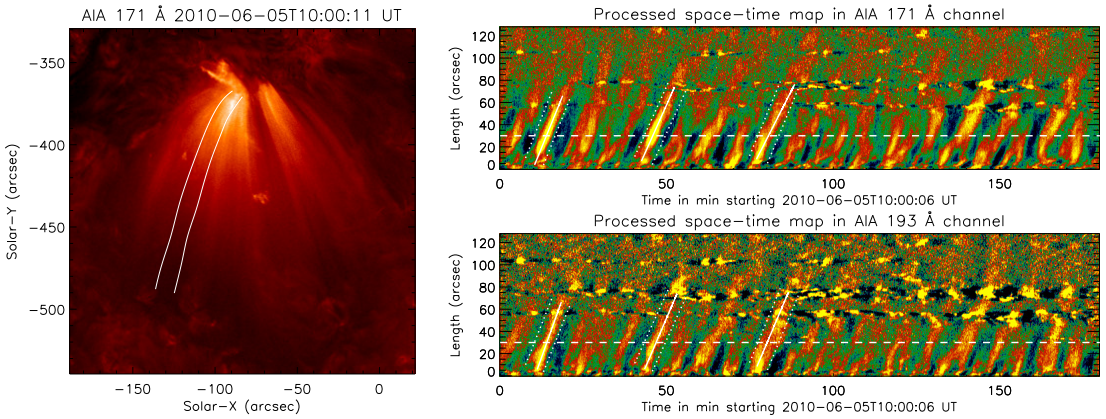

FIGURE 6.3: *Left:* Snapshot displaying the on-disk plume-like structure. The white lines overplotted bound the chosen loop location. *Right:* Processed space-time maps constructed from this loop portion in 171 Å (top) and 193 Å (bottom) channels. Apparent propagation speeds were estimated from the slopes of the slanted solid lines overplotted. The horizontal dashed lines in each panel mark the location of the row used in the wavelet analysis for periodicity estimation.

TABLE 6.1: Periodicity and propagation speeds in different AIA channels. Second-strongest periods are listed in brackets.

Channel (Å)	Periodicity (min)	Apparent speed (km s^{-1})		
		Ridge1	Ridge2	Ridge3
171	9.4 (15.7)	88.7±9.7	80.5±5.7	70.6±5.8
193	9.4 (15.7)	100.8±6.4	84.0±8.6	85.0±13.3

more details). Recently, Kiddie *et al.* (2012) used a similar method to determine the speeds of such propagating disturbances and discussed their temperature dependence. Yuan and Nakariakov (2012) also developed three different methods for measuring the apparent speed of propagating waves with considerably high accuracy. Apparent propagation speeds obtained from the two AIA channels are listed in Table 6.1. Same ridges are chosen in both channels for comparison. The observed apparent propagation speed is consistently higher for all three ridges in the hotter 193 Å channel. To estimate periodicity, wavelet analysis was performed at an arbitrarily chosen row marked by the horizontal dashed line in space-time maps. Wavelet plots at this location for both 171 Å and 193 Å channels are shown in Figure 6.4. Top two significant periods obtained from this analysis are labelled as P1 and P2 at the middle right portion of these plots. These periodicity values are also listed in Table 6.1. The periodicity of these disturbances was found to be 9.4 min. In the table, the values listed in brackets are the second-strongest peaks.

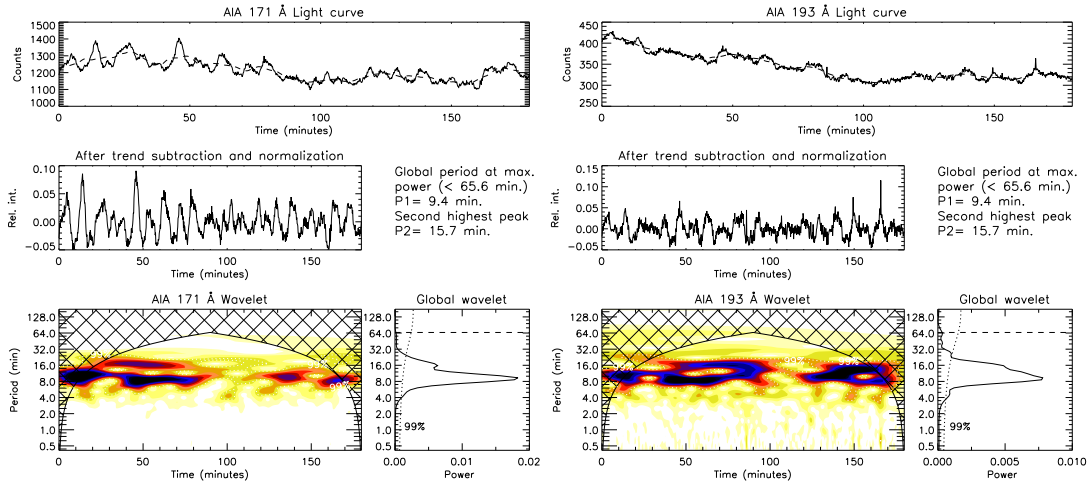

FIGURE 6.4: Wavelet plots for the time series from a row marked by the dashed line in Figure 6.3 for 171 Å (left) and 193 Å channels. In each of these figures top panels show the original light curve in solid line and the subtracted trend in dashed line. The middle panels display the trend subtracted and normalized light curves. The main wavelet plot and the global wavelet plot are shown in the bottom left and bottom right panels. Overplotted dotted line in the global wavelet plot represents the 99% confidence level. Top two significant periods are listed as P1 and P2 in the middle right portion.

Note the presence of the longer periods despite the 11 min filtering. They are only suppressed but not completely eliminated.

Spatial damping can be clearly seen in the space-time maps (see Figure 6.3). The disturbances were not clearly visible after certain distance. This seems to have happened at a relatively shorter distance for 193 Å channel. To study this quantitatively, intensity variation along the loop was constructed relative to the background by averaging over three successive time frames. This spatial variation is shown as solid grey lines in Figure 6.5 for both the channels. Overplotted plus symbols in blue are the 10 point ($\approx$ 4.3 Mm) smooth average values. A damping sine wave function given by

$$I(l) = A_0 \sin(\omega l + \phi) \exp(-l/L_d) + B_0 + B_1 l \tag{6.1}$$

was fitted to these values, which is also overplotted as a solid line in red. Here A_0 is the amplitude of the sine wave, l is the length along the loop, ω and ϕ are frequency and phase of the wave, and L_d represents the damping length. The last two terms were used to fit the background trend, if present. The first-order fit is

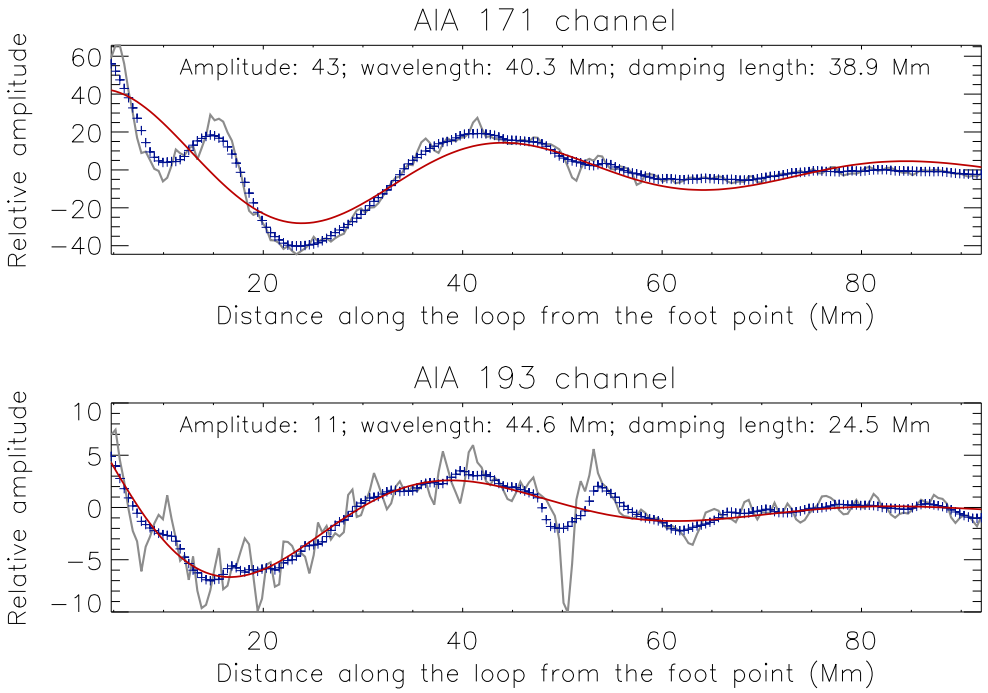

FIGURE 6.5: *Top:* Solid line in grey represents the intensity values along the loop relative to the background, averaged over three successive time frames in 171 Å channel. Plus symbols in blue are the 10 point ($\approx$ 4.3 Mm) smooth averages of these values. The damping sine curve fitted to these smoothed values is overplotted as a red solid line. Obtained fit parameters are labelled. *Bottom:* Similar curves and values generated from the 193 Å channel.

found to be more than sufficient for this purpose. The best fits were obtained using a Levenberg-Marquardt least-squares minimisation (Bevington 1969). Obtained fit parameters are labelled in the respective panels. Clearly, the relative amplitude of the oscillation and the damping length (L_d value in equation 6.1) are lower and the wavelength is slightly longer in the hotter 193 Å channel. The damping lengths are 38.9 Mm and 24.5 Mm in 171 Å and 193 Å channels respectively. The lower damping length indicate faster damping in the 193 Å channel. Now let us try to understand these observed properties using a simple slow wave model.

6.4 Slow-wave model

The farther propagation of the lower frequencies and the stronger dissipation in hotter channels may be understood as an effect of the damping of slow magneto-sonic waves due to thermal conduction. Let us consider a simple 1-D model (De Moortel and Hood 2003; Owen *et al.* 2009), where radial structuring has been neglected. More complicated models have been studied by Soler *et al.* (2008). The dispersion relation of slow waves in such a simple configuration is given by

$$\omega^3 - \imath\gamma d c_{\rm s}^2 k^2 \omega^2 - \omega k^2 c_{\rm s}^2 + \imath d k^4 c_{\rm s}^4 = 0, \tag{6.2}$$

where ω is the angular wave frequency, k is the wave number, γ is the ratio of specific heats and $c_{\rm s}$ is the sound speed. The parameter $d = \frac{(\gamma-1)\kappa_{\parallel} T_0}{\gamma c_{\rm s}^2 p_0}$ expresses the importance of the thermal conduction. It has the dimension of time. The quantities p_0 and T_0 are the background pressure and temperature, respectively. $\kappa_{\parallel} = \kappa_0 T_0^{5/2}$ is the thermal conduction coefficient. Low d means a weak thermal conduction, high d corresponds to strong thermal conduction. Since the observed waves are presumably driven from near the foot points of the loop, the frequency ω was considered to be fixed by the driver, and solved the dispersion equation for the wave number k. For the vanishing thermal conduction ($d\omega = 0$), it was found $k^2 = \omega^2/c_{\rm s}^2$, which corresponds to the sound wave solution. In the limit of weak thermal conduction ($d\omega \ll 1$), the solution may be found as

$$k = \frac{\omega}{c_{\rm s}}\left(1 - \imath\frac{d\omega}{2}(\gamma - 1)\right) = \frac{\omega}{c_{\rm s}} - \imath\frac{1}{L_{\rm cond}}, \tag{6.3}$$

where the thermal conduction damping length was defined as $L_{\rm cond}$. This formula is only marginally applicable in the solar corona, since the thermal conduction in coronal loops is quite strong (Van Doorsselaere *et al.* 2011). For instance, the results from Van Doorsselaere *et al.* (2011) indicate $d\omega \approx 0.7$ which is less than 1 but not very low. However, a lot of the physics relevant for these observations may be understood from this asymptotic formula.

Let us first consider the effect of temperature. When the temperature increases (i.e. when the structures were observed in a higher temperature passband), the

thermal conduction coefficient $\kappa_{\parallel}$ increases as well. This results in a higher value for d, and thus a lower value for the damping length $L_{\rm cond}$ in the limiting case of weak thermal conduction ($d\omega \ll 1$) that is currently considered. As found in the observations, the slow waves are more heavily damped in higher temperature passbands. Now, let us consider the frequency dependence of the damping. In Equation 6.3, it was defined $L_{\rm cond} = 2c_{\rm s}/d\omega^2(\gamma - 1)$, where it is now obvious that the damping length is inversely proportional to the frequency squared, or directly proportional to the period squared. Indeed, in the observations it was found that the longer periods propagate much higher (longer damping lengths). This simple model explains the qualitative features of the observations quite well. This model could be tested by measuring the damping lengths for different frequency bands, and verifying whether a power law with slope 2 is found.

6.5 Conclusions

Three different open loop structures both off-limb and on-disk, were chosen to study the damping in propagating disturbances. By constructing powermaps in three period ranges it was found that the longer periods travel farther distances along the supporting structure which might mean faster damping in shorter periods. Omnipresence of longer periods was also observed from these powermaps. The apparent speeds obtained for the propagating disturbance in the on-disk plume structure are consistently higher in the hotter (193 Å) channel. Quantitative analysis on the spatial damping along the loop indicate relatively lower amplitudes and shorter damping lengths in this channel. The damping lengths were found to be 38.9 Mm and 24.5 Mm in 171 Å and 193 Å channels, respectively. All these properties, the further propagation of longer periods, the higher propagation speeds, lower amplitudes, and faster damping observed in the hotter channel, can be very well explained using a simple slow wave model considering thermal conduction as the damping mechanism. It is difficult to understand these properties, particularly the frequency dependent damping, if the PDs were due to periodic upflows. So it is more likely that the observed PDs are signatures of slow magneto-acoustic waves rather than due to high speed quasi-periodic upflows.

Chapter 7

Conclusions & Future Work

Solar corona, the tenuous outer atmosphere of the Sun, is very hot with temperatures of the order of a few million kelvin. With its extreme conditions, it serves as a unique physical laboratory to improve our understanding on various branches of physics (for *e.g.,* plasma physics). The energy source for maintaining the corona at such high temperatures is not clearly known yet and is called coronal heating problem. This is one of the major problems in astrophysics and appears as a common motivation for majority of the coronal studies. The advent of new instruments with increasing spatial, temporal and spectral resolutions, is advancing our knowledge on corona while at the same time puzzling us with more and more new problems. The main aim of this thesis is to solve or improve our understanding on a few such issues using imaging and spectroscopic data from instruments both ground- and space-based.

Broadly, two different studies were performed to study coronal structures using data from a ground-based coronagraph, a space-based EUV imager, and a space-based EUV spectrometer. One of them is connected with the variation of spectral line parameters and the other is related to the nature of propagating intensity disturbances. Some of the important results obtained from these studies are given in this chapter along with the future directions to pursue them further.

7.1 Major Results

The thermal structure of a coronal loop is crucial for determining the plasma heating mechanism and other important properties. One of the earliest theoretical models of a coronal loop was proposed by Rosner *et al.* (1978) who predicted that the temperature in a uniformly heated hydrostatic loop increases towards its apex. This model is widely known as RTV model named after the authors, Rosner, Tucker, and Vaiana. Although the initial observations were in good agreement with this, later observations in Extreme Ultra-Violet (EUV) wavelengths show almost no variation in temperature along the coronal segment of a loop. Different theories, superposition of several thin strands, non-uniform heating, non-static loops with significant flows inside, non-uniform cross-section of a loop, etc., were proposed to explain this behaviour. A few other studies disagree on the observed isothermal nature itself. In an attempt to determine the general temperature variation in a loop along its length, high resolution spectroscopic observations from a ground based coronagraph were used. These observations were taken simultaneously in multiple emission lines, on 4 different days. The temperature variation along 18 different loop structures observed on these days, was studied using temperature sensitive emission line ratios. It was found that the structures observed in colder lines ([Fe XI] 7892 Å and [Fe X] 6374 Å lines) show a positive gradient whereas that observed in relatively hotter lines ([Fe XIV] 5303 Å and [Fe XIII] 10747 Å lines) show a significant negative gradient in temperature. The positive gradients fit into the regular uniform heating model while the unusual negative gradients can be explained by considering non-uniform heating. However, the observed variation seems to general for a majority of the loops, which surprisingly indicates that the loop tops appear cooler or hotter depending on the line pair chosen. It may not be correct in such case to interpret the results with different loop heating models. A gradual interaction between different temperature plasma was proposed to explain this behaviour. The exact physical process responsible for this gradual interaction remains to be explored.

Singh *et al.* (1999, 2003a) studied the line width variation with height extensively in different spectral lines using data from Norikura coronagraph. They found that in general, the line width of Fe X 6374 Å (red emission line) increases with

height whereas that of Fe XIV 5303 Å (green emission line) decreases with height. Earlier, some authors explained the increase in line width as due to increase in non-thermal velocity because of outward propagating waves and the decrease as due to damping in these waves. A few others discussed the possibility of increase in ion temperature which can be significantly different from the electron temperature due to preferential heating. But this opposite trends observed in same loop with different spectral lines could not be explained with those theories. This was again solved by assuming a gradual interaction between different temperature plasma. However, most of these studies were limited to the equatorial regions and it was not explored whether or not the polar regions show similar behaviour. To explore this, several raster scans that cover mid- and high-latitude regions observed with the same coronagraph, were analysed. Combining these results with that from the equatorial regions, the latitudinal variation was also studied. It was found that variation of line width with height in the polar and mid latitude regions is qualitatively similar to that observed in equatorial regions. The latitudinal variation, however, revealed some thing interesting. The line widths were found to increase towards the poles with higher values in polar regions for all the lines studied except for the green line! The width of the green line does not seem to change. It is generally believed that higher line widths observed in polar regions are due to some non-thermal source that is powering the fast solar wind, but the behaviour of green emission line needs an explanation.

Propagating quasi-periodic disturbances (PDs) were ubiquitously observed in polar plumes by Deforest and Gurman (1998). From the propagation speeds and other observed properties these disturbances were interpreted as due to propagating slow magneto-acoustic waves. But some of the recent studies suggest the possibility of high speed quasi-periodic upflows which can also show similar signatures in intensity. In an attempt to resolve this ambiguity, a similar study was performed using imaging data from AIA onboard SDO in two different temperature channels. Using wider slits along different plume and interplume regions the effect of fainter jets, if any present, was removed. The stronger jets were identified by visual inspection. Despite these measures PDs were observed in all the structures studied with periodicities ranging from 10 – 30 min and more importantly they were found to be insensitive to changes in slit width. This suggests the involvement of a coherent mechanism. The apparent propagation speeds obtained were in the range

of 100 to 170 km s^{-1} and the average speeds are higher in hotter temperature channels indicating their acoustic nature. All these observed properties favour the interpretation of these PDs as slow waves.

Propagating disturbances were also observed in active region fan loops and were studied extensively by several authors. Wang *et al.* (2009b) observed the in phase behaviour of these oscillations in intensity and Doppler shift indicating their magneto-acoustic nature. But later, De Pontieu and McIntosh (2010) found that the line width is also in phase with intensity in addition to the Doppler shift. They also found a blue ward asymmetry in the line profiles which they interpreted as due to high speed quasi-periodic upflows. These studies indicate the importance of spectroscopy in identifying the exact nature of PDs. In an attempt to understand this, active region fan loops in AR 11076 were explored using simultaneous imaging and spectroscopic observations. Two different periodicities, short (<3 min) and long (≈9 min) were observed at two different locations. Shorter periodicities showed oscillations in all the three line parameters but the longer ones did not show in line width. Line profiles at both these locations can be fitted well with a single Gaussian and no asymmetry was observed. The longer periods were also observed in the co-temporal imaging data which show the temperature dependence in their propagation speeds. Based on these observed properties, it was suggested the longer period oscillations could be due to slow waves and the shorter ones could be due to the simultaneous presence of different magnetohydrodynamic (MHD) waves.

One of the major differences between PDs observed in polar plumes and that in active region fan loops is the periodicity. The periodicities observed in AR fan loops are usually shorter. Using powermaps constructed in three period ranges for different open structures, it was shown that the longer periods are omnipresent and the disturbances observed in these two regions are one and the same. These powermaps also revealed an interesting property of these disturbances. The longer periods were found to travel relatively larger distances along the supporting structure. This might mean faster damping in the short period oscillations. Spatial damping was studied in detail along an on-disk plume like structure. It was found

that the PDs have lower amplitudes and shorter damping lengths in hotter channels. A simple 1-D slow wave model was presented taking thermal conduction as the damping mechanism to explain these properties qualitatively. However, an exact relation between the periodicity and the damping length of these oscillations will reveal more information on the damping sources, which needs to be established.

7.2 Future Directions

As demonstrated by the results presented in the previous section, this thesis had significantly improved our knowledge on the problems undertaken. Nevertheless, a few issues still remain and prompt us to carry this work forward. Some of the possible future directions are outlined here for the individual studies.

The general temperature variation along a coronal loop had been studied and it was observed that the temperature gradients appear positive or negative depending on the line pair chosen. A gradual interaction between different temperature plasma was proposed to explain this. However, the exact process responsible for this interaction may be worked out. The inference that different gradients are observed when a loop is seen in different temperature plasma was based on the behaviour of majority of the loops in the independently observed lines. Although it appears safe to assume this, since the observations were selected solely on the basis of good signal-to-noise ratio without any other bias in selecting the loops, it may be useful to find a direct evidence by looking at the same loop in different temperature lines. This can be achieved by using a space-based spectrometer such as EIS, which observes the solar corona in several emission lines simultaneously. Also, this is important in the view of recent studies by Huang *et al.* (2012) & Nuevo *et al.* (2013), who report the evidence of two kinds of loops, the 'up' loops and 'down' loops with positive and negative temperature gradients respectively. They also found that the down loops are ubiquitous in the low-latitude regions. Although their observations are for quiet coronal regions it maybe worthwhile

investigating any possible connection between their 'down' loops and the negative gradient loops observed in our study.

Variation of line width with height was studied for both mid- and high-latitude regions and by comparing with the existing results for the equatorial regions, the latitudinal variation was also investigated. Similar to that observed in most other studies, the line widths were found to be high in polar regions for all the lines except green line. This behaviour of green line is puzzling and needs some attention. It may be possible that the existing notion of 'higher line widths correspond to higher non-thermal velocity' is wrong and the broadening in polar regions is mainly caused by increase in ion temperature through some process (such as preferential heating) that neglects Fe XIV. This, however requires a thorough investigation.

Propagating disturbances were studied in different open structures using several improvised tools and techniques and none of our studies seem to find the effect of upflows. Maybe the effect of flow is more prominent close to the foot points of the supporting structure as indicated by some authors (Nishizuka and Hara 2011; Tian *et al.* 2012). Different properties observed, particularly the frequency dependent damping favours the slow wave interpretation of these PDs. The further propagation of longer periods was explained by considering the damping in slow waves due to thermal conduction. Although the results were in good qualitative agreement with model, a rigorous quantitative analysis is required to find the additional damping mechanism(s), if any, present. This can be done by measuring the damping lengths of PDs at different frequencies and finding the power law slope. If the slope is significantly different from 2, the value expected for thermal conduction alone, it is indicative of additional damping mechanism(s) present. This idea can be pursued in a future work.

Bibliography

Akiyama, S., Doschek, G. A. and Mariska, J. T., 2005, "Nonthermal Velocities in Different Temperature Regions of the Solar Lower Transition Region", *Astrophys. J.*, **623**, 540–550. [DOI], [ADS]

Antiochos, S. K., MacNeice, P. J., Spicer, D. S. and Klimchuk, J. A., 1999, "The Dynamic Formation of Prominence Condensations", *Astrophys. J.*, **512**, 985–991. [DOI], [ADS], [arXiv:astro-ph/9808199]

Arnaud, M. and Raymond, J., 1992, "Iron ionization and recombination rates and ionization equilibrium", *Astrophys. J.*, **398**, 394–406. [DOI], [ADS]

Aschwanden, M. J., 2005, *Physics of the Solar Corona. An Introduction with Problems and Solutions (2nd edition)*. [ADS]

Aschwanden, M. J., Nightingale, R. W. and Alexander, D., 2000, "Evidence for Nonuniform Heating of Coronal Loops Inferred from Multithread Modeling of TRACE Data", *Astrophys. J.*, **541**, 1059–1077. [DOI], [ADS]

Aschwanden, M. J., Schrijver, C. J. and Alexander, D., 2001, "Modeling of Coronal EUV Loops Observed with TRACE. I. Hydrostatic Solutions with Nonuniform Heating", *Astrophys. J.*, **550**, 1036–1050. [DOI], [ADS]

Banerjee, D., Teriaca, L., Doyle, J. G. and Wilhelm, K., 1998, "Broadening of SI VIII lines observed in the solar polar coronal holes", *Astron. Astrophys.*, **339**, 208–214. [ADS]

Banerjee, D., O'Shea, E. and Doyle, J. G., 2000a, "Long-Period Oscillations in Polar Plumes as Observed by cds on Soho", *Solar Phys.*, **196**, 63–78. [ADS]

Banerjee, D., Teriaca, L., Doyle, J. G. and Lemaire, P., 2000b, "Polar Plumes and Inter-plume regions as observed by SUMER on SOHO", *Solar Phys.*, **194**, 43–58. [ADS]

Banerjee, D., O'Shea, E., Doyle, J. G. and Goossens, M., 2001a, "Long period oscillations in the inter-plume regions of the Sun", *Astron. Astrophys.*, **377**, 691–700. [DOI], [ADS]

Banerjee, D., O'Shea, E., Doyle, J. G. and Goossens, M., 2001b, "Signatures of very long period waves in the polar coronal holes", *Astron. Astrophys.*, **380**, L39–L42. [DOI], [ADS]

Banerjee, D., Erdélyi, R., Oliver, R. and O'Shea, E., 2007, "Present and Future Observing Trends in Atmospheric Magnetoseismology", *Solar Phys.*, **246**, 3–29. [DOI], [ADS]

Banerjee, D., Pérez-Suárez, D. and Doyle, J. G., 2009a, "Signatures of Alfvén waves in the polar coronal holes as seen by EIS/Hinode", *Astron. Astrophys.*, **501**, L15–L18. [DOI], [ADS], [arXiv:0906.4600 [astro-ph.SR]]

Banerjee, D., Teriaca, L., Gupta, G. R., Imada, S., Stenborg, G. and Solanki, S. K., 2009b, "Propagating waves in polar coronal holes as seen by SUMER & EIS", *Astron. Astrophys.*, **499**, L29–L32. [DOI], [ADS], [arXiv:0905.1013 [astro-ph.SR]]

Bemporad, A. and Abbo, L., 2012, "Spectroscopic Signature of Alfvén Waves Damping in a Polar Coronal Hole up to 0.4 Solar Radii", *Astrophys. J.*, **751**, 110. [DOI], [ADS], [arXiv:1204.2544 [astro-ph.SR]]

Berghmans, D. and Clette, F., 1999, "Active region EUV transient brightenings - First Results by EIT of SOHO JOP80", *Solar Phys.*, **186**, 207–229. [ADS]

Berghmans, D. and Clette, F., 1999, "Active region EUV transient brightenings – First Results by EIT of SOHO JOP80", *Solar Phys.*, **186**, 207–229. [DOI], [ADS]

Bevington, P. R., 1969, *Data reduction and error analysis for the physical sciences*. [ADS]

Boerner, P., Edwards, C., Lemen, J., Rausch, A., Schrijver, C., Shine, R., Shing, L., Stern, R., Tarbell, T., Title, A., Wolfson, C. J., Soufli, R., Spiller, E., Gullikson, E., McKenzie, D., Windt, D., Golub, L., Podgorski, W., Testa, P.

and Weber, M., 2012, "Initial Calibration of the Atmospheric Imaging Assembly (AIA) on the Solar Dynamics Observatory (SDO)", *Solar Phys.*, **275**, 41–66. [DOI], [ADS]

Brown, C. M., Feldman, U., Seely, J. F., Korendyke, C. M. and Hara, H., 2008, "Wavelengths and Intensities of Spectral Lines in the 171-211 and 245-291 Å Ranges from Five Solar Regions Recorded by the Extreme-Ultraviolet Imaging Spectrometer (EIS) on Hinode", *Astrophys. J. Suppl.*, **176**, 511–535. [DOI], [ADS]

Casalbuoni, S., Del Zanna, L., Habbal, S. R. and Velli, M., 1999, "Coronal plumes and the expansion of pressure-balanced structures in the fast solar wind", *J. Geophys. Res.*, **104**, 9947–9962. [DOI], [ADS]

Contesse, L., Koutchmy, S. and Viladrich, C., 2004, "Analysis of non-thermal velocities in the solar corona", *Annales Geophysicae*, **22**, 3055–3062. [DOI], [ADS]

Culhane, J. L., Harra, L. K., James, A. M., Al-Janabi, K., Bradley, L. J., Chaudry, R. A., Rees, K., Tandy, J. A., Thomas, P., Whillock, M. C. R., Winter, B., Doschek, G. A., Korendyke, C. M., Brown, C. M., Myers, S., Mariska, J., Seely, J., Lang, J., Kent, B. J., Shaughnessy, B. M., Young, P. R., Simnett, G. M., Castelli, C. M., Mahmoud, S., Mapson-Menard, H., Probyn, B. J., Thomas, R. J., Davila, J., Dere, K., Windt, D., Shea, J., Hagood, R., Moye, R., Hara, H., Watanabe, T., Matsuzaki, K., Kosugi, T., Hansteen, V. and Wikstol, Ø., 2007, "The EUV Imaging Spectrometer for Hinode", *Solar Phys.*, **243**, 19–61. [DOI], [ADS]

De Moortel, I., 2009, "Longitudinal Waves in Coronal Loops", *Space Sci. Rev.*, **149**, 65–81. [DOI], [ADS]

De Moortel, I. and Hood, A. W., 2003, "The damping of slow MHD waves in solar coronal magnetic fields", *Astron. Astrophys.*, **408**, 755–765. [DOI], [ADS]

De Moortel, I. and Hood, A. W., 2004, "The damping of slow MHD waves in solar coronal magnetic fields. II. The effect of gravitational stratification and field line divergence", *Astron. Astrophys.*, **415**, 705–715. [DOI], [ADS]

De Moortel, I., Ireland, J. and Walsh, R. W., 2000, "Observation of oscillations in coronal loops", *Astron. Astrophys.*, **355**, L23–L26. [ADS]

De Moortel, I., Ireland, J., Hood, A. W. and Walsh, R. W., 2002a, "The detection of 3 & 5 min period oscillations in coronal loops", *Astron. Astrophys.*, **387**, L13–L16. [DOI], [ADS]

De Moortel, I., Ireland, J., Walsh, R. W. and Hood, A. W., 2002b, "Longitudinal intensity oscillations in coronal loops observed with TRACE I. Overview of Measured Parameters", *Solar Phys.*, **209**, 61–88. [DOI], [ADS]

De Pontieu, B. and McIntosh, S. W., 2010, "Quasi-periodic Propagating Signals in the Solar Corona: The Signature of Magnetoacoustic Waves or High-velocity Upflows?", *Astrophys. J.*, **722**, 1013–1029. [DOI], [ADS], [arXiv:1008.5300 [astro-ph.SR]]

De Pontieu, B., Erdélyi, R. and James, S. P., 2004, "Solar chromospheric spicules from the leakage of photospheric oscillations and flows", *Nature*, **430**, 536–539. [DOI], [ADS]

De Pontieu, B., Erdélyi, R. and De Moortel, I., 2005, "How to Channel Photospheric Oscillations into the Corona", *Astrophys. J. Lett.*, **624**, L61–L64. [DOI], [ADS]

Deforest, C. E. and Gurman, J. B., 1998, "Observation of Quasi-periodic Compressive Waves in Solar Polar Plumes", *Astrophys. J. Lett.*, **501**, L217. [DOI], [ADS]

Deforest, C. E., Hoeksema, J. T., Gurman, J. B., Thompson, B. J., Plunkett, S. P., Howard, R., Harrison, R. C. and Hassler, D. M., 1997, "Polar Plume Anatomy: Results of a Coordinated Observation", *Solar Phys.*, **175**, 393–410. [DOI], [ADS]

Del Zanna, G. and Mason, H. E., 2003, "Solar active regions: SOHO/CDS and TRACE observations of quiescent coronal loops", *Astron. Astrophys.*, **406**, 1089–1103. [DOI], [ADS]

Doyle, J. G., Banerjee, D. and Perez, M. E., 1998, "Coronal line-width variations", *Solar Phys.*, **181**, 91–101. [ADS]

Edlén, B., 1943, "Die Deutung der Emissionslinien im Spektrum der Sonnenkorona. Mit 6 Abbildungen.", *Z. Astrophys.*, **22**, 30. [ADS]

Erdélyi, R. and Ballai, I., 2007, "Heating of the solar and stellar coronae: a review", *Astronomische Nachrichten*, **328**, 726–733. [DOI], [ADS]

Erdelyi, R., Doyle, J. G., Perez, M. E. and Wilhelm, K., 1998, "Center-to-limb line width measurements of solar chromospheric, transition region and coronal lines", *Astron. Astrophys.*, **337**, 287–293. [ADS]

Gabriel, A. H., Bely-Dubau, F. and Lemaire, P., 2003, "The Contribution of Polar Plumes to the Fast Solar Wind", *Astrophys. J.*, **589**, 623–634. [DOI], [ADS]

Gabriel, A. H., Abbo, L., Bely-Dubau, F., Llebaria, A. and Antonucci, E., 2005, "Solar Wind Outflow in Polar Plumes from 1.05 to 2.4 R_solar", *Astrophys. J. Lett.*, **635**, L185–L188. [DOI], [ADS]

Guhathakurta, M., Fisher, R. R. and Altrock, R. C., 1993, "Large-scale coronal temperature and density distributions, 1984-1992", *Astrophys. J. Lett.*, **414**, L145–L148. [DOI], [ADS]

Gupta, G. R., Banerjee, D., Teriaca, L., Imada, S. and Solanki, S., 2010, "Accelerating Waves in Polar Coronal Holes as Seen by EIS and SUMER", *Astrophys. J.*, **718**, 11–22. [DOI], [ADS], [arXiv:1005.3453 [astro-ph.SR]]

Hahn, M., Landi, E. and Savin, D. W., 2012, "Evidence of Wave Damping at Low Heights in a Polar Coronal Hole", *Astrophys. J.*, **753**, 36. [DOI], [ADS], [arXiv:1202.1743 [astro-ph.SR]]

Harra, L. K., Sakao, T., Mandrini, C. H., Hara, H., Imada, S., Young, P. R., van Driel-Gesztelyi, L. and Baker, D., 2008, "Outflows at the Edges of Active Regions: Contribution to Solar Wind Formation?", *Astrophys. J. Lett.*, **676**, L147–L150. [DOI], [ADS]

Harrison, R. A., Hood, A. W. and Pike, C. D., 2002, "Off-limb EUV line profiles and the search for wave activity in the low corona", *Astron. Astrophys.*, **392**, 319–327. [DOI], [ADS]

Hassler, D. M. and Moran, T. G., 1994, "Broadening of the FeX (6374 {\AA}) profiles above the limb in a coronal hole", *Space Science Reviews*, **70**, 373–377. [DOI], [ADS]

Hassler, D. M., Rottman, G. J., Shoub, E. C. and Holzer, T. E., 1990, "Line broadening of MG X 609 and 625 A coronal emission lines observed above the solar limb", *Astrophys. J. Lett.*, **348**, L77–L80. [DOI], [ADS]

Huang, Z., Frazin, R. A., Landi, E., Manchester, W. B., Vásquez, A. M. and Gombosi, T. I., 2012, "Newly Discovered Global Temperature Structures in the Quiet Sun at Solar Minimum", *Astrophys. J.*, **755**, 86. [DOI], [ADS], [arXiv:1207.6661 [astro-ph.SR]]

Ireland, J., Walsh, R. W., Harrison, R. A. and Priest, E. R., 1999, "A wavelet analysis of active region oscillations", *Astron. Astrophys.*, **347**, 355–365. [ADS]

Jess, D. B., Mathioudakis, M., Erdélyi, R., Crockett, P. J., Keenan, F. P. and Christian, D. J., 2009, "Alfvén Waves in the Lower Solar Atmosphere", *Science*, **323**, 1582–. [DOI], [ADS], [arXiv:0903.3546 [astro-ph.SR]]

Kamio, S., Hara, H., Watanabe, T., Fredvik, T. and Hansteen, V. H., 2010, "Modeling of EIS Spectrum Drift from Instrumental Temperatures", *Solar Phys.*, **266**, 209–223. [DOI], [ADS], [arXiv:1003.3540 [astro-ph.SR]]

Kano, R. and Tsuneta, S., 1996, "Temperature Distributions and Energy Scaling Law of Solar Coronal Loops Obtained with YOHKOH", *Pub. Astron. Soc. Japan*, **48**, 535–543. [ADS]

Kiddie, G., De Moortel, I., Del Zanna, G., McIntosh, S. W. and Whittaker, I., 2012, "Propagating Disturbances in Coronal Loops: A Detailed Analysis of Propagation Speeds", *Solar Phys.*, **279**, 427–452. [DOI], [ADS], [arXiv:1205.0891 [astro-ph.SR]]

King, D. B., Nakariakov, V. M., Deluca, E. E., Golub, L. and McClements, K. G., 2003, "Propagating EUV disturbances in the Solar corona: Two-wavelength observations", *Astron. Astrophys.*, **404**, L1–L4. [DOI], [ADS]

Klimchuk, J. A., 2006, "On Solving the Coronal Heating Problem", *Solar Phys.*, **234**, 41–77. [DOI], [ADS], [arXiv:astro-ph/0511841]

Kosugi, T., Matsuzaki, K., Sakao, T., Shimizu, T., Sone, Y., Tachikawa, S., Hashimoto, T., Minesugi, K., Ohnishi, A., Yamada, T., Tsuneta, S., Hara, H., Ichimoto, K., Suematsu, Y., Shimojo, M., Watanabe, T., Shimada, S.,

Davis, J. M., Hill, L. D., Owens, J. K., Title, A. M., Culhane, J. L., Harra, L. K., Doschek, G. A. and Golub, L., 2007, "The Hinode (Solar-B) Mission: An Overview", *Solar Phys.*, **243**, 3–17. [DOI], [ADS]

K.P. Dere, E. Landi, H.E. Mason, B.C. Monsignori Fossi and P.R. Young, 1997, "CHIANTI - an atomic database for emission lines", *Astron. Astrophys. Suppl. Ser.*, **125**(1), 149–173. [DOI]URL: http://dx.doi.org/10.1051/aas:1997368

Krishna Prasad, S., Banerjee, D. and Gupta, G. R., 2011, "Propagating intensity disturbances in polar corona as seen from AIA/SDO", *Astron. Astrophys.*, **528**, L4. [DOI], [ADS], [arXiv:1102.2979 [astro-ph.SR]]

Krishna Prasad, S., Banerjee, D. and Singh, J., 2012a, "Oscillations in Active Region Fan Loops: Observations from EIS/ Hinode and AIA/SDO", *Solar Phys.*, **281**, 67–85. [DOI], [ADS], [arXiv:1208.1377 [astro-ph.SR]]

Krishna Prasad, S., Banerjee, D., Van Doorsselaere, T. and Singh, J., 2012b, "Omnipresent long-period intensity oscillations in open coronal structures", *Astron. Astrophys.*, **546**, A50. [DOI], [ADS], [arXiv:1209.2536 [astro-ph.SR]]

Krishna Prasad, S., Singh, J. and Ichimoto, K., 2013, "Thermal Structure of Coronal Loops as Seen with Norikura Coronagraph", *Astrophys. J. Lett.*, **765**, L46. [DOI], [ADS], [arXiv:1302.5905 [astro-ph.SR]]

Landi, E. and Feldman, U., 2004, "Models for Solar Magnetic Loops. IV. On the Relation between Coronal and Footpoint Plasma in Active Region Loops", *Astrophys. J.*, **611**, 537–544. [DOI], [ADS]

Landi, E., Del Zanna, G., Young, P. R., Dere, K. P. and Mason, H. E., 2012, "CHIANTI—An Atomic Database for Emission Lines. XII. Version 7 of the Database", *Astrophys. J.*, **744**, 99. [DOI], [ADS]

Lemen, J. R., Title, A. M., Akin, D. J., Boerner, P. F., Chou, C., Drake, J. F., Duncan, D. W., Edwards, C. G., Friedlaender, F. M., Heyman, G. F., Hurlburt, N. E., Katz, N. L., Kushner, G. D., Levay, M., Lindgren, R. W., Mathur, D. P., McFeaters, E. L., Mitchell, S., Rehse, R. A., Schrijver, C. J., Springer, L. A., Stern, R. A., Tarbell, T. D., Wuelser, J.-P., Wolfson, C. J., Yanari, C., Bookbinder, J. A., Cheimets, P. N., Caldwell, D., Deluca, E. E., Gates, R.,

Golub, L., Park, S., Podgorski, W. A., Bush, R. I., Scherrer, P. H., Gummin, M. A., Smith, P., Auker, G., Jerram, P., Pool, P., Soufli, R., Windt, D. L., Beardsley, S., Clapp, M., Lang, J. and Waltham, N., 2012, "The Atmospheric Imaging Assembly (AIA) on the Solar Dynamics Observatory (SDO)", *Solar Phys.*, **275**, 17–40. [DOI], [ADS]

Lenz, D. D., Deluca, E. E., Golub, L., Rosner, R. and Bookbinder, J. A., 1999, "Temperature and Emission-Measure Profiles along Long-lived Solar Coronal Loops Observed with the Transition Region and Coronal Explorer", *Astrophys. J. Lett.*, **517**, L155–L158. [DOI], [ADS], [arXiv:astro-ph/9903491]

Mariska, J. T., 1992, *The solar transition region*. [ADS]

Mariska, J. T. and Muglach, K., 2010, "Doppler-shift, Intensity, and Density Oscillations Observed with the Extreme Ultraviolet Imaging Spectrometer on Hinode", *Astrophys. J.*, **713**, 573–583. [DOI], [ADS], [arXiv:1003.0420 [astro-ph.SR]]

Mariska, J. T., Warren, H. P., Williams, D. R. and Watanabe, T., 2008, "Observations of Doppler Shift Oscillations with the EUV Imaging Spectrometer on Hinode", *Astrophys. J. Lett.*, **681**, L41–L44. [DOI], [ADS], [arXiv:0806.0265]

Marsh, M. S., Walsh, R. W., De Moortel, I. and Ireland, J., 2003, "Joint observations of propagating oscillations with SOHO/CDS and TRACE", *Astron. Astrophys.*, **404**, L37–L41. [DOI], [ADS]

Marsh, M. S., Walsh, R. W. and Plunkett, S., 2009, "Three-dimensional Coronal Slow Modes: Toward Three-dimensional Seismology", *Astrophys. J.*, **697**, 1674–1680. [DOI], [ADS], [arXiv:0903.4039]

Mathioudakis, M., Jess, D. B. and Erdélyi, R., 2013, "Alfvén Waves in the Solar Atmosphere. From Theory to Observations", *Space Sci. Rev.*, **175**, 1–27. [DOI], [ADS], [arXiv:1210.3625 [astro-ph.SR]]

McComas, D. J., Ebert, R. W., Elliott, H. A., Goldstein, B. E., Gosling, J. T., Schwadron, N. A. and Skoug, R. M., 2008, "Weaker solar wind from the polar coronal holes and the whole Sun", *Geophys. Res. Lett.*, **35**, L18103. [DOI], [ADS]

McEwan, M. P. and De Moortel, I., 2006, "Longitudinal intensity oscillations observed with TRACE: evidence of fine-scale structure", *Astron. Astrophys.*, **448**, 763–770. [DOI], [ADS]

McIntosh, S. W. and De Pontieu, B., 2009, "Observing Episodic Coronal Heating Events Rooted in Chromospheric Activity", *Astrophys. J. Lett.*, **706**, L80–L85. [DOI], [ADS], [arXiv:0910.2452 [astro-ph.SR]]

McIntosh, S. W., Innes, D. E., de Pontieu, B. and Leamon, R. J., 2010, "STEREO observations of quasi-periodically driven high velocity outflows in polar plumes", *Astron. Astrophys.*, **510**, L2. [DOI], [ADS], [arXiv:1001.3377 [astro-ph.SR]]

Mendoza-Briceño, C. A., Erdélyi, R. and Di G. Sigalotti, L., 2002, "Coronal Loop Heating by Random Energy Releases", *Astrophys. J. Lett.*, **579**, L49–L52. [DOI], [ADS]

Mierla, M., Schwenn, R., Teriaca, L., Stenborg, G. and Podlipnik, B., 2008, "Analysis of the Fe X and Fe XIV line width in the solar corona using LASCO-C1 spectral data", *Astron. Astrophys.*, **480**, 509–514. [DOI], [ADS], [arXiv:0903.0496 [astro-ph.SR]]

Morton, R. J., Verth, G., Jess, D. B., Kuridze, D., Ruderman, M. S., Mathioudakis, M. and Erdélyi, R., 2012, "Observations of ubiquitous compressive waves in the Sun's chromosphere", *Nature Communications*, **3**, 1315. [DOI], [ADS], [arXiv:1306.4124 [astro-ph.SR]]

Nightingale, R. W., Aschwanden, M. J. and Hurlburt, N. E., 1999, "Time Variability of EUV Brightenings in Coronal Loops Observed with TRACE", *Solar Phys.*, **190**, 249–265. [DOI], [ADS]

Nishizuka, N. and Hara, H., 2011, "Spectroscopic Observations of Continuous Outflows and Propagating Waves from NOAA 10942 with Extreme Ultraviolet Imaging Spectrometer/Hinode", *Astrophys. J. Lett.*, **737**, L43. [DOI], [ADS]

Noens, J. C., Pageault, J. and Ratier, G., 1984, "Measuring electron density in coronal active regions. II - A multichannel coronagraph with a photoelectric spectrograph and a reflex monitor at lambda 5303 A", *Solar Phys.*, **94**, 117–131. [DOI], [ADS]

Nuevo, F. A., Huang, Z., Frazin, R., Manchester, iv, W. B., Jin, M. and Vásquez, A. M., 2013, "Evolution of the Global Temperature Structure of the Solar Corona during the Minimum between Solar Cycles 23 and 24", *Astrophys. J.*, **773**, 9. [DOI], [ADS]

Ofman, L., Romoli, M., Poletto, G., Noci, G. and Kohl, J. L., 1997, "Ultraviolet Coronagraph Spectrometer Observations of Density Fluctuations in the Solar Wind", *Astrophys. J. Lett.*, **491**, L111. [DOI], [ADS]

Ofman, L., Nakariakov, V. M. and Deforest, C. E., 1999, "Slow Magnetosonic Waves in Coronal Plumes", *Astrophys. J.*, **514**, 441–447. [DOI], [ADS]

Ofman, L., Nakariakov, V. M. and Sehgal, N., 2000, "Dissipation of Slow Magnetosonic Waves in Coronal Plumes", *Astrophys. J.*, **533**, 1071–1083. [DOI], [ADS]

O'Shea, E. and Doyle, J. G., 2009, "On oscillations found in an active region with EIS on Hinode", *Astron. Astrophys.*, **494**, 355–360. [DOI], [ADS]

O'Shea, E., Banerjee, D., Doyle, J. G., Fleck, B. and Murtagh, F., 2001, "Active region oscillations", *Astron. Astrophys.*, **368**, 1095–1107. [DOI], [ADS]

O'Shea, E., Muglach, K. and Fleck, B., 2002, "Oscillations above sunspots: Evidence for propagating waves?", *Astron. Astrophys.*, **387**, 642–664. [DOI], [ADS]

O'Shea, E., Banerjee, D. and Poedts, S., 2003, "Variation of coronal line widths on and off the disk", *Astron. Astrophys.*, **400**, 1065–1070. [DOI], [ADS]

O'Shea, E., Banerjee, D. and Doyle, J. G., 2005, "On the widths and ratios of Mg X 609.79 and 624.94 Å lines in polar off-limb regions", *Astron. Astrophys.*, **436**, L35–L38. [DOI], [ADS]

O'Shea, E., Banerjee, D. and Doyle, J. G., 2006, "Magnetoacoustic wave propagation in off-limb polar regions", *Astron. Astrophys.*, **452**, 1059–1068. [DOI], [ADS]

O'Shea, E., Banerjee, D. and Doyle, J. G., 2007, "A statistical study of wave propagation in coronal holes", *Astron. Astrophys.*, **463**, 713–725. [DOI], [ADS]

Owen, N. R., De Moortel, I. and Hood, A. W., 2009, "Forward modelling to determine the observational signatures of propagating slow waves for TRACE, SoHO/CDS, and Hinode/EIS", *Astron. Astrophys.*, **494**, 339–353. [DOI], [ADS]

Parker, E. N., 1958, "Dynamics of the Interplanetary Gas and Magnetic Fields.", *Astrophys. J.*, **128**, 664. [DOI], [ADS]

Patsourakos, S. and Klimchuk, J. A., 2007, "The Cross-Field Thermal Structure of Coronal Loops from Triple-Filter TRACE Observations", *Astrophys. J.*, **667**, 591–601. [DOI], [ADS]

Pekünlü, E. R., Bozkurt, Z., Afsar, M., Soydugan, E. and Soydugan, F., 2002, "Alfvén waves in the inner polar coronal hole", *Mon. Not. Roy. Astron. Soc.*, **336**, 1195–1200. [DOI], [ADS]

Pesnell, W. D., Thompson, B. J. and Chamberlin, P. C., 2012, "The Solar Dynamics Observatory (SDO)", *Solar Phys.*, **275**, 3–15. [DOI], [ADS]

Prasad, S. K., Singh, J. and Banerjee, D., 2013, "Variation of Emission Line Width in Mid- and High-Latitude Corona", *Solar Phys.*, **282**, 427–442. [DOI], [ADS], [arXiv:1210.6434 [astro-ph.SR]]

Priest, E. R., 1984, *Solar magneto-hydrodynamics*, Geophysics and Astrophysics Monographs, Dordrecht: Reidel, 1984. [ADS]

Priest, E. R., Foley, C. R., Heyvaerts, J., Arber, T. D., Culhane, J. L. and Acton, L. W., 1998, "Nature of the heating mechanism for the diffuse solar corona", *Nature*, **393**, 545–547. [DOI], [ADS]

Raju, K. P., Chandrasekhar, T. and Ashok, N. M., 2011, "Analysis of Coronal Green Line Profiles: Evidence of Excess Blueshifts", *Astrophys. J.*, **736**, 164. [DOI], [ADS], [arXiv:1106.3206 [astro-ph.SR]]

Reale, F. and Ciaravella, A., 2006, "Analysis of a multi-wavelength time-resolved observation of a coronal loop", *Astron. Astrophys.*, **449**, 1177–1192. [DOI], [ADS], [arXiv:astro-ph/0512397]

Reale, F. and Peres, G., 2000, "TRACE-derived Temperature and Emission Measure Profiles along Long-lived Coronal Loops: The Role of Filamentation", *Astrophys. J. Lett.*, **528**, L45–L48. [DOI], [ADS], [arXiv:astro-ph/9911096]

Robbrecht, E., Verwichte, E., Berghmans, D., Hochedez, J. F., Poedts, S. and Nakariakov, V. M., 2001, "Slow magnetoacoustic waves in coronal loops: EIT and TRACE", *Astron. Astrophys.*, **370**, 591–601. [DOI], [ADS]

Roberts, B., Edwin, P. M. and Benz, A. O., 1984, "On coronal oscillations", *Astrophys. J.*, **279**, 857–865. [DOI]

Rosner, R., Tucker, W. H. and Vaiana, G. S., 1978, "Dynamics of the quiescent solar corona", *Astrophys. J.*, **220**, 643–645. [DOI], [ADS]

Sakao, T., Kano, R., Narukage, N., Kotoku, J., Bando, T., DeLuca, E. E., Lundquist, L. L., Tsuneta, S., Harra, L. K., Katsukawa, Y., Kubo, M., Hara, H., Matsuzaki, K., Shimojo, M., Bookbinder, J. A., Golub, L., Korreck, K. E., Su, Y., Shibasaki, K., Shimizu, T. and Nakatani, I., 2007, "Continuous Plasma Outflows from the Edge of a Solar Active Region as a Possible Source of Solar Wind", *Science*, **318**, 1585–1588. [DOI], [ADS]

Schmelz, J. T., 2002, "Are Coronal Loops Isothermal?", *Astrophys. J. Lett.*, **578**, L161–L164. [DOI], [ADS]

Schmelz, J. T., Reames, D. V., von Steiger, R. and Basu, S., 2012, "Composition of the Solar Corona, Solar Wind, and Solar Energetic Particles", *Astrophys. J.*, **755**, 33. [DOI], [ADS]

Schrijver, C. J., Title, A. M., Berger, T. E., Fletcher, L., Hurlburt, N. E., Nightingale, R. W., Shine, R. A., Tarbell, T. D., Wolfson, J., Golub, L., Bookbinder, J. A., Deluca, E. E., McMullen, R. A., Warren, H. P., Kankelborg, C. C., Handy, B. N. and de Pontieu, B., 1999, "A new view of the solar outer atmosphere by the Transition Region and Coronal Explorer", *Solar Phys.*, **187**, 261–302

Seely, J. F., Feldman, U., Schuehle, U., Wilhelm, K., Curdt, W. and Lemaire, P., 1997, "Turbulent Velocities and Ion Temperatures in the Solar Corona Obtained from SUMER Line Widths", *Astrophys. J. Lett.*, **484**, L87+. [DOI], [ADS]

Serio, S., Peres, G., Vaiana, G. S., Golub, L. and Rosner, R., 1981, "Closed coronal structures. II - Generalized hydrostatic model", *Astrophys. J.*, **243**, 288–300. [DOI], [ADS]

Singh, J., Ichimoto, K., Imai, H., Sakurai, T. and Takeda, A., 1999, "Spectroscopic Studies of the Solar Corona I. Spatial Variations in Line Parameters of Green and Red Coronal Lines", *Pub. Astron. Soc. Japan*, **51**, 269–276. [ADS]

Singh, J., Sakurai, T., Ichimoto, K., Suematsu, Y. and Takeda, A., 2002a, "Spectroscopic Studies of the Solar Corona II. Properties of Green and Red Emission Lines in Open and Closed Coronal Structures", *Pub. Astron. Soc. Japan*, **54**, 793–806. [ADS]

Singh, J., Sakurai, T., Ichimoto, K. and Takeda, A., 2002b, "Spectroscopic Studies of the Solar Corona III. Density Diagnostics Using the Infrared Lines of Fe XIII", *Pub. Astron. Soc. Japan*, **54**, 807–816. [ADS]

Singh, J., Ichimoto, K., Sakurai, T. and Muneer, S., 2003a, "Spectroscopic Studies of the Solar Corona. IV. Physical Properties of Coronal Structure", *Astrophys. J.*, **585**, 516–523. [DOI], [ADS]

Singh, J., Sakurai, T., Ichimoto, K. and Muneer, S., 2003b, "Spectroscopic Studies of the Solar Corona - V. Physical Properties of Coronal Structures", *Solar Phys.*, **212**, 343–359. [ADS]

Singh, J., Sakurai, T., Ichimoto, K. and Watanabe, T., 2004, "Complex Variations in the Line-Intensity Ratio of Coronal Emission Lines with Height above the Limb", *Astrophys. J. Lett.*, **617**, L81–L84. [DOI], [ADS]

Singh, J., Sakurai, T. and Ichimoto, K., 2006a, "Do the Line Widths of Coronal Emission Lines Increase with Height above the Limb?", *Astrophys. J.*, **639**, 475–483. [DOI], [ADS]

Singh, J., Sakurai, T., Ichimoto, K., Muneer, S. and Raveendran, A. V., 2006b, "Spectroscopic Studies of Solar Corona VIII. Temperature and Non-Thermal Variations in Steady Coronal Structures", *Solar Phys.*, **236**, 245–262. [DOI], [ADS]

Singh, J., Hasan, S. S., Gupta, G. R., Nagaraju, K. and Banerjee, D., 2011, "Spectroscopic Observation of Oscillations in the Corona During the Total Solar Eclipse of 22 July 2009", *Solar Phys.*, **270**, 213–233. [DOI], [ADS]

Soler, R., Oliver, R. and Ballester, J. L., 2008, "Nonadiabatic Magnetohydrodynamic Waves in a Cylindrical Prominence Thread with Mass Flow", *Astrophys. J.*, **684**, 725–735. [DOI], [ADS], [arXiv:0803.2600]

Srivastava, A. K., Singh, J., Dwivedi, B. N., Muneer, S., Sakurai, T. and Ichimoto, K., 2007, "Fe XIV green/Fe XIII infrared line ratio diagnostics", *Bulletin of the Astronomical Society of India*, **35**, 457–463. [ADS]

Teriaca, L., Poletto, G., Romoli, M. and Biesecker, D. A., 2003, "The Nascent Solar Wind: Origin and Acceleration", *Astrophys. J.*, **588**, 566–577. [DOI], [ADS]

Tian, H., McIntosh, S. W. and De Pontieu, B., 2011, "The Spectroscopic Signature of Quasi-periodic Upflows in Active Region Timeseries", *Astrophys. J. Lett.*, **727**, L37. [DOI], [ADS], [arXiv:1012.5112 [astro-ph.SR]]

Tian, H., McIntosh, S. W., Wang, T., Ofman, L., De Pontieu, B., Innes, D. E. and Peter, H., 2012, "Persistent Doppler Shift Oscillations Observed with Hinode/EIS in the Solar Corona: Spectroscopic Signatures of Alfvénic Waves and Recurring Upflows", *Astrophys. J.*, **759**, 144. [DOI], [ADS], [arXiv:1209.5286 [astro-ph.SR]]

Tomczyk, S. and McIntosh, S. W., 2009, "Time-Distance Seismology of the Solar Corona with CoMP", *Astrophys. J.*, **697**, 1384–1391. [DOI], [ADS], [arXiv:0903.2002 [astro-ph.SR]]

Torrence, Christopher and Compo, Gilbert P., 1998, "A Practical Guide to Wavelet Analysis", *Bulletin of the American Meteorological Society*, **79**, 61–78

Tripathi, D., Mason, H. E., Dwivedi, B. N., del Zanna, G. and Young, P. R., 2009, "Active Region Loops: Hinode/Extreme-Ultraviolet Imaging Spectrometer Observations", *Astrophys. J.*, **694**, 1256–1265. [DOI], [ADS], [arXiv:0901.0095 [astro-ph.SR]]

Uchida, Y., 1970, "Diagnosis of Coronal Magnetic Structure by Flare-Associated Hydromagnetic Disturbances", *Pub. Astron. Soc. Japan*, **22**, 341–+

Van Doorsselaere, T., Wardle, N., Del Zanna, G., Jansari, K., Verwichte, E. and Nakariakov, V. N., 2011, "The first measurement of the coronal adiabatic index", *Astrophys. J. Lett.*, **727**

Verwichte, E., Marsh, M., Foullon, C., Van Doorsselaere, T., De Moortel, I., Hood, A. W. and Nakariakov, V. M., 2010, "Periodic Spectral Line Asymmetries in Solar Coronal Structures from Slow Magnetoacoustic Waves", *Astrophys. J. Lett.*, **724**, L194–L198. [DOI], [ADS]

Wang, T. J., Ofman, L. and Davila, J. M., 2009a, "Propagating Slow Magnetoacoustic Waves in Coronal Loops Observed by Hinode/EIS", *Astrophys. J.*, **696**, 1448–1460. [DOI], [ADS], [arXiv:0902.4480 [astro-ph.SR]]

Wang, T. J., Ofman, L., Davila, J. M. and Mariska, J. T., 2009b, "Hinode/EIS observations of propagating low-frequency slow magnetoacoustic waves in fan-like coronal loops", *Astron. Astrophys.*, **503**, L25–L28. [DOI], [ADS], [arXiv:0908.0310 [astro-ph.SR]]

Wedemeyer-Böhm, S., Scullion, E., Steiner, O., Rouppe van der Voort, L., de La Cruz Rodriguez, J., Fedun, V. and Erdélyi, R., 2012, "Magnetic tornadoes as energy channels into the solar corona", *Nature*, **486**, 505–508. [DOI], [ADS]

Wilhelm, K., 2006, "Solar coronal-hole plasma densities and temperatures", *Astron. Astrophys.*, **455**, 697–708. [DOI], [ADS]

Wilhelm, K., Curdt, W., Marsch, E., Schühle, U., Lemaire, P., Gabriel, A., Vial, J.-C., Grewing, M., Huber, M. C. E., Jordan, S. D., Poland, A. I., Thomas, R. J., Kühne, M., Timothy, J. G., Hassler, D. M. and Siegmund, O. H. W., 1995, "SUMER - Solar Ultraviolet Measurements of Emitted Radiation", *Solar Phys.*, **162**, 189–231. [DOI], [ADS]

Wilhelm, K., Dammasch, I. E., Marsch, E. and Hassler, D. M., 2000, "On the source regions of the fast solar wind in polar coronal holes", *Astron. Astrophys.*, **353**, 749–756. [ADS]

Wilhelm, K., Dwivedi, B. N. and Teriaca, L., 2004, "On the widths of the Mg X lines near 60 nm in the corona", *Astron. Astrophys.*, **415**, 1133–1139. [DOI], [ADS]

Wilhelm, K., Fludra, A., Teriaca, L., Harrison, R. A., Dwivedi, B. N. and Pike, C. D., 2005, "The widths of vacuum-ultraviolet spectral lines in the equatorial solar corona observed with CDS and SUMER", *Astron. Astrophys.*, **435**, 733–741. [DOI], [ADS]

Winebarger, A. R., Warren, H., van Ballegooijen, A., DeLuca, E. E. and Golub, L., 2002, "Steady Flows Detected in Extreme-Ultraviolet Loops", *Astrophys. J. Lett.*, **567**, L89–L92. [DOI], [ADS]

Withbroe, G. L. and Noyes, R. W., 1977, "Mass and energy flow in the solar chromosphere and corona", *Ann. Rev. Astron. Astrophys.*, **15**, 363–387. [DOI], [ADS]

Yang, S. H., Zhang, J., Jin, C. L., Li, L. P. and Duan, H. Y., 2009, "Response of the solar atmosphere to magnetic field evolution in a coronal hole region", *Astron. Astrophys.*, **501**, 745–753. [DOI], [ADS], [arXiv:0904.2684 [astro-ph.SR]]

Yuan, D. and Nakariakov, V. M., 2012, "Measuring the apparent phase speed of propagating EUV disturbances", *Astron. Astrophys.*, **543**, A9. [DOI], [ADS]